INVESTIGATIONS ON THE ELEMENTARY PLASTICITY MECHANISM(S) IN FINE-GRAIN FACE-CENTERED CUBIC METALS AND ALLOYS: A CASE STUDY WITH A HIGH-Mn STEEL

THESIS SUBMITTED FOR THE DEGREE OF
DOCTOR OF PHILOSOPHY (SCIENCE)
OF
JADAVPUR UNIVERSITY
2022

By

Soma Rani Das

Index No.: 41/18/Phys./25

Department of Physics

Jadavpur University

Kolkata-700 032

INDIA

Dedicated

to

my parents

যাদবপুর বিশ্ববিদ্যালয়
কলকাতা - ৭০০ ০৩২, ভারত

JADAVPUR UNIVERSITY
KOLKATA-700 032, INDIA

FACULTY OF SCIENCE : DEPARTMENT OF PHYSICS

CERTIFICATE FROM THE SUPERVISOR

This is to certify that the thesis entitled "***Investigations on the elementary plasticity mechanism(s) in fine-grain face-centered cubic metals and alloys: A case study with a high-Mn steel***" submitted by Soma Rani Das, who got her name registered on 12th February 2018 for the award of Ph.D. (Science) degree of Jadavpur University, is absolutely based upon her own work under the supervision of Dr. Puspendu Sahu and that neither this thesis nor any part of it has been submitted for any degree/diploma or any other academic award anywhere before.

07/03/2022

Signature of the supervisor

and date with official seal

DR. PUSPENDU SAHU
Associate Professor
Department of Physics
Jadavpur University
Kolkata - 700 032

ACKNOWLEDGEMENTS

I would like to take this opportunity to convey my sincere gratitude towards all those people who have extended their valuable assistance, encouragement and contribution indispensably to this PhD work in one way or the other.

First and foremost, I would like to thank my supervisor Dr. Puspendu Sahu for his kindness, constant enthusiasm and guidance. I am extremely grateful for his continuous streams of ideas, which opened many avenues for study and for his intensive proof reading of this thesis. I have been fortunate enough in unflinching support and encouragement from him. I could not have imagined having better advisor and mentor for my Ph.D. study.

I extend my thanks to my lab mates who have assisted me immensely during this tenure. I would like to specially thank of my Lab mate Mr. Saikat Shyamal for his valuable suggestion and contribution in my work. I want to thank my other Lab mates Mr. Tousif Riaz and Mr. Dhananjay Das for all contribution and support.

In my PhD tenure, I got the opportunity to work in collaboration with Dr. Swapan Kumar Shee (Midnapore College), Prof. Pravash Chandra Chakraborti (Jadavpur University), Prof. Jukka Komi (University of Oulu), Prof. L. Pentti Karjalainen (University of Oulu), Prof. David Porter (University of Oulu) Matias Jaskari (University of Oulu). I want to express my deep gratitude to all of them.

I would like to thank Dr. Stefan Martin (TU Bergakademie Freiberg), Dr. Christian Schimpf (TU Bergakademie Freiberg), Prof. Dr. Horst Biermann (TU Bergakademie Freiberg), Prof. Dr. David Rafaja (TU Bergakademie Freiberg) for their active help in carrying out the ECCI measurements described in the dissertation.

From the core of my heart, I would like to specially thank Dr. Bhupeshwar Mahato (CSIR NML, Jamshedpur) for his contribution.

I extend special acknowledgement to all the office staff for their help in regards to all officials activities related directly or indirectly to my research work during these years.

I don't have any idea how to acknowledge my family. I must say that I would not have been able to come to this stage without their constant encouragement, support, love and prayers. Words cannot express how grateful I am to my parents for all of the sacrifices that they have made on my behalf.

I must thank my dearest brother Mr. Debabrata Das for his continuous support and I acknowledge him for his help in AutoCAD drawing.

I would like to thank my lovely friend Mr. Santanu Gayen for his immense and continuous support.

To conclude this, I would like to acknowledge the "DST INSPIRE Fellowship, Government of India" for providing me the financial support. So, again thanks to all.

Soma Rani Das

Date: 07.03.2022

Soma Rani Das

PREFACE

The present dissertation reports the deformation microstructure and the plasticity mechanism(s) of a fine-grain Fe-26Mn-1Al-0.14C high-Mn steel. The thesis is divided into two parts i.e., Part A and Part B. Part A contains two Chapters and six Chapters are in Part B. Chapter 1 briefly describes strain hardening in metals/alloys, stages of strain hardening, the fundamentals of plastic deformation and short literature review on the grain size strengthening in high-Mn steel. Chapter 2 concerns the description of underlying X-ray and electron diffraction theories used towards assessment of deformation microstructure. Chapter 3 describes material processing & the flow stress behavior. Chapter 4 describes results of electron backscattered diffraction and electron channelling contrast imaging of the deformation microstructure. Chapter 5 defines X-ray line profile analysis of the deformation microstructure. Chapter 6 briefly describes transmission electron microscopy investigations and its implications on the deformation mechanism. Chapter 7 describes a quantitative assessment on the contribution of dislocation substructures to flow-stress. Chapter 8 gives the conclusion of the study.

The material chosen is Fe-26Mn-1Al-0.14C high-Mn steel. The compositions reported throughout this dissertation are in weight %, unless otherwise specified. The material was prepared by induction furnace melting. Suitable thermomechanical treatments were applied to produce an average grain size of ~ 5 µm. The initial microstructure was studied using electron backscatter diffraction (EBSD). Uniaxial tensile tests with a quasi-static strain rate: 10^{-4} were carried out at room temperature (RT). The tensile tests were interrupted at 2%, 5%, and 10% true strain and finally continued up to failure at: 50% strain. Deformed microstructures were investigated using X-ray diffraction (XRD) and a transmission electron microscope (TEM). The EBSD and electron channelling contrast imaging (ECCI) measurements were performed using a high-resolution field emission scanning electron microscope equipped with an EBSD system. An attempt has been made to interpret deformation mechanism(s) and to correlate with the strain hardening behavior of the steel.

CONTENTS

Part A

General Introduction & Methodologies

Chapter 1: General Introduction

Chapter 2: Methodologies adopted for interpretation of deformation microstructures

Part B

Case Study with fine grain Fe-Mn-Al-C Steel

Chapter 3: Material, its processing & the flow stress behavior

Chapter 4: Electron Backscattered Diffraction and Electron Channel Contrast Imaging studies of the deformation microstructure

Chapter 5: X-ray diffraction studies of the deformation microstructure

Chapter 6: TEM investigations of the deformation microstructure and the paradigm of twinning

References

Chapter 7: A quantitative assessment of dislocation substructures' contribution to flow-stress

References

Chapter 8: Summary and Conclusions

List of Publications

Journal Publications:

1 X-ray line profile analysis of the deformation microstructure in a medium-grained Fe-Mn-Al-C austenitic steel

S.R. Das, S. Shyamal, S.K. Shee, J.I. Kömi and P. Sahu*, *Materials Characterization*, 172 **(2021)** 110833.

2. On the mechanism of cross-slip induced dislocation substructure formation in an high-Mn steel.

S.R. Das, S. Shyamal, T. Sahu, J.I. Kömi, P.C. Chakraborti, D.A. Porter, L.P. Karjalainen and P. Sahu*, *Materialia* 15 **(2021)** 101042.

3. A quantitative assessment on the contribution of various dislocation substructures to flow stress in a fine-grain high-Mn steel.

S.R. Das, T. Riaz, S. Shyamal, P.C. Chakraborti and P. Sahu*, *Materials Letters*, 300 **(2021)** 130216.

4. Graded deformation in an Fe-Mn-Al-C steel under bending fatigue

S. Shyamal, **S.R. Das**, M. Jaskari, D.A. Porter, L.P. Karjalainen and P. Sahu*, *Materials Letters*, 285 **(2021)** 129002.

5 Dislocation substructures in tensile deformed Fe-Mn-Al-C steel.

T. Riaz, **S.R. Das**, T. Sahu, P.C. Chakraborti and P. Sahu*, *Materials Letters*, 282 **(2021)**128691.

List of Communicated Paper:

1 A classical viewpoint on the suppression of twinning induced plasticity effect in a Fe-Mn-Al-C steel (communicated)

S.R. Das, S. Shyamal, M. Jaskari, P.C. Chakraborti, L.P. Karjalainen, P. Sahu*.

List of Presentation/Participation in conferences

1 Participation in the course “Microstructure and Texture of Materials” in “**Global Initiative for Academic Networks (Gian)**” February 7-15, 2018, Jadavpur University, India.

2. Presentation of a poster entitled “On the strain hardening behavior of a twinning deficient Fe-26Mn-1Al-0.14C high-Mn steel” in “**International Conference on Current Trends in Materials Science and Engineering (CTMSE 2019)**” July 18-20, 2019, S.N. Bose National Centre for Basic Sciences, India.

3 Oral presentation of a paper entitled “Quantitative assessment on the progression of dislocation substructures in a high-Mn steel and their contribution to flow-stress” in “**International Conference of Multidisciplinary Aspects of Materials in Engineering (IC-MAME 2021)**” October 8-9, 2021, Panjab University, Chandigarh, India.

List of symbols*

α''	Angle between the perfect dislocation line and its Burgers vector
n	Any integer
D	apparent crystallite size
σ_A	Applied tensile stress
γ_{fcc}	Austenite (fcc)
$\bar{C}_{hkl}$	Average contrast factor for (hkl) planes
L_0	Average length of the twinning source
ρ_{loop}	Average prismatic loop density
θ_{hkl}	Bragg angle
$\vec{b}_p$	Burgers vector of partial dislocations (Shockley/Frank)
β'	Character angle between the diffraction vector and dislocation line
E_{str}	Coherency strain energy
$\rho(D)$	Column length (size) distribution function
τ_{crss}	Critical resolved shear stress
$(\tau_c)_{twin}$	Critical twinning stress
ΔK	Deviation from diffraction vector
s	Deviation from exact Bragg angle condition in TEM
ΔL	Deviation from L
$\vec{\mathrm{g}}$	Diffraction vector
K	Diffraction vector for X-ray analysis
E_{dil}	Dilatation energy due to volumetric stress
r	Dislocation core radius
ρ	Dislocation density
α_i	Dislocation interaction strength parameter
R_e	Effective outer cut-off radius of dislocations
γ_{eff}	Effective stacking fault energy
B	Electron beam direction
ε_{hcp}	Epsilon martensite (hcp)

x_{eq}	Equilibrium separation distance of the partial dislocation pairs
w_{tw}	Equilibrium twin width
σ	Flow stress
L	Fourier variable
$f_{\gamma(edge)}$	Fraction of edge dislocation
$f_{\gamma(screw)}$	Fraction of screw dislocation
d	Grain size
γ_{∞}	Ideal stacking fault energy
d_{hkl}	Interplanar spacing for (hkl) planes
γ_{isf}	Intrinsic stacking fault energy
$\vec{R}$	Lattice distortion vector
σ_{YS}^{0}	Lattice friction stress
a	Lattice parameter
β	Line breadth
$\vec{u}$	Line direction of dislocations
$\langle \mathrm{\varepsilon}_{\mathrm{L}}^{2} \rangle$	Mean square microstrain
ε_L	Mean squared strain
$A^d(L, K_i)$	Order dependent Fourier strain coefficient
$A^s(L)$	Order independent Fourier size coefficients
$\vec{b}$	Perfect dislocations’ Burgers vector
ν	Poisson's ratio
w	Prismatic loop diameter
K_s	Scherrer constant
q	Screw or edge character of dislocation
E_{sh}	Shear energy
ˋm_T	Shear for partial dislocation
m_G	Shear for perfect dislocation
G	Shear modulus
τ	Shear stress
β_s	Size broadening integral breadth
γ	Stacking fault energy

P_{sf}	Stacking fault probability
w_{sf}	Stacking fault width
β_D	Strain broadening integral breadth
$\rho(\varepsilon_L)$	Strain distribution function
σ_{forest}	Stress due to forest dislocations
σ_{loop}	Stress due to prismatic dislocation loop
T	Taylor factor
P_{tw}	Twin fault probability
e	Vector normal to the dislocation line
λ	Wavelength of X-rays
σ_{YS}	Yield stress

* Symbols appearing in several equations/figures obtained from literatures are not described here. This list primarily describes the symbols considered in the present work.

Abbreviations

BSE	Backscatter electron
BF	Bright field
CCD	Charge-coupled device
CST	Cross-slip truncation
DF	Dark filed
DRV	Dynamic recovery
DSA	Dynamic strain ageing
EBSD	Electron backscatter diffraction
ECCI	Electron channelling contrast imaging
ECAP	Equal channel angular pressing
ESF	Extrinsic stacking fault
fcc	Face-centered cubic
FESEM	Field emission scanning electron microscope
FWHM	Full width half maximum
HRTEM	High resolution transmission electron microscopy
High-Mn	High-Manganese
ICDD	International centre for diffraction data
ISF	Intrinsic stacking fault
IPF	Inverse pole figure
KAM	Kernel average misorientation
LEDS	Low-energy dislocation structures
MBIP	Microband induced plasticity
RT	Room temperature
SEM	Scanning electron microscope
SAD	Selected area diffraction
SPD	Shockley partial dislocation
SRC	Short-range clustering
SRO	Short-range order
SF	Stacking fault
SFE	Stacking fault energy
SHR	Strain hardening rate
TRIP	Transformation induced plasticity

TEM	Transmission electron microscope
TWIP	Twinning induced plasticity
UTS	Ultimate tensile strength
UFG	Ultrafine grained
WA	Warren-Averbach
WB	Weak beam
WBDF	Weak beam dark field
XRD	X-ray diffraction
YS	Yield strength

Part A

General introduction & methodologies

Chapter 1

General introduction

1.1 Background of the work

The development of metals/alloys with high strength, ductility and toughness is long perceived. Typical examples of those in case of steels include advanced high-strength steels comprising dual-phase steels, transformation-induced plasticity (TRIP) steels and high-manganese austenitic steels for automotive applications. In recent years, another concept of advanced steel has gained a great deal of attention driven by the need for further reducing the vehicle weight, without compromising the strength. Traditionally, the high level of specific strength of advanced steels is achieved mainly by increasing the strength of the steels (Grassel *et al.*, 2000; Fan *et al.*, 2009; Bhadeshia, 2010; Jang *et al.*, 2012). An alternative way of increasing the strength is to make the steels lighter by alloying light elements such as Al (and/or Si) with the Fe-Mn-C-base alloy system. The Fe-Al-Mn-C system have been studied for several applications, namely: (i) cryogenic application, (ii) oxidation resistance at high temperature and (iii) corrosion resistance as a potential substitute for more expensive Fe-Cr-Ni base stainless steels (Lee *et al.*, 1992; Shih *et al.*, 1993; Saxena *et al.*, 1994; Zhu & Zhang, 1998; Herrmann, 2003; Hamada & Karjalainen, 2006; Morris *et al.*, 2006). During the last two decades, much effort has been directed towards the development of ductile lightweight steels with high strength and reduced density for structural applications. The Fe-Al-Mn-C system for automotive applications has been studied in Europe and Japan since the early 2000s.

In the 2000s, Frommeyer and Brux (Frommeyer & Brux, 2006) reported high-strength Fe-Al-Mn-C lightweight alloys with excellent ductility, and they coined the term: TRIPLEX steels, which is a multiphase steel with three major phases. It is composed of austenite as the matrix phase with 5–15 vol.% ferrite and nano-sized κ-carbides less than 10 vol.%, which are finely dispersed throughout the austenite. The composition range of these steels covers Fe-(18–28)Mn-(9–12)Al-(0.7–1.2)C (in wt%). Their typical alloy of Fe-28Mn-12Al-1C alloy exhibited a yield strength (YS) of 730 MPa, an ultimate tensile strength (UTS) of 1000 MPa and total elongation of 55% during a uniaxial tensile test performed at room temperature (RT) at a strain rate of 10^{-4} s^{-1}. The concept of lightweight steel looks quite simple, but the underlying metallurgical issues are complicated since the lightweight steel can have ferritic, austenitic or even a multiphase structure depending on the content of primary alloying elements of C, Mn or Al. Such a situation complicates the deformation mechanism as well.

Deformation behavior of face-centered cubic (fcc) metals/alloys, including the austenitic steels is strongly dependent on the stacking fault energy (SFE) of the concerned material. Depending on the SFE value of the steel, strain-induced martensitic transformation and mechanical twinning are deformation mechanisms competitive with dislocation glide. Strain-induced martensitic transformation is known to be dominant when the SFE of austenite is less than about 20 mJ/m^2, while for SFE values above 20 mJ/m^2, mechanical twinning is likely to control the deformation in high manganese (high-Mn) austenitic steels – leading to the well-known twinning induced plasticity (TWIP) effect (Olson & Cohen, 1976a, 1976b). Frommeyer *et al.* (2000) reported the transition of deformation behavior from TRIP to TWIP in Fe-3Si-3Al-Mn alloys containing 15 to 25% Mn. At 15–20% Mn concentrations, the strain-induced martensitic transformation $\gamma_{fcc} \rightarrow \varepsilon_{hcp} \rightarrow \alpha'$ i.e. the TRIP effect dominates, while further increase of Mn content elevates the SFE further and mechanical twinning become a major deformation mode i.e. the TWIP effect predominates.

When the SFE is higher than 30-40 mJ/m^2, the formation of dislocation cell is profound during deformation of high-Mn steels (Remy & Pineau, 1977). The dislocation cell is known to occur in deformation of fcc materials with high SFE due to active cross-slip, while planar glide of dislocation is observed during deformation of fcc metals/alloys having low SFE (Kuhlmann, 2001). However, many Fe-Al-Mn-C austenitic steels deform by planar dislocation glide rather than wavy glide, despite having a high SFE (Frommeyer & Brux, 2006; Yoo & Park, 2008; Choi *et al.*, 2010; Park *et al.,* 2010). For instance, Fe-28Mn-12Al-1C alloy subjected to ageing for 16h at 550°C revealed shear band formation by planar glide even with a SFE ~ 110 mJ/m^2 (Frommeyer & Brux, 2006). Subsequently, Park *et al.* also observed that solution treated Fe-28Mn-9Al-0.8C with SFE ~ 85 mJ/m^2 deformed in planar dislocation glide (Yoo & Park, 2008). Park *et al.* (2010) and Park (2013) attributed the planar glide of dislocations in high-Mn steels to the glide softening phenomenon associated with short-range ordering (SRO) in the solid solution state.

The complex deformation mechanisms in high-Mn steels are further compounded by grain refinement. One important parameter influencing the mechanical twinning behaviour of a given high-Mn steel is the grain size of austenite (Ueji *et al.*, 2000; Gutierrez *et al.*, 2008; Dini *et al.*, 2010; Gutierrez & Raabe., 2012a; Lee, 2012). The densities of mechanical twins are known to significantly decreases at the same strain by refining the grain size from 49.6 μm to 1.8 μm for Fe-31Mn-3Al-3Si high-Mn steel (Ueji *et al.*, 2000). Ueji *et al.* (2000) explains this through the development of a non-planar dislocation structure (Dini & Ueji, 2012), while Gutierrez-Urrutia *et al.* (2008) believes that grain refinement retards mechanical twinning by increasing the critical twinning stress in Fe-22Mn-0.6C steel. Lee (2012) thereafter proposed that the suppression of mechanical twinning by grain refinement is similar to the formation of ε-martensite during grain refinement, and that mechanical twinning is retarded by local increase in SFE near the grain boundaries where the C atoms are segregated to or by the increased back stress of dislocations. Nevertheless, the exact cause of inactive mechanical twinning and the corresponding strain hardening behavior of fine-grained high-Mn steels is still under discussion (Kang *et al.*, 2016) and the present dissertation aims to provide newer insights into investigating the twinning tendency in a fine-grained high-Mn Fe-Mn-Al-C steel and its associated strain hardening behavior based on the classical theory of twinning and existing theory of strain hardening, which are now discussed in the following.

1.2 Strain hardening in metals/alloys and the associated stages

1.2.1. The Hall-Petch theory

In the 1950s, Hall and Petch demonstrated that the yield stress σ_{YS} (Fig. 1.1) (Hall, 1951; Petch, 1953) (and hence the hardness) scales with the inverse square root of grain size in polycrystalline materials according to the following relation:

$$\sigma_{YS}(MPa) = \sigma_{YS}^{0} + \frac{k_{YS}^{HP}}{\sqrt{d}} \tag{1.1}$$

where the parameter σ_{YS}^{0} includes the lattice friction stress, the solid solution strengthening contribution of the alloying elements, and the strain hardening contribution of the initial dislocation density, k_{YS}^{HP} is a material parameter, and d is the average grain size (Armstrong, 2014).

It has been explained by a dislocation pile-up model for the stress concentration at the tip of a slip band (Armstrong, 2014; Cordero *et al.*, 2016), but recently, the validity of this relationship has been debated (Li, 2016). In the 1980s, Gleiter *et al.* (1989) pioneered research into polycrystalline materials whose grains are of nanometre size. It was thought then that these materials would exhibit superior hardness as well as superior wear resistance and fracture strength compared with their coarse-grained counterparts due to the large volume fraction of grain boundaries they contain as grain boundaries were known to govern the response of metals to deformation (Meyers *et al.*, 2006; Pande & Cooper, 2009). Although hardness measurements of some nanocrystalline samples have been reported to be consistent with the behaviour

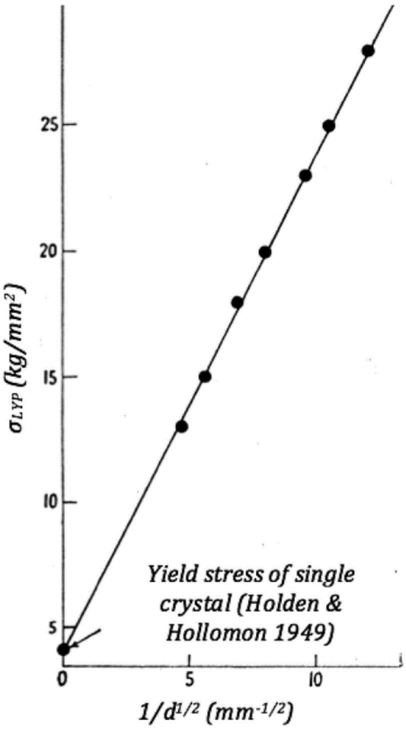

Fig. 1.1: The relationship between lower yield point (σ_{LYP}) and grain size, d, in mild steel (Hall, 1951)

expected by the Hall–Petch equation, grain boundary weakening has also been reported for nanocrystalline materials having typical grain sizes less than 30 nm – the so-called inverse Hall–Petch effect (Chokshi *et al*., 1989; Koch & Narayan, 2000). The inverse Hall–Petch effect has been observed both experimentally (Chokshi *et al*., 1989), as well as in molecular dynamics

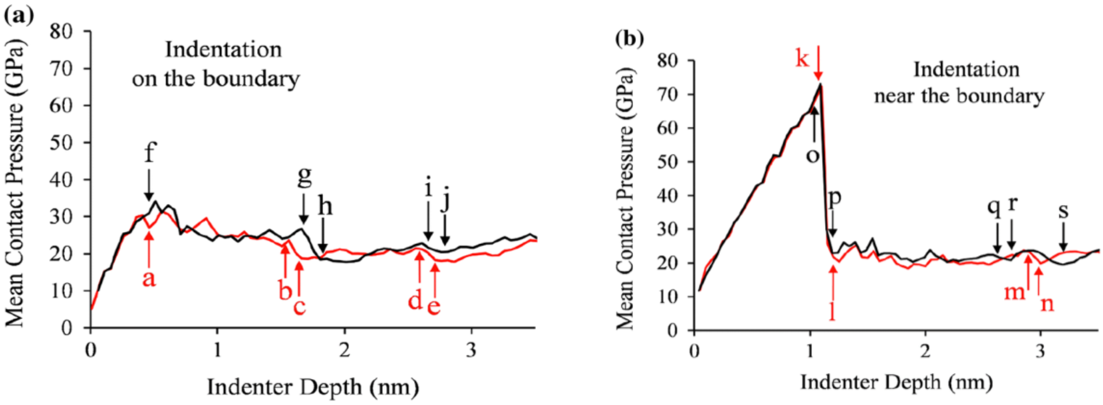

Fig. 1.2: Molecular dynamics simulations of hardness-depth relations for (a) on a grain boundary and (b) near a grain boundary for nanocrystalline pure iron (Kuhr & Aifantis, 2019).

(MD) simulations (Schiotz & Jacobsen, 2003; Huang, 2018; Xu & Davila, 2018; Kuhr & Aifantis, 2019). The weakening has been attributed to (1) processing artefacts (Meyers *et al.*, 2006; Koch & Narayan, 2000), (2) disordered grain boundaries (Armstrong, 2016), and (3) the higher percentage of material in grain boundaries for nano- as opposed to micro-grained materials (Carsley *et al.*, 1995; Carsley *et al.*, 1998) coupled with the intrinsic relative softness of material in grain boundaries (Fig. 1.2) (Kuhr & Aifantis, 2019). Other studies, such as the one reported by Conrad (2004), considered a possible explanation for the effect as being the transition from dislocation controlled to grain boundary and diffusion-dominated deformation (Pande & Cooper, 2009).

1.2.2. The stages of strain hardening

Diehl (1956) in 1956 first demarcated the stress-strain curve into three stages based on the mechanical properties of single crystals, which is presented in Fig. 1.3. Stage I/A is observed only during single slip in single crystals, while Stage II/B is a linear hardening stage with a relatively high work hardening rate and occurs in both single crystals and polycrystals, independently of stage I/A. This hardening behavior is thought of as a limiting behavior at

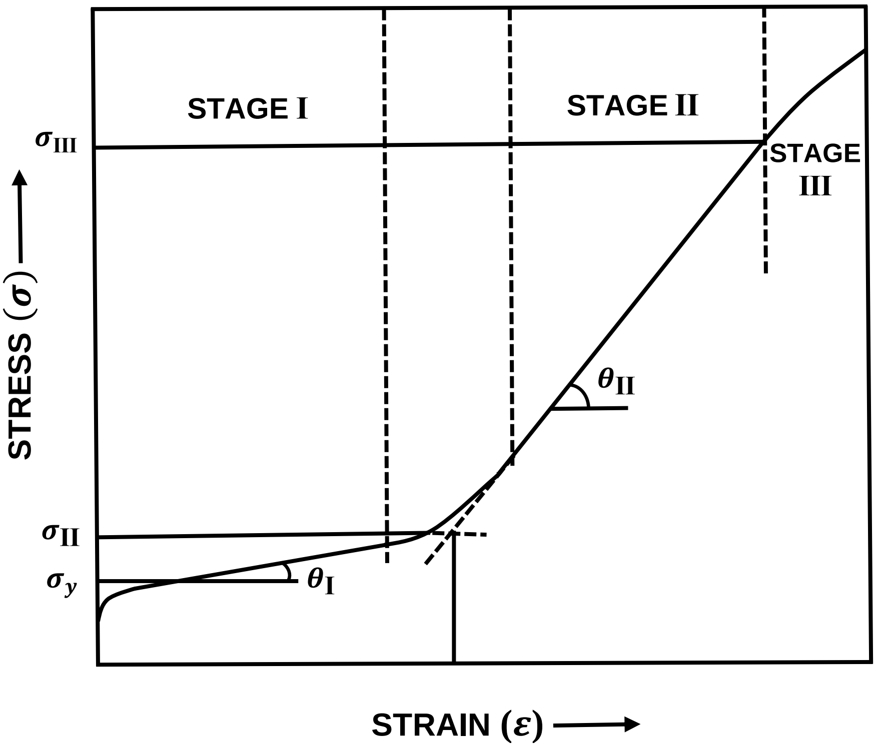

Fig. 1.3: The stages of work hardening, Stage I easy glide, Stage II athermal work hardening and Stage III dynamic recovery (Diehl,1956).

small strains since it’s validity decreases with increasing temperature and SFE. Stage III/C represents a steady decrease in work hardening rate and is sensitive to temperature and strain rate. The theory for stage III/C assumes that a saturation stress is reached at the end of stage III/C when recovery balances dislocation storage. When this discussion turns to consideration of large strain behavior, a further stage IV/D must be added, however. This stage is the low level work hardening that persists in some cases to very large strains. The existence of a stage IV/D in work hardening requires modification of theory of stage III/C that predicts saturation of the flow stress at the end of stage III/C. Some authors refer to a stage V/E, wherein further dynamic recovery takes place, leading to an eventual actual saturation of the flow stress. The various stages of work hardening are most clearly distinguished on a diagram of θversus ε, where $\theta = \frac{d\sigma}{d\varepsilon}$, Fig. 1.4. Stage II is commonly found in low SFE materials and at low temperature at a constant, high, value of G at about $G/200$ ($\frac{d\sigma}{d\varepsilon}$), where G is the shear modulus. Stage III/C is often be represented by a straight line where the hardening rate decreases linearly with stress towards a "saturation stress". Stage IV/D is manifested before the saturation stress is reached and is commonly thought of as another stage of constant, low θ at about 2.10^{-4}G.

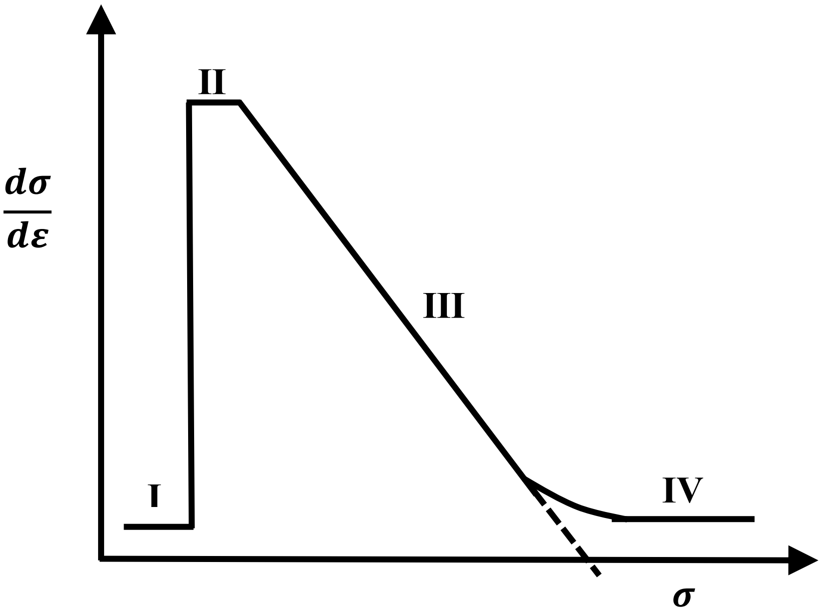

Fig. 1.4: Stages of work hardening for a single crystal represented on a plot of hardening rate versus flow stress. A polycrystal would show stages III & IV, possibly II also (Rolltt & Kocks, 1993)

1.3. The factors influencing the strain hardening of high-Mn steels

1.3.1. The SFE of austenite

The SFE is a key factor that controls the mechanical properties of the high-Mn alloys, including the occurrence of TWIP effect. It is still unclear why a threshold SFE value is essential for occurrence of the strain induced twinning, but it appears to be related to the suppression of the athermal $\gamma \rightarrow \varepsilon$ martensitic transformation. Since the SFE is an essential parameter, there has been a considerable interest in determining its value for high-Mn steels (Idrissi *et al.*, 2010; Pierce *et al.*, 2012; Pierce *et al.*, 2014). These steels possess a stable fully austenitic microstructures in the SFE range of 20-30 mJ/m^2 or more (Schumann, 1972; Alder *et al.*, 1986; Mindownik, 1998; Yakubtsov *et al.*, 1999; Allain *et al.*, 2004a). C content of less than 1% lower the SFE to approximately ~ 22 mJ/m^2, while at higher C contents, the SFE is reported to increase (Yakubtsov *et al.*, 1999). The critical SFE regime to observe TWIP effect in high-Mn steels is still debated and there is a slight difference depending on the alloy compositions. Frommeyer *et al.* (2003) indicated that the SFE larger than ~ 25 mJ/m^2 will result in the TWIP effect in the stable austenite, while Allain *et al.* (2004b) presented a narrower range for SFE mediated twinning. On the other hand, Dumay *et al.* (2008) mentioned that below SFE ~18 mJ/m^2 twinning tends to disappear and is replaced by ε platelets and the SFE of ~ 20 mJ/m^2 is needed for the best strain hardening rate (SHR). Jin & Lee (2009) suggested that the SFE value ~33 mJ/m^2 is required to obtain twinning in Fe-18Mn-0.6C-1.5Al. De Cooman *et al.* (2011) measured that the SFE of Fe- 18Mn-0.6C-1.5Al high-Mn steel as ~ (30±10) mJ/m^2. Kim & De Cooman (2016) recently reported that the SFE required for the TWIP effect is ~ 13-40 mJ/m^2.

Pierce *et al.* (2015) investigated the influence of SFE on the microstructural and strain-hardening evolution of three (Fe-22/25/28Mn-3Al-3Si) TRIP/TWIP steels during RT tensile deformation. They observed SFE of the Fe-22/25/28Mn-3Al-3Si alloys increased from 15-39 mJ/m^2, with systematic the increase in Mn content and best combination of UTS and total elongation could be obtained for SFE 15-39 mJ/m^2. Their report also indicate that the strength and ductility decrease significantly above a SFE ~ 39 mJ/m^2, corresponding to a decrease in the incidence of mechanical twinning. SFE ~ 21 mJ/m^2 in Fe-25Mn-3Al-3Si results in a dislocation structure that exhibited both planar and wavy characteristics. It was further reported by them that a higher SFE ~ 39 mJ/m^2 in Fe-28Mn-3Al-3Si enhances greater dislocation cross slip and mobility, which reduces work-hardening in comparison to the lower SFE alloys.

1.3.2. The grain size of austenite

It is established that the grain size is closely related to mechanical behaviour of materials and the grain refinement is a suitable means of the microstructure control for strengthening a material without changing its chemical compositions (Ueji *et al.*, 2008). However, in fcc metals and alloys with low SFE such as high-Mn steels, the information concerning the range of the grain size effect on the both strength and ductility and the underlying deformation mechanism is still limited. It is accepted that grain refinement in high-Mn steels increases the threshold stress with some reduction in ductility (Scott *et al.*, 2005; Ueji *et al.*, 2008). Changes in grain size from 1 to 18 μm follow the Hall-Petch relationship, primarily affecting the threshold (i.e., initial yield) stress as shown in Fig. 1.5 (Scott *et al.*, 2005).

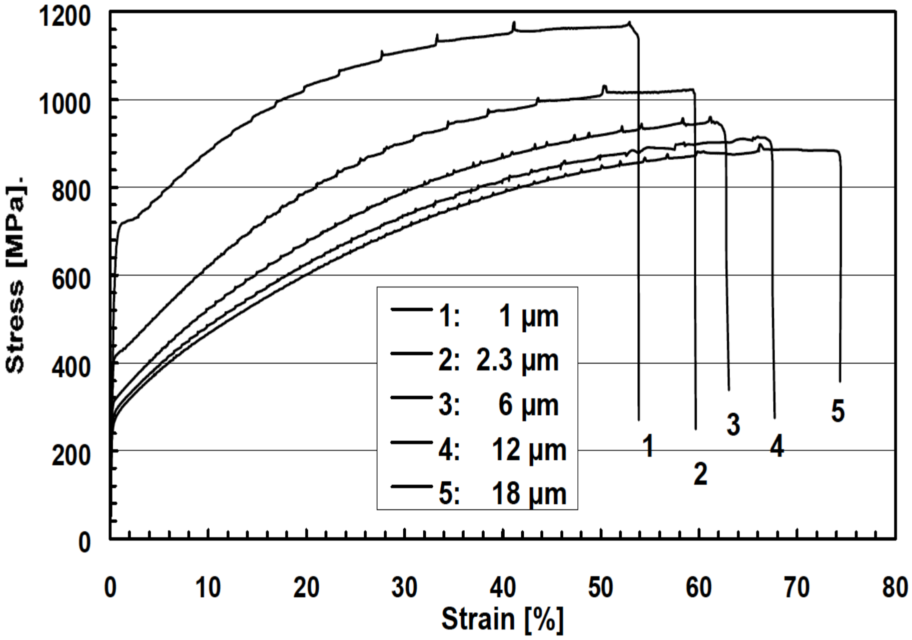

Fig. 1.5: Effect of grain size on tensile response of Fe-22Mn-0.6C (Scott *et al.*, 2005).

The dislocation substructures that form depend on the grain size, which in turn influences the twinning tendency of high-Mn steels (Gutierrez-Urrutia & Raabe, 2012a). Grain refinement in the μm range does not seem to suppress deformation twinning, at least in Fe-22Mn-0.6C (Gutierrez-Urrutia *et al.*, 2010). As grain size is increased, both the YS and UTS decreases according to Hall-Petch relationship, while ductility increases (De Cooman *et al.*, 2009) while that the Hall-Petch parameters for twinning are similar to that for slip (Gutierrez-Urrutia *et al.*, 2010). Ueji *et al.* (2008) reported that fine-grained (grain size $d = 1.8\mu m$) Fe-31Mn-3Al-3Si high-Mn steel show high strength with adequate ductility, as shown in Fig. 1.6, which differs from the case of the alloys with medium to high SFE. This observation suggests that the large ductility lies on not only the twinning but also in the suppressed dynamic recovery due to low SFE. It has been also reported that fine grain sizes may completely inhibit the formation of twin and martensite in low SFE materials (El-Danaf *et al.*, 1999; Asgari, 2004; Mohammed *et al.*, 2007). Furthermore, previous investigations with other fcc metals/alloys have suggested that the initiation of the twin requires a critical dislocation density i.e., the twin formation occurs after a given plastic strain and before the dislocation structure while investigating the grain size effects on the occurrence of deformation twins in high-Mn steels.

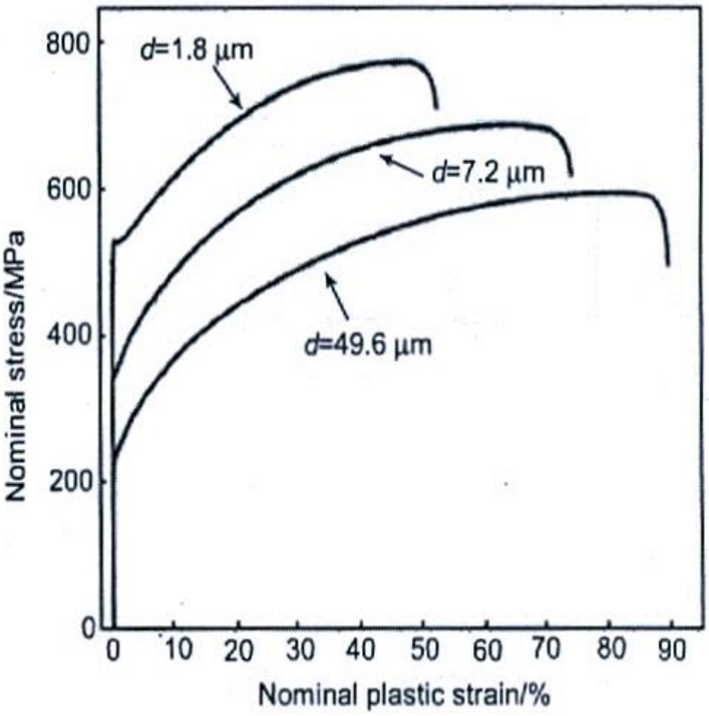

Fig. 1.6: Nominal stress strain curves of the Fe-31Mn-3Al-3Si high-Mn steel after 88% cold rolled and subsequently annealed at 700^{0}C ($d = 1.8\mu m$), 800^{0}C ($d = 7.2\mu m$), or 1000^{0}C ($d = 49.6\mu m$) for 1800s (Ueji., *et al.*, 2008).

Yoo *et al.* (2009) used Fe-28Mn-9Al-0.8C steel to investigate the factors affecting the tensile properties of high Fe-Mn-Al-C high-Mn steels. They observed that the strength increases and elongation decreases with decreasing grain size. The SHR of the fine-grained steel remained unchanged to the medium strain level but that of the coarse-grained steel continuously increased to a high strain level, resulting in exceptional ductility, as listed in Table 1.1. Their steel showed exceptionally high elongation with reasonably high strength. The YS and UTS increased with decreasing the grain size and the opposite trend was observed for elongation. The product of UTS and total elongation also decreased with decreasing the grain

Table: 1.1: RT tensile characteristics of Fe-28Mn-9Al-0.8C with three different grain size (Yoo *et al.*, 2009)

$d_A(d_{AT})$/μm	YS/ MPa	UTS/ MPa	Uniform elongation/%	Elongation /%	UTS*Elongation/MPa.%
5(3.5)	633	955	59.8	70.9	6.7710x10^4
8(6.7)	539	903	69.8	82.3	7.4317x10^4
38(14)	440	843	89.3	100.3	8.4553x10^4

size in spite of the increase of strength, indicating the elongation dominated tensile characteristics of the steel.

The representative engineering stress-strain curves of Fe-28Mn-9Al-0.8C steel used by Yoo *et al.*, 2009 having three different grain sizes are shown in Fig. 1.7(a). The grain size effect on strain hardening of the Fe-28Mn-9Al-0.8C steel can be seen in the plot of SHR against true strain superimposed on the true stress-strain curves in Fig. 1.7(b). The strain hardening rate of the fine grained (5 μm) steel remained constant up to a true strain of 0.3 and then decreased. By contrast, the SHR of the coarse-grained (38 μm) steel was lower than that of the fine-grained steel at the initial stage of plastic deformation but it increased continuously with increasing strain up to a true strain of 0.5, reaching the value close to that of fine-grained steel.

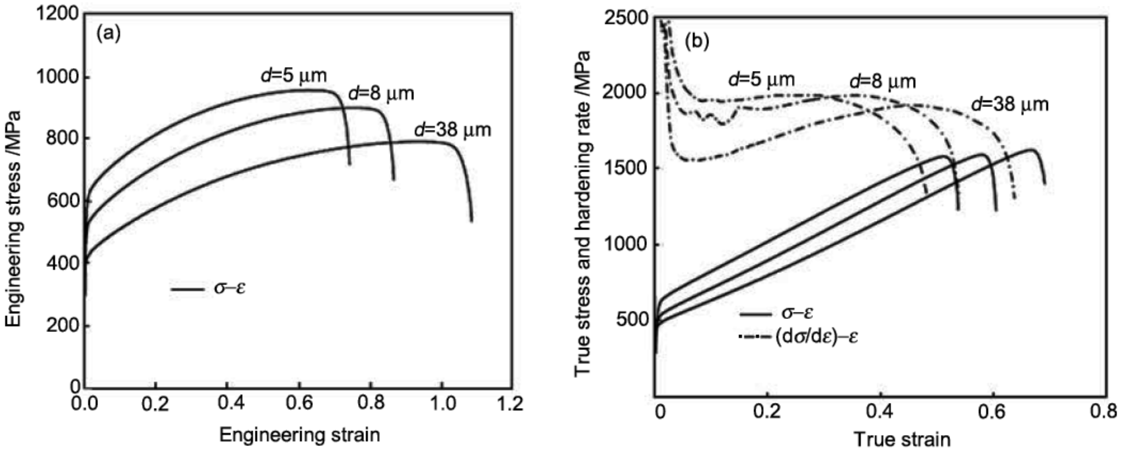

Fig. 1.7: The representative engineering stress-stress curve of Fe-28Mn-9Al-0.8C with three different grain sizes tested at 250°C with the initial strain of 10^{-3}s^{-1} (a), and the true stress-strain curves and the corresponding SHR as a function of true strain (b) (Yoo *et al.*, 2009).

Yoo & Park (2008) suggested that continuous increase of the SHR of high Mn Fe-Mn-Al-C austenitic steel, leading to the exceptionally high elongation of 100%, is attributed to the formation and intersection of the microbands consisting of geometrically necessary dislocations, i.e. they report about microband induced plasticity (MBIP). Microbands in the high-Mn Fe-Mn-Al-C austenitic steel are crystallographic in nature and usually run through the grain. Therefore, their length scale has the same order as the grain size (Wilsdorf, 1989; Hughes, 1993) Accordingly, it is plausible that strain hardening by MBIP is saturated early in the fine-grained steel compared to the coarse-grained steel.

1.3.3. The grain orientation of austenite

The initial grain orientation is also reported to have a pronounced influence on twinning and the development of the crystallographic texture. The effect of grain orientation on twinning has been given three different explanations, which are outlined schematically in Fig. 1.8.

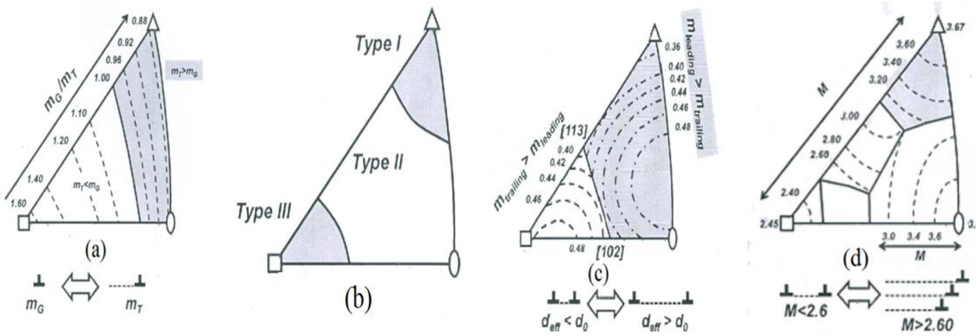

Fig. 1.8: (a) Schematic illustrating the effect of grain orientation on deformation twinning according to (Gutierrez-Urrutia & Raabe, 2011; Sato *et al*., 2011). (b) Orientation range of type I and type II grain, which behave as expected on the basis of their Schmid factor (c) Schematic illustrating the effect of grain orientation on deformation twinning according to Kireeva and Chemlyakov (Kuprekova *et al*., 2008; Kireeva & Chemlyakov, 2009;) (d) schematic illustrating the effect of grain orientation on deformation twinning according to (Beladi *et al*., 2011).

According to Gutierrez-Urrutia *et al.* (2010) and Sato *et al*. (2011), the effect of the grain orientation observed at low strain is governed by the relative value of the Schmid factor. They also proposed that twinning occurs when the resolved shear stress for twinning is less than the critical resolved shear stress for dislocation glide:

$$(\tau_c)_{twin} = \tau_{crss} = m_T\sigma_A < \tau_G = m_G\sigma_A \rightarrow m_T < m_G \qquad (1.2)$$

Where the Schmid factor has a conventional definition as the product of the cosines of the angles between the direction of the applied tensile stress (σ_A) and the slip plane normal and the direction of shear for a perfect dislocation (m_G) or a partial dislocation (m_T). This approach is mainly based on the observation that during uniaxial tensile deformation of high-Mn steels, a strong $\langle 111\rangle//t_d$ and a weak $\langle 100\rangle//t_d$ fiber orientations develop and Fig. 1.9 shows that while $\langle 111\rangle//t_d$ -oriented grains show profuse twinning, while the $\langle 100\rangle//t_d$ oriented grains are mostly twin-free. Electron channelling contrast imaging (ECCI) technique was used by Gutierrez-Urrutia & Raabe (2012b) to analyze Fe-22Mn-0.6C high-Mn steel

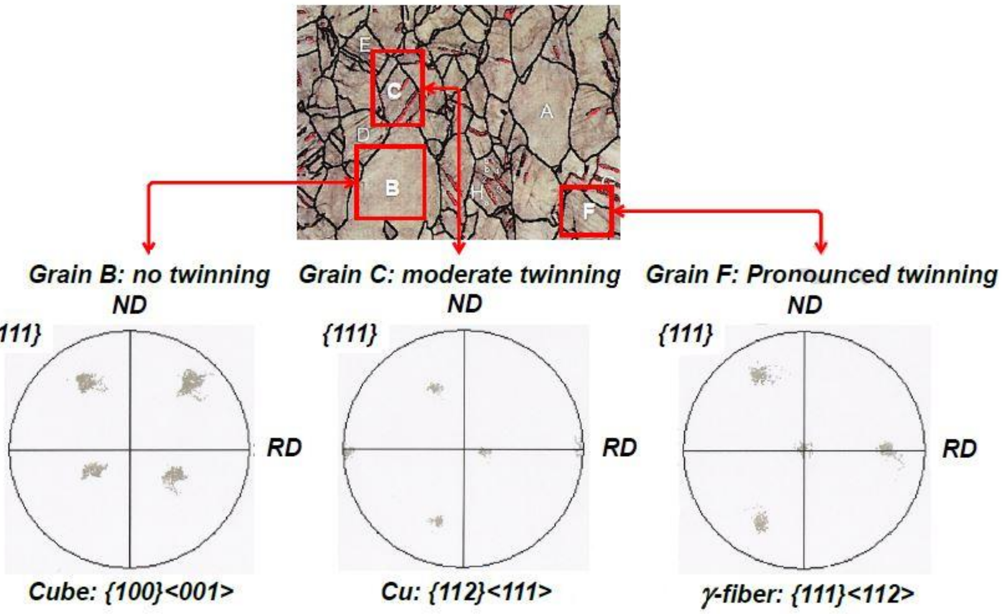

Fig. 1.9: Illustration of the influence of the grain orientation of twinning in a tensile sample of high-Mn steel strained to 59% engineering strain. The pole figures of the individual grains reveal that C-grain, which has a cube $\{100\}\langle 011\rangle$ orientation does not contain deformation twins, the B- grain which has Cu $\{112\}\langle 111\rangle$ orientation exhibits an intermediate twinning behaviour, and the f-grain which has $\{111\}\langle 112\rangle$ (gamma fibre) orientation is heavily twinned. Here RD and ND denote the rolling direction and normal direction respectively (Gutierrez-Urrutia & Raabe, 2012b)

(SFE=22 mJ/m^2), to evaluate the grain orientation dependence mechanism experimentally and showed that this strict Schmid law orientation dependence of slip and twinning in a tensile test does not hold practice. Only type I grains, which were favourably oriented for twinning due to their orientation very close to $\langle 111\rangle//t_d$, and type III grains, which were favourably oriented for dislocation glide with an orientation very close to $\langle 100\rangle//t_d$, behaved in a manner expected solely on the basis of their Schmid factor. Furthermore, type II grains, which cover a wide range of orientations unfavourable for twinning based on their Schmid factor, were also found to contain deformation twins. Gutierrez-Urrutia & Raabe (2012b) associated the deformation twinning in these unfavourably oriented grains with stress concentrations and strain gradients at grain boundaries.

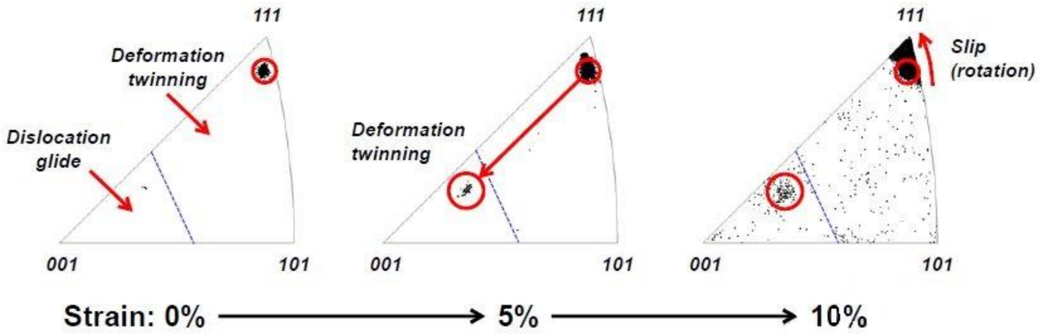

Fig. 1.10: Orientation changes within a single grain which an orientation close to $\langle 111\rangle//t_d$ Twinning is clearly seen to give rise to a volume reorientation. The initially Cu $\{112\}\langle 111\rangle$oriented grain twins easily to a CuT-$\{552\}\langle 115\rangle$orientation. In this new orientation, slip is preferred relative to deformation twinning. $\{111\}\langle 100\rangle$ dislocation slip results in a gradual rotation of grain towards the $\{001\}\langle 111\rangle$ line in the basic stereographic triangle. The dotted line separates the orientation for which twinning and dislocation glide are preferred deformation mode under uniaxial tension Yang *et al*. (2006).

Beladi *et al*. (2011) reports that while grains with an orientation close to the Goss and Cube orientation were free of mechanical twins, while those having an orientation close to the Brass or Cu, orientations were twinned. According to Beladi *et al*. (2011), the nucleation and growth of twins requires the activation of multiple slip systems and the presence of a high stress resulting from dislocation pile-ups. The confirmation of the hypothesis that multiple slip precedes twinning is provided by Yang *et al*. (2006) on texture development in a Fe-33Mn-3Al-3Si high-Mn steel during uniaxial tensile deformation. The very thin deformation twins formed did not contribute to texture evolution. The twinned volume was reoriented to CuT-$\{552\}\langle 115\rangle$, presented in Fig. 1.10, which is an orientation favoring slip. Yang *et al*. (2006) also reported that uniaxial tensile deformation resulted in a strong $\langle 111\rangle//t_d$ and a weak $\langle 100\rangle//t_d$ fiber orientation. Slip caused grain rotation towards the $\langle 111\rangle\langle 100\rangle$ line. They also noticed that tension along a $\langle 111\rangle//t_d$ type direction promoted twinning, in contrast to tension along $\langle 100\rangle//t_d$, which did not favor twinning

They report that orientations near those with the highest Schmid factor for twinning did not twin. Grains with $\langle 110\rangle//t_d$ orientations were seldom observed to contain twins even after an engineering strain as high as 20%, despite their high Schmid factors for twinning. Yang *et al.* (2006) suggested that there were two contributions of the TWIP effect to strain hardening: (a) the interaction between twin variants in the $\langle 111 \rangle$oriented grains and (b) the dislocation-dislocation interactions within the deformation twins, whose orientation favours dislocation glide.

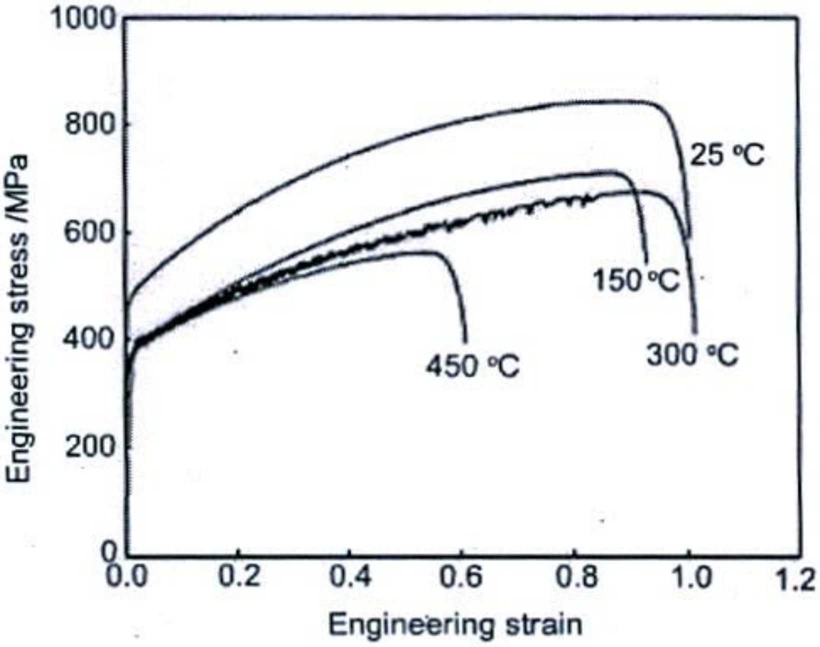

Fig. 1.11: The representative engineering stress-strain curves of the coarse grained Fe-28Mn-9Al-0.8C tested at various temperatures with the initial strain rate of $10^{-3}s^{-1}$ (Yoo *et al.*, 2009).

1.3.4. The deformation temperature

Increasing the deformation temperature generally has the effect of decreasing the strength and elongation of metals Considering the treatment of Allain (2004b), the SFE of Fe-25Mn- 3Si-3Al steel calculated by Wang *et al.* (2009), while emphasizing on the mechanical properties and the microstructure evolution between $25 - 400°C$. They observed that deformation twinning is the dominant deformation mechanism at $25°C \leq T \leq 100°C$ for $21 \leq SFE \leq 34$ mJ/m^2, while slip dominates for $SFE \geq 76$ mJ/m^2 at elevated temperatures ($T \geq 400°C$). The SFE value was estimated to decrease with decreasing temperature and a low SFE favored deformation twinning by inhibiting slip. Deformation twins formed during plastic deformation also behave as obstacles to dislocation movement, resulting in high strain hardening effect such that both high elongation and UTS can be observed at relatively low temperatures.

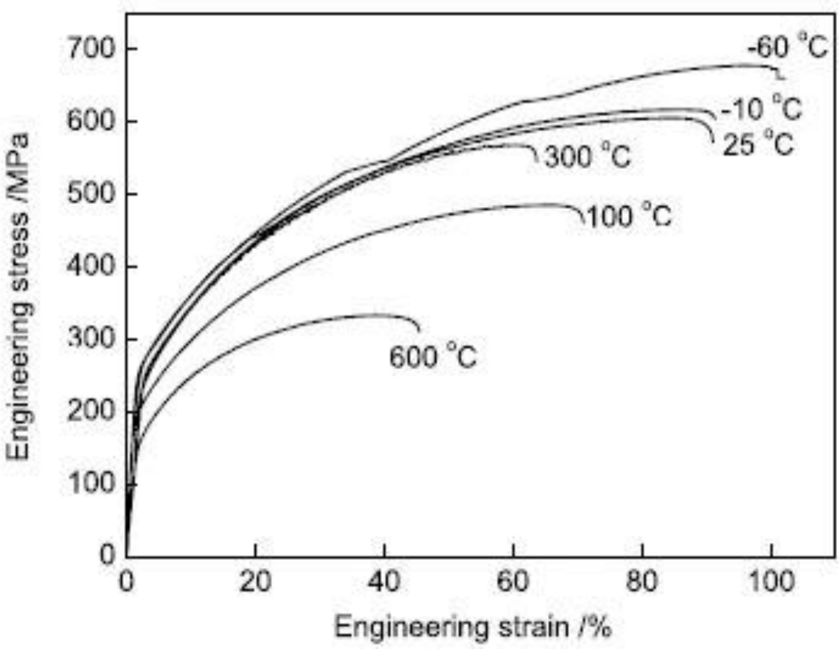

Fig. 1.12: Engineering stress-strain curves of Fe-23Mn-2Al-0.2C steel at different deformation temperature (Qin *et al*., 2011).

However, high-Mn steels with high Al and C contents exhibit an exceptional situation and that elongation does not decrease with increasing deformation temperature. Yoo *et al*. (2009) while studying the stress-strain curves of the coarse-grained Fe- 28Mn-9Al-0.8C steel

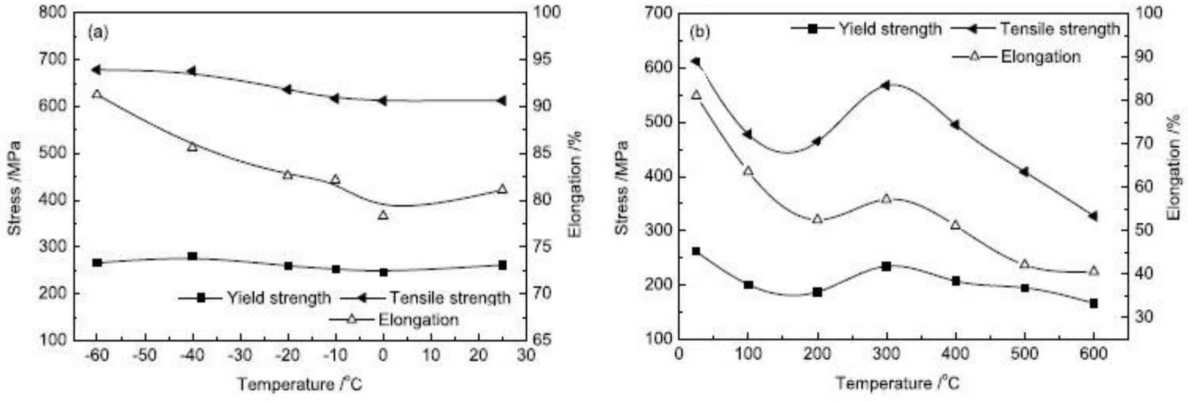

Fig. 1.13: Variations of the YS, tensile strength and elongation of Fe-23Mn-2Al-0.2C high-Mn steel with lower (a) and higher (b) deformation temperatures (Qin *et al*., 2011).

tensile-tested with a strain rate of $10^{-3}s^{-1}$at temperatures of $25 - 400$℃ reported that the YS in between $150 - 450$℃ was sensitive to the temperature with the value lower than that at 25℃ while the UTS decreased with increasing temperature (Fig.1.11). Their results are presented in Fig. 1.11 and show that except at 300℃, total elongation decreased with increasing temperature. Yoo *et al*. (2009) confirmed that the serrated flow occurring at $300°C$ is primarily attributed to interaction between dislocations-interstitial atoms rather than interaction between dislocations and substitutional atoms. Qin *et al.* (2011) studied the tensile deformation behavior of Fe-23Mn-2Al-0.2C high-Mn steel in a wide temperature range from $-60°C \leq T \leq 600°C$ (Fig. 1.12). Fig. 1.13 indicate that with increasing the deformation temperature, the strength and elongation to failure of the steel first decrease, then increase and finally decrease and the maximum values appearing at $300°C$. They also revealed that the SFE of the steel increases as deformation temperature increased from$-60°C \leq T \leq 600°C$ which changed the deformation mechanism from twining to slipping. They also revealed using electron microscopy that high-density deformation twins appearing at lower deformation temperatures gradually decrease with increasing temperature and only dislocations and dislocation cells appear in the microstructure at $600°C$.

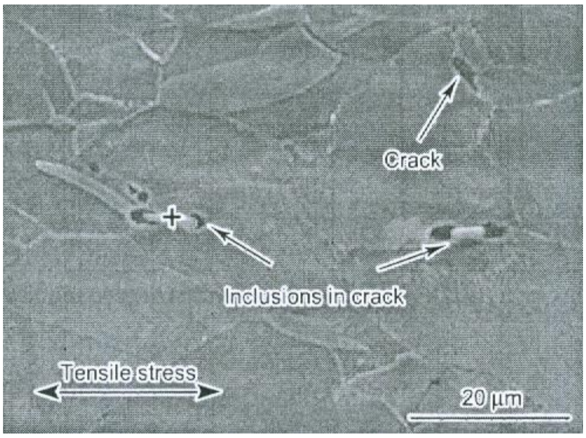

Fig. 1.14: SEM images showing microstructure of Fe-23Mn-2Al-0.2C high-Mn steel tensile deformed at 600^0C, "+" sign showing inclusion (Qin *et al.*, 2011).

The high incidence of deformation twins formed during low temperature deformation resulted in the high UTS and elongation of the studied steel. At $600°C$ some micro-cracks formed at the grain boundaries, as shown in Fig. 1.14, which was accompanied by AlN precipitates since AlN begin to precipitate at $600°C$ (Qin *et al.*, 2011).

1.4. A review on the grain size strengthening in high-Mn steels

In numerous publications, the yield stress, σ_{YS} of polycrystalline high-Mn steels was shown to follow the Hall-Petch relation, as described in Eq. (1.1) and its verification for various high-Mn steels is shown in Fig. 1.15. The literature data on the parameters σ_{YS}^0 and k_{YS}^{HP} for a number

Table 1.2: Parameters of the Hall-Peach relations for high-Mn steels

Alloys	σ^{0}_{YS} MPa	k^{HP}_{YS}, MPa $\mu m^{1/2}$	Reference
Fe-31Mn-3Al-3Si	53	764	Dini *et al.* (2010)
Fe-22Mn-0.6C	137	449	Bouaziz *et al.* (2011)
Fe-22Mn-0.6C	170	428	Scoot *et al.* (2011)
Fe-22Mn-0.6C	157	357	Gil Sevillano & Cuevas (2012)
Fe-20Mn-0.6C	158	485	Shen *et al.* (2016)
Fe-17Mn-0.45C-1.5Al-1Si (Hot rolled)	208	445	Gwon, (2017)
Fe-17Mn-0.45C-1.5Al-1Si (Hot rolled and recrystallization annealed)	403	445	Gwon, (2017)
Fe-15Mn-0.7C-2Al-2Si	305	330	Rahman *et al.* (2015)

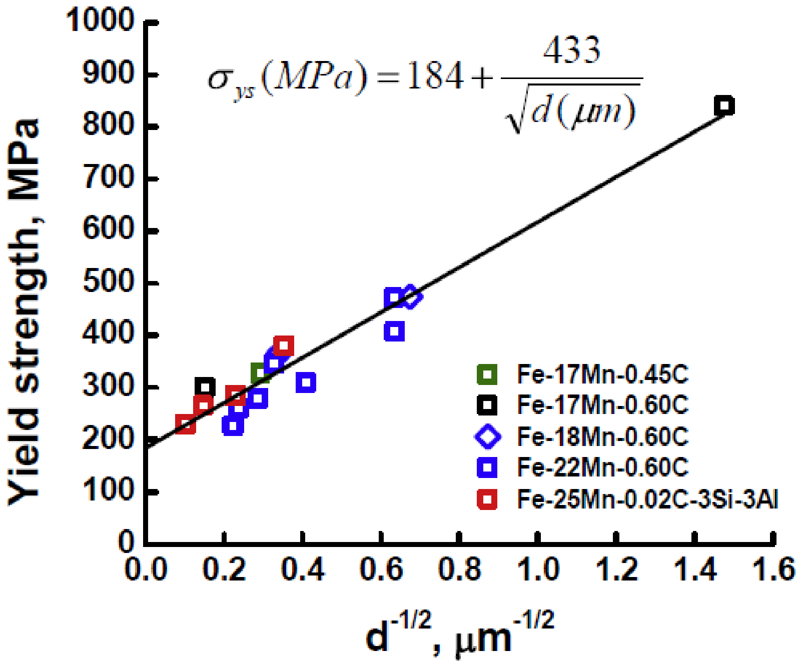

Fig. 1.15: Verification of the Hall-Petch relation for various high-Mn steels (Fe-22Mn-0.6C (Scott *et al.*, 2011), Fe-17Mn-0.45C (Gwon, 2017), Fe-25Mn-3Si-3Al-0.02C (Wang *et al.*, 2009), Fe-17Mn-0.6C (Yen *et al.*, 2012).

of high-Mn steels are reviewed in Table 1.2. (Dini *et al.*, 2010; Bouaziz, *et al.*, 2011, Scott *et al.*, 2011., Sevillano & Cuevas, 2012; Shen *et al.*, 2016; Gwon, 2017; Rahman *et al.*, 2015).

The reported values of σ_{YS}^{0} and k_{YS}^{HP} for polycrystalline Fe-22Mn-0.6C high-Mn steel are 132 MPa and 449 MPa μm$^{1/2}$ (14.2 MPa mm$^{1/2}$), respectively. However, the σ_{YS}^{0} value given by Bouaziz *et al.* (2011) in their original manuscript seems to have some discrepancy since the yield stress level is significantly lower than the value calculated using the parameters from the same reference. Therefore, the value of σ_{YS}^{0} for polycrystalline Fe-22Mn-0.6C steel was re-evaluated and a revised magnitude for σ_{YS}^{0} is 242 MPa was obtained by De Cooman *et al.* (2018), rather than 132 MPa, the value reported by Bouaziz *et al.* (2011). The corresponding critical resolved shear stress estimated was 79 MPa, assuming a Taylor factor of 3.06 (Bouaziz *et al.*, 2011). De Cooman *et al.* (2018) have derived the following Hall-Petch equations for the YS and the UTS for Fe-22Mn-0.5C-0.08N as:

$$\sigma_{YS}(MPa) = 219 + \frac{15.1 MPa\ mm^{1/2}}{\sqrt{d(mm)}} = 219 + \frac{477.5\ MPa\ \mu m^{1/2}}{\sqrt{d(\mu m)}} \qquad (1.3)$$

$$\sigma_{UTS}(MPa) = 754 + \frac{18.8 MPa\ mm^{1/2}}{\sqrt{d(mm)}} = 754 + \frac{594.5\ MPa\ \mu m^{1/2}}{\sqrt{d(\mu m)}} \qquad (1.4)$$

Kang *et al.* (2016) studied the influence of the C content on the Hall-Petch coefficient k_{YS}^{HP} using a slow cooling procedure to ensure equilibrium C segregation to the available grain boundary sites. They observed that k_{YS}^{HP} increased from 218 MPa μm$^{1/2}$ to 344 MPa μm$^{1/2}$ when the C content was increased from 0.3 mass-% to 0.6 mass-%. Two possible explanations for this pronounced increase of k_{YS}^{HP} was offered and that the effect may be associated either with an increased stress for the activation of dislocation sources in a grain when the C content is increased. Another suggested possibility was that an increased density of grain boundary ledges acting as dislocation sources (Li & Chou, 1970). The second explanation is criticized by De Cooman *et al.* (2018) as the mechanism would result in a decrease of k_{YS}^{HP} upon an increase in C.

The Hall-Petch diagram for high-Mn steels can be affected by alloying additions, as demonstrated in Fig. 1.16 for the case of alloying high-Mn steels with Ti, V, and Ni. The amount of pre-strain at during the measurements are also important, while the slope k_{YS}^{HP} of the Hall-Petch diagram decreases with increasing strain for a-Fe and ferritic steels, it increases with strain for austenitic steels. The latter trend is also observed for high-Mn steels. Gil Sevillano (2009) and de las Cuevas *et al.* (2010) reported a Hall-Petch slope of about 350 MPa μm$^{1/2}$ for the YS, and a Hall-Petch slope of 630 MPa μm$^{1/2}$ for the UTS. The results of Wang *et al.* (2009)

for Fe-24.8Mn-0.022C-3.17Si-3.12Al validates that the Hall-Petch slope is higher for the UTS ~ 638 MPa $\mu m^{1/2}$, while it is ~ 568 MPa $\mu m^{1/2}$ for the YS.

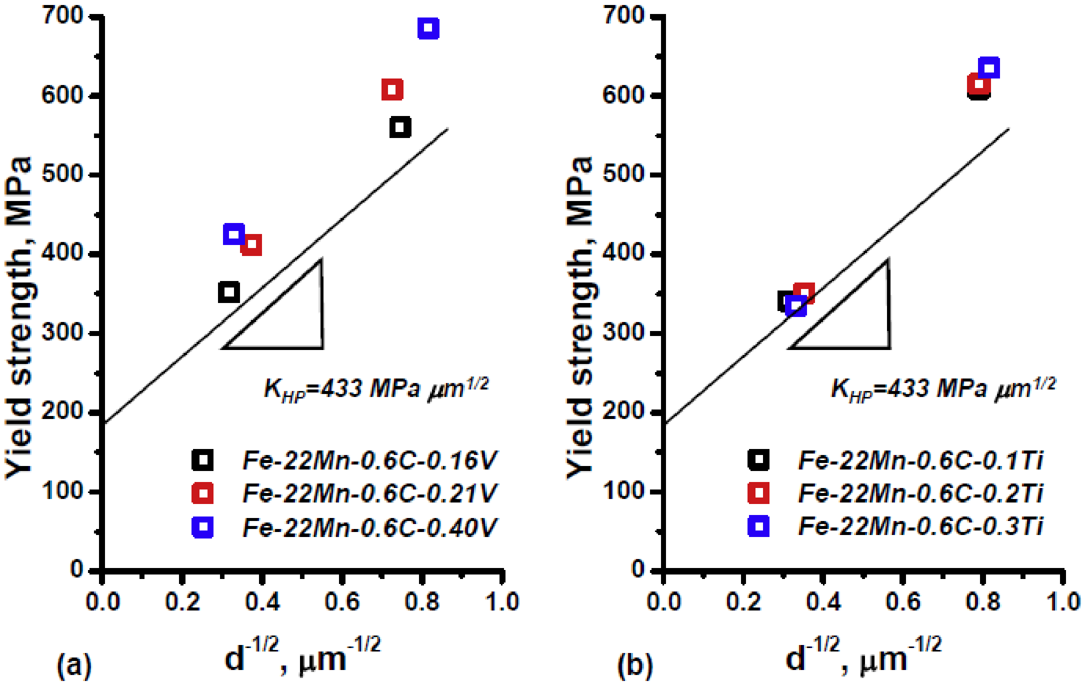

Fig. 1.16: Influence of micro-alloying additions of (a) V and (b) Ti on the Hall-Petch diagram for high-Mn steel (Scott *et al.*, 2011, Gwon, 2017).

It is generally accepted that grain refinement down to the submicron grain size, 100 nm < d < 1 µm, results, with a few exceptions, in a reduction of strain hardening and hence lowered uniform tensile elongation (Valiev *et al.*, 2006; Estrin & Vinogradov, 2013). Plasticity as such is not suppressed, as the ultrafine grained (UFG) materials sustain a large post-uniform elongation in the necking region. High-Mn steels do not appear to be susceptible to a negative influence of small grain size on the uniform elongation. Grain growth after recrystallization annealing makes it possible to obtain a broad grain size range for a high-Mn steel. Ueji *et al.* (2007, 2008) reported that grain size reduction in C-free Fe-31Mn-3Al-3Si high-Mn steel (with SFE ~ 42 mJ/m^2) resulted in a strong inhibition of deformation twinning and a significant drop in ductility. In fine grained high-Mn steel twinning was still prevalent in grains oriented with a ⟨111⟩ direction close to the tensile axis. Gutierrez-Urrutia *et al.* (2010) report that grain refinement did not suppress deformation twinning in a Fe-22Mn-0.6C high-Mn steel (intrinsic SFE ~ 23 mJ/m^2) altogether, but made it more difficult. They also associated the smaller grain size obtained to a reduction of the twin volume fraction. Lee *et al.* (2012) compared the tensile deformation behavior of UFG C-free Fe-17Mn and Fe-17Mn-0.6C high-Mn steels with that of the C-added high-Mn steel and concluded that the grain refinement induced reduction in elongation was smaller for the latter. It should be noted that high-Mn steels with the grain size down to about 2 μm still retained a large uniform elongation of approximately 50% engineering strain. In a recent work (Timokhina *et al.*, 2014) the properties of a Fe-22.3Mn-0.19Si-0.14Ni-0.27Cr-0.61C high-Mn steel deformed by equal channel angular pressing (ECAP) were investigated. It was shown that a good balance between strength (1702 MPa) and tensile elongation (24%) in the steel with a resulting UFG structure can be achieved by a suitable choice of the processing schedule. This was associated with the formation of deformation microbands and twins (including nano-twins) in the microstructure during the ECAP processing.

1.5 Aims and scopes of the dissertation

The previous discussion on the interpretation of deformation microstructure of high-Mn austenitic steels have clearly identified the importance of TWIP effect steels in revealing high strength and superior plasticity required for weight reduction of automotive structures and components (De Cooman *et al.*, 2018). Until now, three types of high-Mn steels, namely, Fe-Mn-C (Idrissi *et al.*, 2010), Fe-Mn-Al-C (Jin & Lee, 2012) and Fe-Mn-Si-Al (Idrissi *et al.*, 2013) have been investigated. Among these three types, Fe-Mn-Al-C remained the most investigated class for possessing a good strength and ductility combination achievable through austenite SFE control by Al adjustment in the steel (De Cooman *et al.*, 2018). Deformation twinning is profound in the coarser-grained high-Mn steels, and majority of investigations with high-Mn steels emphasize on the nucleation and growth of twins in coarse-grained structures, while similar attention has not been paid to the origin of suppression of twinning in fine-grained high-Mn steels. Generally, the strain hardening behavior is interpreted in terms of TWIP effect, overlooking the role of dislocation plasticity (De Cooman *et al.*, 2018), while some recent reports indicate that the TWIP effect is overestimated (Liang *et al.*, 2016; Luo & Huang, 2018; Zhi *et al.*, 2020).

Although the prevalence of deformation twinning in fcc metals/alloys including the high-Mn steels are often related to their low SFE, a second important, but poorly understood factor is the grain size (De Cooman *et al.*, 2018). The grain size is generally considered to influence on the dislocation glide, stacking fault (SF) formation and deformation twinning (De Cooman *et al.*, 2018). Interestingly, there are also reports of an unexpected influence of the grain size on intrinsic SFE of the material, particularly in the high-Mn steels, which could also indirectly affect the twinning tendency of these steels (De Cooman *et al.*, 2018). Volosevich *et al.* (1976) first reported about such an effect of the grain size on SFE of binary Fe-Mn alloys, which was later advocated by Takaki *et al.* (1993) and Lee and Choi (2000). Such a proposition is based on the grain size dependent internal stresses that cause a change in the dislocation dissociation width of the $\frac{a}{2}\langle 110\rangle$ dislocations. This is also recently validated directly using TRIP for high-Mn steels having different grain sizes (Chen *et al.*, 2021).

The contribution of the dislocations to strain hardening is often underestimated in high-Mn steels, for they have an inherently low intrinsic SFE – ranging between 20-40 mJ/m^2, which promotes planar slip of dislocations and suppress any cross-slip (De Cooman *et al.*, 2018). However, some previous investigations on high-Mn steels having higher SFE have indicated the importance of dislocation plasticity for obtaining good strain hardening, indicating that cross-slip dominates the plasticity mechanism (Gutierrez & Raabe, 2012; Liang *et al.*, 2016). Moreover, under a twinning destitute condition, various dislocation activities such as cross-slip, organized dislocation substructure formation, etc., emerge as the prevalent factor controlling the deformation of such steels – either individually or collectively (Luo & Huang, 2018). But those previous studies (Gutierrez & Raabe, 2012; Liang *et al.*, 2016) do not deal in detail with the exact cause of enhancement of dislocation plasticity, as well as the conditions to observe suppression of twinning. Cross-slip as an important aspect of dislocation plasticity is generally predominant in stage C hardening, which is commonly known to be associated with dynamic recovery and consequent lowering in the dislocation storage capacity of the matrix (Friedel, 1964; Nabarro, 1967; Hirsch, 1975). However, an interesting different proposition concerning cross-slip is that it can also cause strain hardening by increasing the dislocation storage capacity of the matrix in lightly deformed crystals (Nabarro *et al.*, 1964; Jackson, 1983). According to this proposition, cross-slip, if activated in the early stages of deformation, results in growth of dipolar and/or multipolar dislocation structures that subsequently transform to more complicated dislocation substructures with increasing deformation (Jackson, 1983).

The existing literature emphasizing the role of dislocation plasticity over twinning in high-Mn steels claims that the primary deformation mode is the formation of complex substructures induced by cross-slip (Fu *et al.*, 2018; Kim *et al.*, 2019). However, the actual mechanisms engendering the dislocation substructure formation in high-Mn steels are still lacking (Kubin & Kratochvíl, 2000). In this work, we aim to clarify the mechanism underlying the dislocation movements that produce cross-slip induced dislocation plasticity in a fine-grained high-Mn steel. The objective of this dissertation is to provide fundamental insights into the mechanism of dislocation plasticity in high-Mn steels, reported in the literature (Luo & Huang, 2018; Fu *et al.*, 2018; Kim *et al.*, 2019) based on diffraction based characterization techniques like: electron channelling contrast imaging (ECCI) in a scanning electron microscope (SEM) having electron backscattered diffraction (EBSD) facility, X-ray line profile analysis (XLPA) and transmission electron microscopy (TEM); are very strong techniques to interpret the deformation microstructures in terms of various microstructural defect parameters in metals/alloys – estimated in different length scales either indirectly or directly. They offer true picture of the active plasticity mechanisms in the concerned system. In the present dissertation, EBSD, TEM and XLPA is used to investigate the defect substructures in a fine-grained Fe-Mn-Al-C steel (grain size ~ 5 µm), tensile strained at RT. The selection of grain size is based on the existing deliberation that grain refinement would reduce deformation twinning, while enhancing dislocation-mediated plasticity (Ueji *et al.*, 2008; De Cooman *et al.*, 2018). The objective is to systematically study the evolution of deformed microstructures at various levels of imposed strain, while interpreting the strain hardening behavior of the steel and the associated plasticity mechanism(s) with an emphasis on the exact dislocation manoeuvrings responsible for the dislocation dominated plasticity – when the steel is not expected to show pronounced twinning. Furthermore, the underlying plasticity mechanism in the fine-grained steel is substantiated from comparison to that of a coarse-grained counterpart that revealed profound deformation twinning.

References

Adler, P.H., Olson G. B. & W. S. Owen. (1986). *Metall. Trans. A.* **17**, 1725-1737.

Allain, S, Chateau, J. P., Bouaziz, O., Migot, S. & Guelton, N. (2004a). *Mater.Sci. Eng. A.* **387-389**, 143-147.

Allain, S., Chateau J. P., Bouaziz, O., Migot, S. & Guelton N. (2004b). *Mater.Sci. Eng. A.* **387-389**, 158-162.

Armstrong, R. W. (2014) *Mater. Trans.* **55**, 2-12.

Beladi, H., Timokhina, I. B., Estrin, Y., Kim, J., De Cooman, B. C. & Kim S. K. (2011). *Acta Mater.* **59**, 7787-7799.

Bhadeshia, H. K. D. H. (2010) *Proc. R. Soc. Lond.* A. 466, 3-18.

Bouaziz, O., Allain, S., Scott, C., Cugy, P., Barbier, D. (2011) *Curr. Opin. Solid. St. M.* **15,** 141-168.

Chen, J., Dong, F., Liu, Z., & Wang, G. (2021) *J. Mater. Res. Technol.* **10**, 175-187.

Choi, K., Seo, C. H., Lee, H., Kim, S. K., Kwak, J. H., Chin, K. G., Park, K. T. & Kim, N. J. (2010) *Scr. Mater.* **63**, 1028-1031.

Cordero, Z. C., Knight, B. E. & Schuh, C. A. (2016) *Int. Mater. Rev.* **61**, 495-512.

De Cooman, B. C., Chen, L., Kim, H. S., Estrin, Y., Kim, S. K. & Voswinckel, H. (2009). *State of the science of high manganese twip steels for automotive applications, Microstructures and texture in steels*, ch.10. Haldar A., Suwas, S. & Bhattacharjee, D. eds., Springer.

De Cooman, B. C., Estrin, Y. & Kim, S. K., (2018) *Acta Mater.* **142**, 283-362.

De Cooman, B.C., Chin, K.G. & Kim, J.Y. (2011) *New Trends and Developments in Automotive System Engineering*, Ed. M. Chiaberge, Publisher: InTech, Rijeka, Croatia.

De Cooman, B.C., Estrin, Y. & Kim, S.K. (2018) *Acta Mater.* **142**, 283-362.

Diehl, J. (1956) *Z. Metall.* **47**, 331.

Dini, G. & Ueji, R. (2012) *Steel Res. Int.* **83**, 374-378.

Dini, G., Najafizadeh, A., Ueji, R. & Monir-Vaghefi, S.M. (2010) *Mater. Des.* **31**, 3395-3402.

Dumay, A., Chatau, J.P., Allain, S., Migot, S. & Bouaziz, O. (2008). *Mater. Sci.Eng. A.* **483-484**, 184-187.

El-Danaf, E., Kalidindi, S. R. & Doherty, R. D. (1999). *Metall. Mater. Trans. A.* **30A,** 1223-1233.

Estrin, Y. & Vinogradov, (2013) A. *Acta Mater.* **61**, 782-817.

Fan, D. W., Kim, H. S. & De Cooman, B. C. (2009) *Steel Res.Int.* **80,** 241-248.

Friedel, J.(1964) Dislocations, Pergamon, Oxford, , pp 264.

Frommeyer, G. & Brux, U. (2006) *Steel Res. Int.* **77**, 627-633.

Frommeyer, G., Brüx, U., & Neumann, P. (2003). *ISIJ Int.*, **43**, 438-446.

Frommeyer, G., Drewes, E. J. & Engl, B. (2000) *Rev. Metall. Cah. Inf. Tech.* **97**, 1245-1253.

Fu, X., Wu, X. & Yu, Q. (2018) *Mater. Today Nano.* **3**, 48-53.

Gleiter, H. (1989) *Prog. Mater. Sci.* **33,** 223-315.

Grassel, O., Kruger, L., Frommeyer, G. & Meyer, L. W. (2000) *Int. J. Plast.* **16,** 1391-1409.

Gutierrez-Urrutia, I. & Raabe, D. (2011). *Acta Mater.* **59**, 6449-6462.

Gutierrez-Urrutia, I. & Raabe, D. (2012) *Acta Mater.* **60**, 5791-5802.

Gutierrez-Urrutia, I. & Raabe, D. (2012a). Scr. *Mater.* **66**, 992-996.

Gutierrez-Urrutia, I. & Raabe, D. (2012b). *Mater. Sci. Forum.* **702-703**, 523-529.

Gutierrez-Urrutia, I. & Zaefferer, S., Raabe, D. (2010) *Mater. Sci. Eng.* A. **66**, 3552-3560.

Gwon, H. MS Thesis, Pohang University of Science and Technology, South Korea, 2017.

Hall, E. O. (1951) *Proc. Phys. Soc. Lond.* B. **64**, 747-753.

Hamada, A. S. & Karjalainen, L. P. (2006) *Can. Metall. Q.* **45,** 41-48.

Herrmann, J., Inden, G. & Sauthoff, G. (2003) *Acta Mater.* **51,** 2847-2857.

Hirsch, P. B.(1975) The Physics of Metals, P. B. Hirsch (ed.), Cambridge University Press, Cambridge, , pp. 193.

Hughes, D.A. (1993). *Acta Metall. Mater.* **41**, 1421-1430.

Idrissi, H., Renard, K., Ryelandt, L., Schryvers, D. & Jacques P. J. (2010). *Acta Mater.* **58**, 2464-2476.

Idrissi, H., Renard, K., Schryvers, D., Jacques, P.J. (2013) *Philos. Mag*. **93**, 4378-4391.

Jackson, P. J. (1983) *Mater. Sci. Eng*. **57**, 39-47.

Jang, J. H., Lee, C. H., Heo, Y. U. & Suh, D. W. (2012) *Acta Mater.* **60,** 208-217.

Jin, J.E. & Lee, Y.K. (2009). Mater. Sci. Eng. A. 527, 157-161.

Jin, J.-E. & Lee, Y.-K. (2012) *Acta Mater.* **60**, 1680-1688.

Kang, J.-H., Duan, S., Kim, S.-J., Bleck, W. (2016) *Metall. Mater. Trans*. A. **47**, 1918-1921.

Kang, S., Jung, J. G., Kang, M., Woo, W. & Lee Y.K. (2016) *Mater. Sci. Eng*. A. **652**, 212-220.

Kim, J.K. & De Cooman, B. C. (2016). *Mater. Sci. Eng. A.* **676**, 216-231.

Kim, S.-D., Park, J. Y., Park, S.-J., Hoon Jang, J., Moon, J., Ha, H.-Y., Lee, C.-H., Kang, J.-Y., Shin, J.-H., Lee, T.-H. (2019) *Sci. Rep*. **9**, 1-13. 15171.

Kireeva, I.V., & Chumlyakov, Yu. I. (2009). *Phys. Met. Metallogr*. **108**, 298-309.

Kubin, L.P., & Kratochvíl, J. (2000) *Philos. Mag*. A. **80**, 201-218.

Kuhlmann-Wilsdorf, D. (2001) *Mater. Sci. Eng*. A. **315**, 211-216.

Kuprekova, E. I., Chumlyakov, Yu. I. & Chernov, I. P. (2008*). Met. Sci. Heat. Treat*. **50**, 282-288.

Lee, P. Y., Chiu, C. S., Gau,Y. J. &Wu, J. K. (1992) *High Temp. Mater. Proc.* **10,** 141-144.

Lee, T., Koyama, M. Tsuzaki, K., Lee, Y.-H., Lee, C.S. (2012) *Mater. Lett*. **75**, 169-171.

Lee, Y.-K. & Choi, C. (2000) *Metall. Mater. Trans*. A. **31**, 355-360.

Lee, Y.-K. (2012) *Scr. Mater*. **66**, 1002-1006.

Li, J. & Chou, Y. (1970) *Metall. Mater. Trans*. **1**, 1145.

Li, Y., Bushby, A. J., Dunstan, D. J. (2016) *Proc. R. Soc.* A. **472**, 20150890.

Liang, Z. Y., Li, Y. Z. & Huang, M. X. (2016) *Scr. Mater*. **112**, 28-31.

Luo, Z. C. & Huang, M. X. (2018) *Scr. Mater*. **142**, 28-31.

Mahajan, S. & Chin, G.Y. (1973). *Acta Mater*. **21**, 1353-1363.

Miodownik, A.P. (1998). Z. *Metallkunde***. 89**, 840-847.

Mohammed, A. A. S., El-Danaf, E. A. & Radwan, A. A. (2007). *Mater. Sci. Eng. A*. **457**, 373-379.

Morris, D. G., Munoz-Morris, M. A. & Requejo, L. M. (2006) *Acta Mater.* **54,** 2335-2341.

N. J. Petch. (1953). *J. Iron. Steel. Inst.* **174**, 25-28.

Nabarro, F. R. N.(1967) Theory of Crystal Dislocations, Oxford University Press, Oxford, , pp. 260.

Nabarro, F. R. N., Basinski, Z. S. & Holt, D. B. (1964) *Adv. in Phys*. **13**, 193-323.

Naik, S. N. & Walley, S. M. (2019) *J. Mater. Sci*. **55**, 2661-2681.

Olson, G. B. & Cohen, M. (1976a) *Metall. Trans.* A. **7,** 1897-1904.

Park, K. T. (2013) *Scr. Mater*. **68**, 375-379.

Park, K. T., Jin, K. G., Han, S. H., Hwang, S. W., Choi, K. & Lee, C. S. (2010) *Mater. Sci. Eng*. A. **527**, 3651-3661.

Pierce, D. T., Bentley, J., Jiménez, J. A. & J. E. Wittig. (2012). *Scr. Mater.* **66**, 753-756.

Pierce, D. T., Jimenez, J. A., Bantley, J., Raabe, D. & Witting, J.E. (2015). *Acta Mater*. **100**, 178-190.

Pierce, D.T., Jimenez, J. A., Berntley, J., Raabe, D., Oskay C. & Witing, J.E. (2014). *Acta Mater.* **68**, 238-253.

Qin, X.M., Chen, L.Q., Di, H.S. & Deng, W. (2011). *Acta Metall. Sin*. **47**,1117.

Remy, L. & Pineau, A. (1977) *Mater. Sci. Eng*. **28**, 99-107.

Rolltt, A.D. & Kocks, U. F. (1993) *Solid State Phenom.* **35-36**, 1-18.

Sato, Y. S., Kwon, E.P., Imafuku, M., Wagatsuma K., Suzuki, S. (2011). *Mater.Character.* **62**, 781-888.

Saxena, V. K., Krishna, M. S. G., Chhaunker, P. S. & Radhakrishnan, V. M. (1994) *Int. J. Press. Vessels Pip.* **60,** 151-157.

Schumann, V.H. (1972). *NeueHütte*. **17**, 605-609.

Scott, C., Guelton, N., Allain, S. & Faral, M. (2005). *Mater. Sci. Technol. Conf.*, **2**, 127-138.

Scott, C., Remy, B., Collet, J.-L., Cael, A., Bao, F. Danoix, C., Malard, B. Curfs, C. (2011) *Int. J. Mater. Res.* **102**, 538-549.

Sevillano, J.G. & de Las Cuevas, F. (2012) *Scr. Mater.* **66,** 978-981.

Sevillano, J.G. (2009) *Scr. Mater*. **60**, 336-339.

Shen, Y., Jia, N., Misra, R., Zuo, L. (2016) *Acta Mater*. **103**, 229-242.

Shih, S. T., Tai, C. Y. & Perng, T. P. (1993) *Corrosion* **49,** 130-134.

Takaki, S., Nakatsu, H. & Tokunaga, Y. (1993) *Mater. Trans. JIM.* **34**, 489-495.

Timokhina, I., Medvedev, A., Lapovok, R., (2014) *Mater. Sci. Eng*. A. **593**, 163-169.

Ueji, R., Tsuchida, N., Fujii, H., Kondo, D., Kunishige, K. (2007) *J. Jpn. I. Met*. **71**, 815-821.

Ueji, R., Tsuchida, N., Terada, D., Tsuji, N., Tanaka, Y., Takemura, A. & Kunishige, K. (2008) *Scr. Mater*. **59**, 963-966.

Valiev, R.Z., Estrin, Y., Horita, Z., Langdon, T.G., Zechetbauer, M.J., Zhu, Y.T. (2006) JOM **58,** 33-39.

Volosevich, P., Gridnev, V. & Petrov, Y. (1976) *Phys. Met. Metallogr*. **42**, 126-130.

Wang, X. D., Huang, B. X., & Rong, Y. H. (2006). *Mater. Sci. Eng*. A, **438-440**, 300-305.

Wilsdorf, D. K. (1989). *Mater. Sci. Eng. A*, **113**, 1-41.

Yakubtsov, I. A., Airapour, A. & Perovic, D. D. (1999). *Acta Mater*. **47**, 1271-1279.

Yang, P., Xie, Q., Meng, L., Ding, H. & Tang, Z. (2006). *Scr. Mater*. **55**, 629-631.

Yoo, J. D. & Park, K. T. (2008) *Mater. Sci. Eng*. A. **496**, 417-424.

Yoo, J. D., Hwang, S. W. & Park, K. T. (2009). *Mater.Sci. Eng. A*, **508**, 234-240.

Yoo, J. D., Hwang, S. W. & Park. K. T. (2009). *Metall. Mater. Trans. A*, **40A**,

Zhi, H., Zhang, C., Antonov, S., Yu, H., Guo, T., Su, Y. (2020) *Acta Mater*. **195**, 371-382.

Zhu, X. M. & Zhang, Y. S. (1998) *Corrosion*, **54,** 3-12.

Chapter 2

Methodologies adopted for interpretation of deformation microstructures

2.1 Assessment of extended defects in the microstructure and the underlying principles

To study different types of lattice imperfections, there are various methods which have been reviewed by Bryne (1965). In the present research work transmission electron microscopy (TEM), electron backscatter diffraction (EBSD), X-ray diffraction (XRD) and Electron channelling contrast imaging (ECCI) analysis are used to interpret the deformation microstructure of the Fe-26Mn-1Al-0.14C high-Mn steel under different conditions. The underlying principles of the respective methodologies are described briefly in following sections.

2.2 X-ray diffraction

X-ray diffraction (XRD) is used to study the microcrystalline properties and the nature of imperfections of materials during growth and plastic deformations. X-ray diffraction is a scattering phenomenon. When X-rays interact with the atoms, scattering in all directions is occurred. Bragg derived a theory to explain the patterns which was observed when X-rays were scattered from crystalline materials. In this model, each plane of atoms acts as a source of scattered radiation and when the distance between the sources is comparable to the wavelength of the radiation, diffraction effect is observed. When X-rays interact with atoms, it gives rise to scattering in all directions; in some of those directions the scattered beams will be completely in phase and so reinforce each other to form diffracted beams following Bragg’s law,

$$2d_{hkl} \sin\theta = n\lambda \qquad (2.1)$$

where, λ is the wavelength of X-rays directed towards the set of (hkl) parallel planes. d_{hkl} is the distance between identical planes in a crystal and n is the order of reflection, θ is called Bragg angle where the maximum intensity occurs. Fig. 2.1 showing the schematic presentation of Bragg’s law. In an ideal crystal individual set of interplanar spacing d_{hkl} is present for each crystallographic phase which produces a particular diffraction pattern at the corresponding Bragg angle. Some crystal impurities are always present in real crystal and an incident beam is not perfectly parallel and monochromatic. Due to this in real experiments broad peaks are observed instead of sharp lines.

Diffraction line profile analysis is one of the important applications of powder diffraction to study the nature of crystal imperfections. It is known from XRD studies that

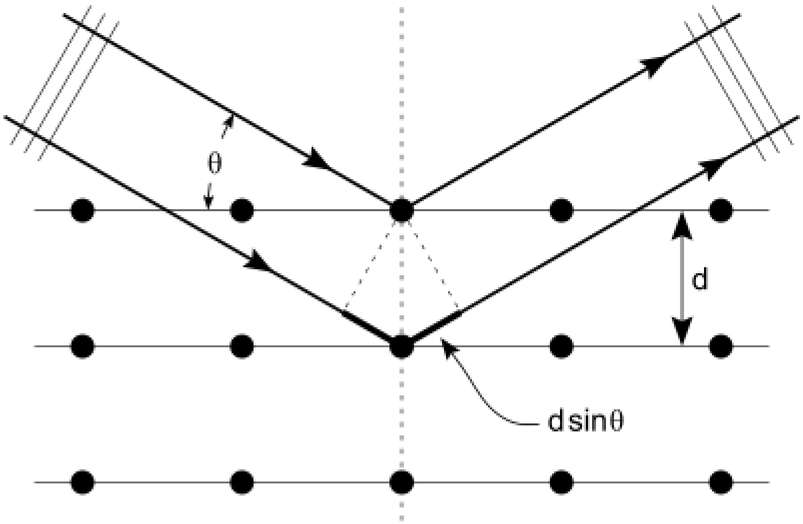

Fig. 2.1: Schematic representation of the Bragg’s law.

plastic deformation induces broadening of the XRD profiles and when the sample is more and more deformed, the peak broadening increases. Broadening of line profiles causes mainly due to small crystallite size, microstrain inside the crystallites and SFs. Some instrumental parameters like slit widths, sample size, penetration in the sample, imperfect focusing, unresolved α_1 and α_2 peaks etc. are also responsible for some extraneous broadening of the line profile. These extraneous sources of broadening are called “instrumental broadening”. Scherrer (Scherrer, 1918) proposed the idea of determination of crystallite size from X-ray line profile and reported that the line breadth is inversely proportional to the size of the crystallites according to the equation,

$$\beta = \frac{K_S\lambda}{D\cos\theta} \tag{2.2}$$

known as Scherrer formula, where λ is the X-ray wavelength, β is the line breadth, θ is the Bragg angle, K_S is Scherrer constant (1.0 > K_S > 0.89) and D is an apparent crystallite size, depends on the measure of breadth, the direction of hkl planes and the shape of the crystallite size. From Eq. (2.2) the length of crystal in the direction of the diffraction planes can be measured and this equation shows that size broadening is independent of the order of reflection. In the Scherrer formula instrumental broadening is totally neglected. This formula is not valid for the study of crystals where the strain broadening is present. Due to these all disadvantages Scherrer formula is used in some simple cases where the crystals size is less than hundred angstroms and line broadening is due to this small crystal size.

Various physicists have shown that the broadening arising from microstrain, ε_L depending on the Bragg angle and the order of reflection. So the corresponding line breadth due to strain is

$$\beta = 4\varepsilon_L \ \tan\theta \tag{2.3}$$

From this Eq. (2.3) we can calculate the microstrain parameter, ε_L . Polycrystalline samples show noticeable variations in crystallite size with grains including dislocation networks, SFs, twin planes and other lattice faults. The interpretation of the peak broadening is difficult due to these distortions. In general, the Scherrer equation produces large values of coherently diffracting domains. However, the Scherrer equation established the first relation between microstructural properties of samples and their Bragg reflection profile. The use of some of the more advanced techniques briefly presented in the following sections.

2.2.1 Integral Breadth Method

Integral Breadth method is an oldest method to determine crystallite size and microstrain. Scherrer (1918) described the breadth of a diffraction line, as its angular width in radians at a point in time when the intensity has fallen by half of its maximum value. In 1926, von Laue defined a diffraction line's breadth (β), as the integrated intensity of the line profile above the background divided by the peak height.

$$\beta = \frac{1}{I_p}\int I(2\theta)\, d_{hkl}(2\theta) \tag{2.4}$$

In integral breadth method the separation of size and strain broadening of integral breadth depends on the shape of the broadening profile due to each effect., It is considered, the broadening is occurred due to lattice strain if the crystallite size $D \geq 10^{-4}$cm. If the broadening is due to crystallite size and lattice distortion both and shapes of their individual profiles are known, the separation of crystallite size and microstrain can be done. If size and strain broadening are present, total integral breadth of a Bragg peak is the summation of size and strain broadening

$$\beta = \beta_s + \beta_D \tag{2.5}$$

where, β_s is the size-broadening integral breadth, and β_D strain broadening integral breadth. As a result of the distinct dependences between both effects, Williamson and Hall

(1953) were able to segregate the effects of size and strain broadening in their analysis and the equation can be written as

$$\beta_{2\theta} = \frac{K_s \lambda}{\langle D \rangle_V \cos\theta} + 2K_D \varepsilon_L \tan\theta \qquad (2.6)$$

Where, K_s is the Scherrer constant. The integral breadth β can now be modeled numerically as a function of scattering angle 2θ and the course of $\beta(2\theta)$ can be fitted with the model function in Eq. (2.6) and thereby from the fit parameters, $\langle D \rangle$ and ε_L are obtained. Multiplying both sides of Eq. (2.6) by $\frac{\cos\theta}{\lambda}$ yields

$$\beta_{2\theta} \frac{\cos\theta}{\lambda} = \frac{K_s}{\langle D \rangle_V} + 2K_D \varepsilon_L \frac{2\sin\theta}{\lambda} \qquad (2.7)$$

This equation shows that the plot of $\frac{\beta \cos\theta}{\lambda}$ versus $\frac{2\sin\theta}{\lambda}$ should give a straight line and from the intercept of the line, the average crystallite size $\langle D \rangle$ can be determined and strain ε_L determined from slope. This graph is generally named the Williamson-Hall plot. The Williamson-Hall plot according to Eq. (2.7) should be taken with caution due to the various anisotropies that may be associated with the microstructure of the sample. There is a significant scatter of the data around an ideal Williamson-Hall line which comes from the anisotropy.

2.2.2 Fourier analysis: determination of coherent domain sizes and r.m.s. strains

In imperfect crystal the Fourier method of peak-shape analysis by Warren-Averbach (WA) technique is a very general and prevailing method of analyzing peak broadening due to size and strain. Fourier method play an important role in X-ray diffraction analysis. We can express the power distribution as a Fourier series (Warren, 1969):

$$P_i(\Delta K) = N \sum_{L=-\alpha}^{+\alpha} A(LK_i)\cos(2\pi L \Delta K) + B(LK_i)\sin(2\pi L \Delta K) \qquad (2.8)$$

where, N is (approximately) a constant, A and B are cosine and sine Fourier coefficients and L is the distance perpendicular to the diffracting planes. In practice, L takes specific discrete value $n\Delta L$, where n is an integer and ΔL is inversely proportional to the length of the measurement range in the reciprocal space. The line profile according to Eq. (2.8) is defined with respect to a distance K_i to the origin in reciprocal space, related to the diffraction angle $2\theta_i$, by $K_i = 2sin\theta_i/\lambda$, where λ is the wavelength. The deviation from K_i is denoted by ΔK, where. $\Delta K = 2(sin\theta - sin\theta_i)/\lambda$. Usually for $2\theta_i$ the location of the centroid of the line is chosen. Any pair of line profile P_1 and P_2 with $K_2 = 2K_1$ is called a first and second order reflection. As the sine coefficients are not physically interpreted (Mittemeijer & Delhez, 1978; Ungar *et al.*, 1989), only the cosine Fourier coefficients $A(LK_i)$ are considered.

2.2.3 The Warren-Averbach analysis

It is considered that the distribution of X-ray intensity measured from a structurally imperfect specimen is related to the structurally broadened line profile and an instrumental line profile. Fourier coefficients of the measured profile are also the combination of Fourier coefficient of the structural and instrumental line profiles. Using a 'standard' specimen free of lattice defects, the instrumental profile can be measured. According to Stokes, the Fourier coefficients of the structurally broadened line profile are obtained (Stokes, 1948) by convoluting Fourier coefficients of the line profiles of the imperfect specimen and the 'standard' specimen. It is possible to treat two broadened line profiles analogously if no standard specimen is available, by defining the profile with a smaller broadening as the instrumental profile. Thus, resultant Fourier coefficients reflect the differences in lattice imperfection (crystallite size and microstrain).

For a structurally broadened line profile the Fourier cosine coefficients can be written as the products of two coefficients, the two coefficients are order-independent size coefficients $A^s(L)$ and order-dependent strain coefficients $A^d(L, K_i)$ (superscript s for size and d for distortion). It is assumed that the specimen is consist of columns parallel to the diffraction vector. If D is the column length and $\rho(D)$ is the column length (size) distribution, $A^s(L)$ is determined by $\rho(D)$. The average column length (size) is represented by $\langle D \rangle$. Now if $\rho(\varepsilon_L)$ is the strain distribution, where ε_L is the average of the true (local) strain ε_0 over a length L, $A^d(L, K_i)$ is determined by $\rho(\varepsilon_L)$. Column length distribution and strain distribution are normalized to unit area. In summary (Warren, 1959):

$$A(L, K_i) = A^s(L)\, A^d(L, K_i), \qquad (2.9)$$

$$A^s(L) = \frac{1}{\langle D \rangle} \int_{|L|}^{\propto} (D - |L|)\, \rho(D) dD \qquad (2.10)$$

$$A^d(L, K_i) = \int_{\propto}^{\propto} \rho(\varepsilon_L)\, \cos\,(2\pi L K_i \varepsilon_L) d\varepsilon_L \qquad (2.11)$$

At least two orders of reflections have to be measured to know statistics of $A^s(L)$ and $A^d(L, K_i)$ separately. $A^s(L)$ and/or $A^d(L, K_i)$ has to be stated by making some assumption on

$\rho(D)$ and $\rho(\varepsilon_L)$. The latter can be accomplished in various ways, resulting in different separation methods. In practice, one must choose the separation method that best suits the specimen to be studied.

An approximation is used in the WA analysis for the K_i dependence of $A^d(L, K_i)$. By Taylor-series expansion for small L and K_i it can be expressed (Warren & Averbach, 1950; van Berkum *et al.*,1994).

$$ln\,\lfloor A^d(L, K_i)\rfloor \cong -2\pi^2 L^2 K_i^2 \langle \varepsilon_L \rangle \cong (K_i/K_1)^2 ln\,\lfloor A^d(L, K_1)\rfloor \qquad (2.12)$$

where, ε_L is the mean squared strain. Eq. (2.12) is exact for all values of L and K_i if all $\rho(\varepsilon_L)$. are Gaussian (Warren & Averbach, 1950). The more the $\rho(\varepsilon_L)$ deviate from being Gaussian, the smaller the range in L for which Eq. (2.12) is valid.

According to Warren (Warren & Averbach, 1952), from Eq. (2.12) and the order independence of. $A^s(L)$ the WA analysis can be written as:

$$ln\,[A(L, K_i)] = ln\,[A^s(L] - 2\pi^2 L^2 K_i^2 \langle \varepsilon_L^2 \rangle \qquad (2.13)$$

For the sake of comparison with the other separation method, the following form of the basic equation for the WA analysis is favored:

$$ln\,[A(L, K_i)] = ln\,[A^s(L] - (K_i/K_1)^2\, ln\,[A^d(L, K_i] \qquad (2.14)$$

From intercept of the plot of $ln\,[A(L, K_i)]$ versus $(K_i/K_1)^2$, the size Fourier coefficients are obtained and from the slopes the strain Fourier coefficients of the profile $\rho_1$are obtained. Mean squared strain $\langle \varepsilon_L^2 \rangle$ can be calculated from $A(L, K_i)$ using Eq. (2.12) if the application of the WA analysis is acceptable.

2.2.4 The modified Williamson-Hall and Warren-Averbach analyses

The scatter in the conventional Williamson-Hall plot is caused by strain anisotropy of elastic constants were addressed by Ungar and coworkers through the use of dislocation contrast factors ($\bar{C}_{hkl}$) for the different representative Bragg reflections (hkl) in the analysis scheme. This approach is commonly referred to as the modified Williason-Hall and WA analyses and is based on the assumption that microstrain arises from screw and edge dislocations of equally populated glide systems. The average contrast factors ($\bar{C}_{hkl}$) for different Bragg reflections

(hkl) were further used in the *modified* W-H plot (Ungar *et al.*, 1998a; Sahu *et al.*, 2012) and in the *modified* W-A procedure (Ungar *et al.*, 1998; Sahu *et al.*, 2012) to determine the dislocation densities (ρ), the effective outer cut-off radius (R_e) of dislocations and the dimensionless quantity, $M = R_e\sqrt{\rho}$. The parameter R_e indicates the range over which the distribution dislocation could be assumed as random, while M represents their dipole character, whose smaller or larger than unity value indicate a stronger or weaker dipole character, respectively (Wilkenns, 1970; Ungar *et al.*, 1998a). The full-width-at-half-maximum (FWHM) of the Bragg reflections were obtained using a pseudo-Voigt function fitting according to Enzo *et al.* (1988), could be substituted into the W-H equation as (Williason & Hall, 1953):

$$\Delta K = \frac{0.9}{D} + \Delta K^D \qquad (2.15)$$

where, $K = \frac{2sin\theta}{\lambda}$ is the magnitude of the diffraction vector, $\Delta K = \frac{2cos\theta}{\lambda}\Delta\theta$ is the FWHM, θ and λ represent the Bragg angle and wavelength of the X-rays used, respectively. D is the average crystallite size and ΔK^D is the strain contribution to X-ray peak broadening. Further invoking the concept of dislocation contrast factors, Ungar *et al.* (1998a) suggested that the *conventional* W-H equation be modified in terms of the scaling factor $K^2\bar{C}_{hkl}$ as:

$$\Delta K = \frac{0.9}{\mathrm{D}} + \left(\frac{\pi M^2 b^2}{2}\right)^{1/2} \rho^{1/2} K \bar{C}_{hkl}{}^{1/2} + O(K^2\bar{C}_{hkl}) \qquad (2.16)$$

wherein, ρ and b represent the dislocation density and the magnitude of the Burgers vector, respectively. O represents higher order terms in $K^2\bar{C}_{hkl}$. Higher order terms of quadratic Eq. (2.16) is neglected and after squaring Eq. (2.16), the following equation is obtained:

$$[(\Delta K^2) - \alpha]/K^2 \; = \; \beta \, \bar{C}_{hkl} \qquad (2.17)$$

where, $\alpha = (0.9/\mathrm{D})^2$ and $\beta = \frac{\pi M^2 b^2 \rho}{2}$. It is established for cubic crystals that the average contrast factors of dislocations, $\bar{C}_{hkl}$, corresponding to the Bragg reflections (hkl) is given by (Ungar *et al.*, 1999):

$$\bar{C}_{hkl} = \bar{C}_{h00}(1 - qH^2) \qquad (2.18)$$

where, $\bar{C}_{h00}$ is the average contrast factor for $h00$ type of Bragg reflection, derived from the elastic constants of the crystal, while q determines the screw or edge character of dislocations and H^2 is defined as:

$$H^2 = \frac{(h^2k^2+k^2l^2+l^2h^2)}{(h^2+k^2+l^2)^2} \tag{2.19}$$

Using Eq. (2.18) in Eq. (2.17), Eq. (2.16) for *modified* W-H plot further reduces to:

$$[(\Delta K^2) - \alpha]/K^2 = \beta \bar{C}_{h00}(1 - qH^2) \tag{2.20}$$

Hence, the coefficient of H^2 in Eq. (2.20) gives the value of the parameter q. For austenite Ungar *et al.* (1999) reported that the values of q for pure edge and screw dislocations are 1.71 and 2.46, respectively. From Eq. (2.20) the q values of austenite are obtained. The q values are used to estimate the fractions of edge and screw dislocations in this microstructure according to following equation (Garabagh *et al.*, 2008):

$$f_{\gamma(edge)} = \frac{(2.46-q_\gamma)}{(2.46-1.71)} \tag{2.21}$$

$$f_{\gamma(screw)} = 1 - f_{\gamma(edge)} \tag{2.22}$$

where, $f_{\gamma(edge)}$ and $f_{\gamma(screw)}$ signify the fraction of the edge and screw dislocations within the austenite microstructure, respectively.

The concept of average contrast factor is then utilized for the real part of the Fourier coefficients, $A(L)$ in the *modified* W-A equation as (Ungar *et al.*, 1998a):

$$\ln A(L) \cong \ln A^s(L) - \rho\frac{\pi b^2}{2}L^2 \ln\left(\frac{R_e}{L}\right)(K^2\bar{C}_{hkl}) + Q(K^4\bar{C}^2{}_{hkl}) \tag{2.23}$$

where, $A^s(L)$ are the size Fourier coefficients of the peak profile, L is the Fourier variable. Neglecting the higher order terms of $K^2\bar{C}_{hkl}$ in Eq. (2.23), $\ln A(L)$ becomes a function of $K^2\bar{C}_{hkl}$. Thus, the real part of the Fourier coefficients derived from the fitting of the individual diffraction profiles may be plotted for various L values, whose slope (Y) in the linear region can be approximated as $\rho\frac{\pi b^2}{2}L^2 \ln\left(\frac{R_e}{L}\right)$ and further rearrangement of the slope in Eq. (2.23) leads to:

$$\frac{Y(L)}{L^2} = \rho\frac{\pi b^2}{2}\ln(R_e) - \rho\frac{\pi b^2}{2}\ln(L) \tag{2.24}$$

Eq. (2.24) is thus identical to $y = mx + c$, yielding a linear relationship between $\frac{Y(L)}{L^2}$ and $\ln(L)$, wherein, the dislocation density (ρ) and the effective outer cut-off radius (R_e) of dislocations are directly determined from the slope and intercept of Eq. (2.24), respectively.

2.2.5 The consideration of stacking and twin faults

To study the effects of SFs in the microstructure of a deformed material, X-ray diffraction is a powerful device. Barrett (1952) first suggested that SFs could be formed in the close-packed fcc metals as a result of cold work, which is the cause of certain changes in the observed XRD pattern. Paterson (1952) presented that for fcc metals, peak shift and twin or growth faults produce asymmetry broadening and deformation faults produce symmetric broadening. For handling SF problem, the difference equations method, which leads to the expression for the probability of mth neighbour layer is the same or different from the original layer, was formerly used by Wilson (1942) and then by Paterson (1952). Gevers (1954a) gives the difference equation for combined effect of growth and deformation faults. Warren assumed that for fcc structure the probabilities for both faults are sufficiently small and gives a simplified form of Gevers (1954b) technique. The peak position shift, peak asymmetry and peak broadening effects contribute to the two fault probabilities namely, SFs $\left(P_{sf}\right)$ and twin fault (P_{tw}).

The shift in peak position of a cold worked material from its annealed specimen is mainly due to combined effect of SFs, change in lattice parameter $(\Delta a/a_0)$and long range residue stress. Considering faulting as the predominant factor for peak shift the stacking fault probability (P_{sf}) is obtained from peak shift analysis of the relative peak shifts of neighboring pairs of profiles taking the corresponding annealed samples as standard. The equation used can be written as

$$\delta(\Delta 2\theta)_{hkl}^{h'k'l'} = A_{hkl}^{h'k'l'}((\Delta a/a_0) \qquad (2.25)$$

Where,

$$\delta(\Delta 2\theta)_{hkl}^{h'k'l'} = \Delta(2\theta)_{hkl} - \Delta(2\theta)_{h'k'l} = (2\theta_{hkl} - 2\theta_{h'k'l})_{cw} - (2\theta_{hkl} - 2\theta_{h'k'l})_{ann} \qquad (2.26)$$

is the comparative peak shifts of the neighbouring pairs of reflections hkl and $h'k'l'$ from cold worked and annealed profiles.

In the absence of an annealed specimen of the same composition free from SFs, another novel approach for determining the values of P_{sf} exists, which has been adopted by several researchers to calculate P_{sf} in different austenitic steels (Tolonen & hanninen, 2007; Huang *et* *al.*, 2008). In this approach, Bragg's law is combined with the Warren's treatment (Warren, 1969) to determine the angular position of the faulted austenite diffraction lines as:

$$2\theta_{hkl} = 2arcsin\left(\frac{\lambda}{2d_{hkl}}\right) + \frac{90\sqrt{3}\,P_{sf}tan\theta_{hkl}}{\pi^2 h_0^2(u+b)}\sum(\pm)\,L_0 \tag{2.27}$$

where, θ_{hkl} is the angular position of austenite (hkl) reflection, $\frac{1}{\pi^2 h_0^2(u+b)}\sum(\pm)\,L_0$ is a constant specific to each austenite (hkl) reflection, the values of which are available in the literature (Warren, 1969). d_{hkl} is the faulted interplanar spacing of the austenite (hkl) planes, can be further written in terms of faulted austenite lattice parameter (a) as: $d_{hkl} = \frac{a}{\sqrt{h^2+k^2+l^2}}$. and λ is wavelength of X-ray used. Subsequently, the set of linear equations for each Bragg reflection, represented by Eq. (2.27) can be solved to estimate the P_{sf}. The effect of long-range residual stress on the direction dependent diffraction line shifts was insignificant and its contribution was assumed to be zero in Eq. (2.27).

2.3 Transmission electron microscopy

TEM is the most commonly used technique for the microstructural characterization of materials. It is widely used for imaging crystal defects in crystals namely, dislocations, SFs, twin, grain boundaries and voids. It is a direct observation method, helps to study the defects, as well as their nature, configuration, etc. For all crystal defects the imaging principle and underlying contrast formation mechanism are the same, which basically exploits the effect of their strain fields on electron scattering. Different modes of imaging of dislocations in TEM is presented briefly in the next sections.

2.3.1 Contrast in transmission electron microscope

Based on contrast mechanism working for their image formation, TEM offers two modes of imaging. These two contrast formation mechanisms are phase contrast and diffraction contrast. High resolution TEM (HRTEM) image is formed according to phase contrast mechanism in which columns of atoms parallel to electron beam are imaged end-on. Missing planes and the core structure of dislocations are imaged with HRTEM. It can identify planes placed as close as 0.2 nm apart (Li, 2009). HRTEM is, however, applicable to a limited number of problems, because it requires dislocation line to be straight and parallel to the electron beam and its core remains same over its entire length (Li, 2009; William & Carter, 2009). Therefore, imaging of dislocations with HRTEM is mostly restricted to dislocations with planar core structures as in the case of covalent crystals and usage of HRTEM in the studies of metallic materials is very minimal.

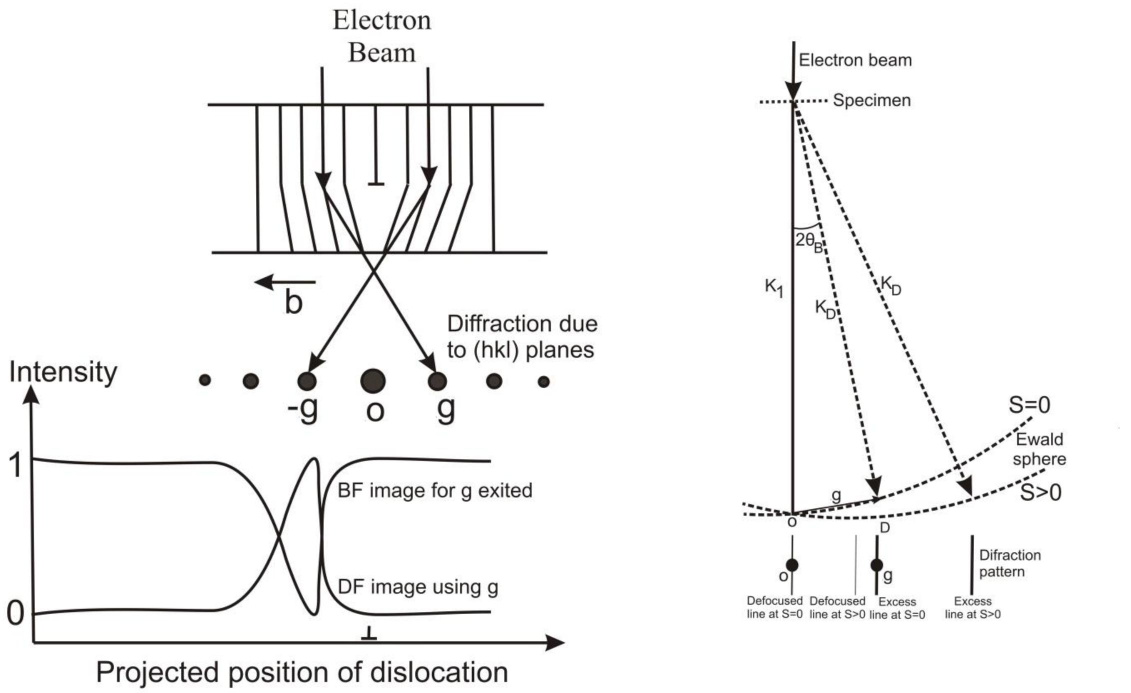

Fig. 2.2: Schematic depicting distorted planes close to the dislocation core diffracting into $\vec{g}$ and $-\vec{g}$. This condition is achieved when the specimen, in general, is tilted slightly away from the Bragg condition $s = 0$ to bring distorted planes near the core into exact Bragg condition $s = 0$. Lower diagram depicts intensity profiles of the dislocation contrast displaced away from its projected position when imaged with $-\vec{g}$ reflection. (b) Ewald sphere geometry for two beam diffraction condition with $s = 0$ and $s < 0$. Lines shown are Kikuchi lines which arise from inelastically scattered electrons (William & Carter, 2009). A pair of Kikuchi lines comprises an "excess" and a "deficient" line. These lines help in setting up the Bragg's condition. When $s > 0$ Kikuchi lines are on the same of side of as $\vec{g}$ as O; when $s > 0$ the lines are on the opposite side of $\vec{g}$.

Diffraction contrast imaging of dislocations exploits the effect of strain fields in Bragg diffraction condition. The presence of a dislocation in a lattice causes atomic planes to bend, particularly at regions close to the core. For imaging, the specimen has to be first tilted into a two-beam condition, exciting a strong diffraction vector $\vec{g}$ from only a specific set of hkl planes, other than the direct (transmitted) beam. It is then tilted slightly away from the exact Bragg condition (i.e. with some excitation error or deviation, $s > 0$) so that distorted planes near the core of dislocation are brought into the Bragg condition while regions distant from the dislocation core are tilted away, as shown in Fig. 2.2. Some scattered intensity from regions not at the exact Bragg condition may still be visible due to streaking or broadening of Bragg peak due to size effect. The contrast of dislocation image is determined by $\vec{g}.\vec{R}$ where $\vec{R}$ is the lattice distortion vector. For a pure screw dislocation, $\vec{R}$ is directly proportional to b Thus, an analysis of the $\vec{g}.\vec{b}$ condition can be correlated to the observed contrast condition of dislocations. Screw dislocations with $\vec{g}.\vec{b} = 0$ do not produce any strain contrast, as the diffracting planes are parallel to $\vec{R}$. This is known as the “invisibility” criterion for dislocations. For edge dislocations the condition, $\vec{g}.\vec{b} \times \vec{u} = 0$ ($\vec{u}$ is the line direction) also has to be satisfied as the displacement field of an edge dislocation causes buckling of the glide planes. Images formed by diffraction contrast are asymmetric. The location of the diffracted intensity relative to the core depends on the signs of and deviation $\vec{g}, \vec{b}$ parameter s. If any sign is reversed, the contrast shifts across the core.

The two modes of imaging dislocations are namely the bright field (BF) and the dark field (DF) depending upon whether the transmitted beam or the diffracted beam is chosen for constructing the image. In the BF mode, dislocations appear in dark contrast on a bright back ground, while they appear in bright contrast on a dark background in the DF mode. The dislocation contrast appears only due to the operating diffraction vector and the area that appears dark/bright in the BF/DF images are areas where the hkl planes are at the Bragg condition. The nature of dislocations (i.e. edge, screw, or mixed nature) can be identified by TEM analysis, along with the glide plane. Diffraction contrast imaging can also disclose features such as, jogs or kinks, and the interactions of dislocations with other dislocations or lattice defects. Diffraction contrast imaging has revealed the existence of unusual defects like SF tetrahedron, faulted dipoles, and multipoles (William & Carter, 2009).

Mainly in elastically anisotropy materials diffraction contrast of dislocations can be blocked out by the dynamical scattering of the intense diffracted beam. Due to this the analysis of closely separated dislocations gets limited, as in the case of super dislocations of intermetallics. Here the computer simulation of dislocation contrast is required to interpret the experimentally observed diffraction contrast. Further, the Burgers vectors associated with perfect translations in ordered phases are generally integral multiples of Burgers vectors of lattice dislocations in the corresponding disordered phases. The invisibility criterion, $\vec{g}.\vec{b}$ satisfied by dislocations with a Burgers vector $\vec{b}$ would as well be satisfied by dislocations with

Burgers vectors given by an integral multiple of $\vec{b}$. Therefore, the magnitude of the Burgers vector of dislocations in ordered phases cannot be explicitly determined with the use of invisibility criterion alone. In these scenarios too, the computer simulation of dislocation images (Singh *et al*., 1988) can help to determine the magnitude of Burgers vector.

Diffraction contrast imaging is particularly useful in the in-situ deformation studies, where, to evaluate the development of dislocation structures a special cognizance of dislocation reactions required. Miniaturised tensile samples (less than 3mm in gauge length) are strained in the microscope and dislocation movements, dislocation-dislocation interaction, its interactions with other defects and the multiplication processes occurring during the plastic deformation are observed and recorded in real time. In-situ experiments are a powerful method of studying micro-processes that control dislocation mobility. The direct measurement of parameters such as, density of mobile dislocations, kinetics of movements or events, measurement of activation volume can be done by in-situ experiments It is possible by this technique to observe metastable core configurations that exist only under stress. Finally, this is the only technique in which the direct observation can be made of processes like dislocations overcoming obstacles such as, precipitates, interfaces, etc.

2.3.2 Weak Beam Transmission Electron Microscopy

Weak beam (WB) Transmission Electron Microscopy is a special case of diffraction contrast imaging in which weakly excited reflections are used for imaging. It is called WB because the intensity of the diffraction spot working for imaging is very weak when averaged over the imaging area. By locating the crystal orientation far away from the Bragg condition (*i.e.* $s > 0$) in the two beam condition, the WB condition is obtained. The diffraction condition in which the specimen is tilted to a 3g WB condition is shown schematically in Fig. 2.3.

In this condition using the $\vec{g}$ vector in DF imaging dislocations are imaged as bright and sharp lines with negligible intensity everywhere else. Firstly, the regular two-beam condition is set up for WB imaging and then the specimen is tilted to a large value of deviation, s.The average intensity decreases at a rate of $\frac{1}{s^2}$ as s increases and the diffraction beam looks as a weak spot (William & Carter, 2009). Due to large s, the excitation distance will be small and, thus, sharp and narrow images of dislocations are formed. Unlike conventional DF imaging, the positions of dislocations imaged under WB are well defined with respect to their cores. In the WB condition the resolution is limited by the minimum volume of crystal (set locally in

Bragg orientation) that causes constructive interference (William & Carter, 2009). Dislocation pairs as close as ~1.5 nm can be resolved by using WB imaging (Veyssier, 1991).

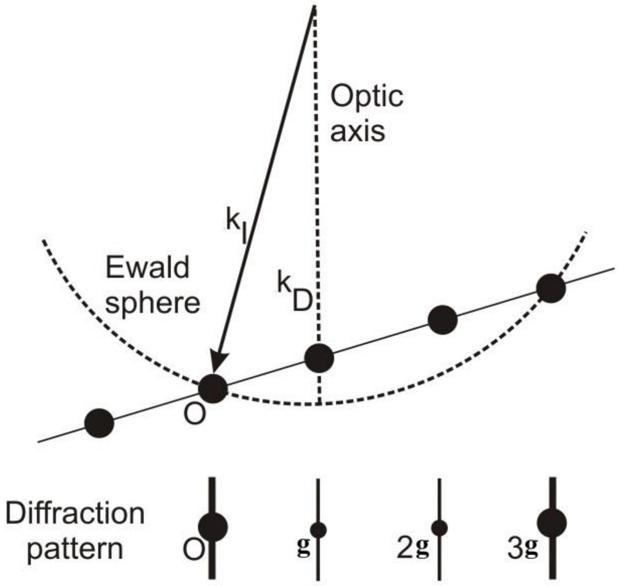

Fig. 2.3: Ewald sphere and positions of Kikuchi lines for the diffraction conditions. (William & Carter, 2009).

In intermetallic alloys the WB technique is mostly useful for reviewing finely separated dislocations, where distances between dislocation pairs are very small (of the order of nm). There are some advantages of WB imaging, its low sensitivity to foil thickness and position of dislocations in the sample, and, as compared to DF imaging there is the lower uncertainties in elastically anisotropic crystals, which is affected by dynamical scattering. As fine structures of dislocations can be resolved by using WB imaging, this characterization of dislocations has become popular.

As a typical TEM sample only characterizes a maximum volume of about 10^{-5} mm^3, questions arise about the reliability of TEM analysis in predicting deformation mechanisms when bulk material is taken. According to Veyssier (1991) a rough estimation of the defect density in TEM samples can be made. Assuming that the density of dislocations is of the order of 10^9 cm^{-2} in a sample deformed to a permanent strain of 1%, this implies that to describe the entire deformation process only about a few centimetres of dislocation length can be examined and out of which, a small fraction of dislocations are analyzed (*i.e.*, slip plane, Burgers vector dislocation reaction, etc.) to characterize the entire deformation process.

TEM delivers the most wide-ranging and detailed analysis of the deformation behavior and the nature of dislocations. It is the only tool that can disclose uncommon slip systems and deformation processes that often occur in many alloy systems. Its imaging capabilities are better than other techniques, while the others may only compliment it by sampling larger volumes of the specimen**.**

2.4 Electron Backscatter Diffraction

Electron Backscatter Diffraction (EBSD) is an analysis technique based on scanning electron microscope (SEM) used to obtain crystallographic orientation with sub-micron spatial resolution and also to get phase information of the material. The EBSD's image is based on the Kikuchi diffraction patterns obtained in a TEM (Nishikawa & Kikuchi, 1928a, 1928b; Joy & Booker, 1971; Venables & Harland, 1973; Dingley, 1984) and the introduction of the Hough transform for interpretation of the obtained images (Schmidt *et al*., 1991; Lassen *et al*., 1992; Lassen, 1996). In EBSD accelerated electrons in the primary beam of a SEM can be diffracted by atomic layers in crystalline materials. These diffracted electrons can be detected when they impinge on a phosphor screen and generate visible lines, called Kikuchi bands, or "EBSP's" (electron backscatter patterns). These patterns are effectively projections of the geometry of the lattice planes in the crystal, and they give direct information about the crystalline structure and crystallographic orientation of the grain from which they originate. When used in conjunction with a data base that includes crystallographic structure information for phases of interest and with software for processing the EPSP's and indexing the lines, the data can be used to identify phases based on crystal structure and also to perform fabric analyses on polycrystalline aggregates.

In the EBSD experiment, a highly flat crystalline specimen with well-polished surface is placed in the SEM chamber. To increase the contrast in the resultant EBSD pattern the electron beam should hit the sample at a grazing angle nearly 20 degrees, i.e, the sample-carrying stage is inclined at 70 degrees (Fig. 2.4) Diffraction occurs on the specimen at the point of incidence of the electron beam which undergoes an acceleration voltage of 10-30 kV using and incident current of 1-50 nA. The EBSD pattern emerges spherically from the point of incidence with a stationary beam. This primary beam interacts with the crystal lattice, as a result of it the electrons which were backscattered with little loss of energy are channelled and made to cross different paths. This results constructive and destructive interference.

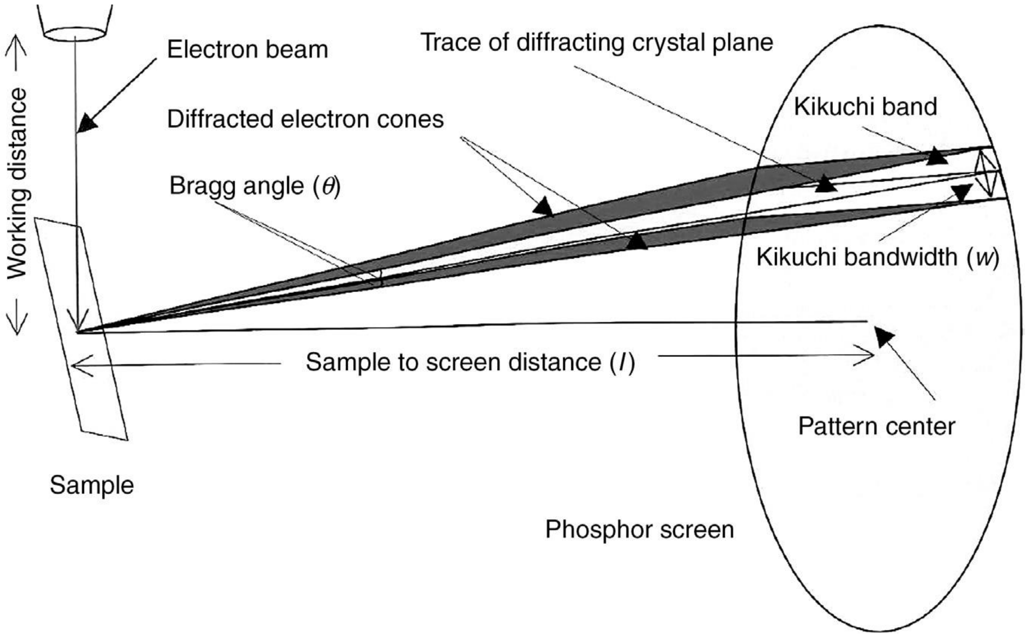

Fig. 2.4: Detection setup for Electron backscatter diffraction (EBSD). (Pereira-da-Silva & Ferri,2017).

The detector is actually a charge-coupled device (CCD)–type camera equipped with a phosphor screen integrated with a digital frame grabber. The camera resides on a horizontally mounted motorized carriage. It is inserted to within several mm of the surface of the inclined sample. The optimal arrangement results when the camera is as close to the sample as possible. A diffraction pattern is observed in the path of the diffracted electrons if we place the phosphorous screen very close to the sample. (Wells, 1999). The phosphorous screen converts the diffracted electrons into photon thus transforming the backscattered signal into light. This light enters the CCD camera and the EBSD image is detected by it. Now the EBSD image detected by the CCD camera can be recorded and analyzed. The EBSD images depends on the crystal's spatial orientation in the sample, sample's distance from the phosphorous screen and on the incident electron beam's wavelength.

The pattern of Kikuchi lines on the phosphor screen is electronically digitized and processed to recognize the individual Kikuchi lines. Kikuchi lines are best seen in diffraction patterns from areas of the specimen that have a low density of defects and are about half of that the beam can penetrate or thicker. If the specimen is thinner only spots will be seen, if it is very thick only Kikuchi lines will be seen. The location of the more intense Kikuchi bands (Fig. 2.5) can be clearly identified within the Hough space by the brightest peaks but other peaks are more indistinct and almost unnoticeable. Now by the peak detection algorithm the most intense peaks are analyzed (Fig. 2.5) and the ultrafine false peaks are disregarded. To analyze the results, a line corresponding to each peak of the previous image is superimposed on the original image of the Kikuchi diffraction pattern.

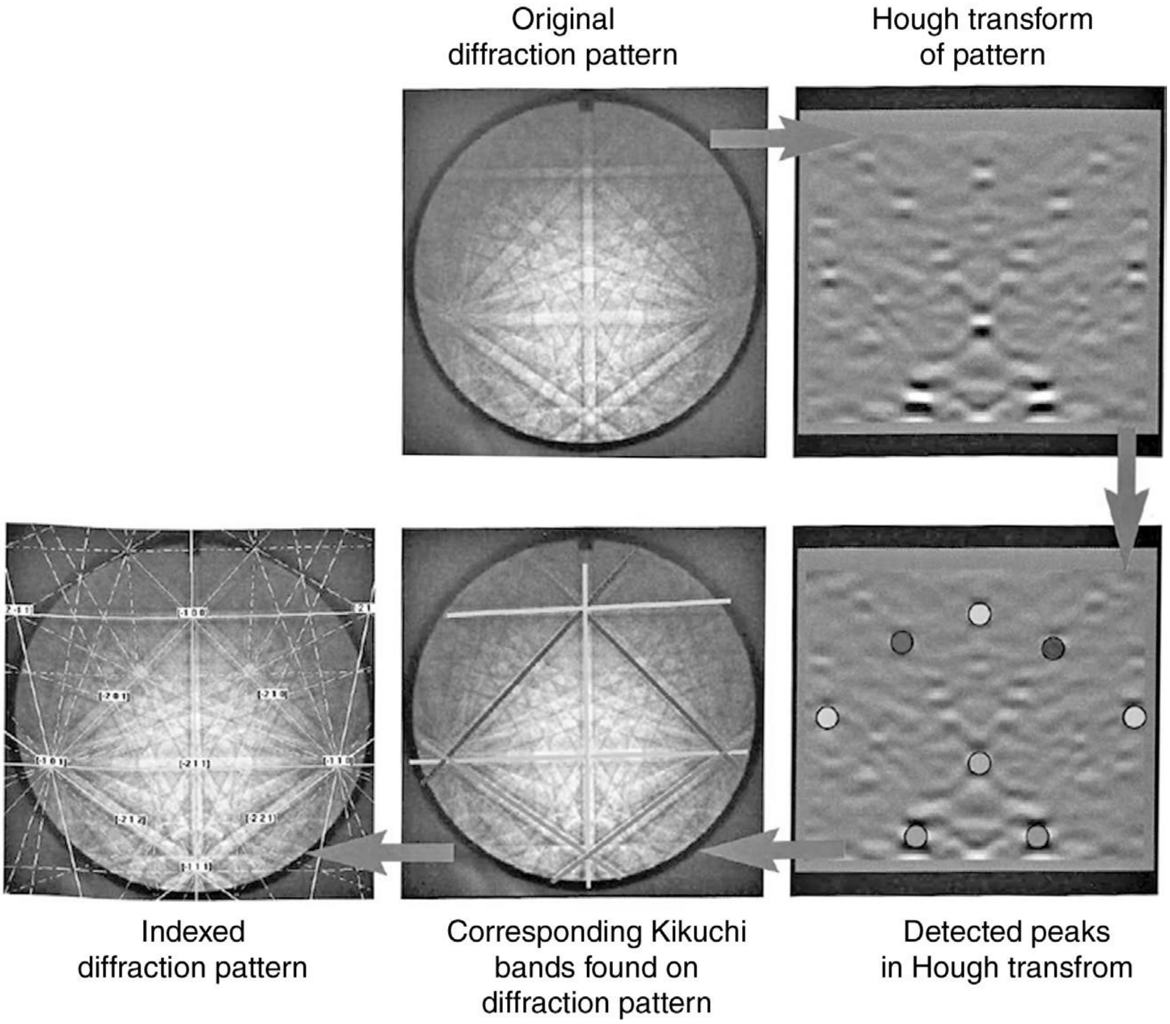

Fig. 2.5: EBSD sequence for obtaining structural characteristics. This sequence includes the original diffraction pattern, Hough transformed pattern, peaks detected in the Hough transformation, corresponding Kikuchi bands found in the diffraction pattern, and indexed diffraction patterns. (Pereira-da-Silva & Ferri,2017).

The lines and peaks are coded illustrating their relationship for each point or set of points. Now it is possible to make a map of the structural characteristics of the entire image, identifying points with the same structural features, when we get the structural characteristics of a set of points within an image. EBSD data used for lot of purposes like, to determine the orientation of the crystal, to identify the phase and to index the pattern. Also it can be used to make statistical studies of the micro fabric of the sample, to know the systematic textural relations between individual grains or phases, and to determine relative abundances of phases in a poly phase sample. It is possible to obtain data for phases of all symmetries (even isotropic phases) and for opaque phases in EBSD. This data gives a true 3-dimensional orientations of the individual crystals and the spatial resolution can be few microns.

2.5 Electron channelling contrast imaging

Electron channelling contrast imaging (ECCI) is a scanning electron microscope (SEM) technique. Crystal defects like dislocations can be imaged by ECCI in SEM. According to the dynamical theory of electron diffraction, by orienting the crystal specimen into Bragg condition the optimum diffraction contrast for crystal defect imaging can be obtained, for a selected set of intense lattice planes.

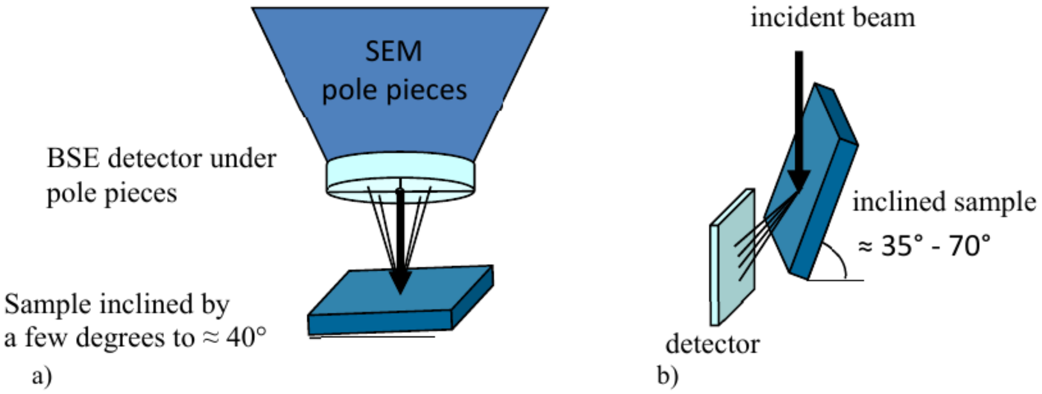

Fig. 2.6: Illustrating the a) backscatter, and b) forescatter geometries for acquisition of ECCI micrographs (Trager *et al*., 2020).

When a sample is placed so that a plane or planes are at the Bragg angle with respect to the incident electron beam then ECCI Micrographs are produced. Deviation in crystallographic orientation or in lattice constant happens due to local strain. As a result of this a variation in contrast is produced in ECCI micrograph. Now when the electron beam is scanned over the sample then by monitoring the intensity of backscattered or forescattered electrons the micrograph is constructed. Very small changes in strain and orientation can be detected, which reveals low angle tilt and rotation boundaries and atomic steps. Extended defects like dislocations and SFs can be imaged in ECCI (Wilkinson & Hirsch, 1997; Crimp *et al*., 2001; Trager *et al*., 2007; Picard *et al*., 2012). An electron beam with a low divergence (a few mrad), small spot size (nanometres) and high brightness (nanoamps or higher) is required to resolve individual dislocations in an electron channeling contrast image (Wilkinson &

Hirsch, 1997; Joy *et al.*, 1982). All these conditions are perfectly fulfilled in a field emission gun SEM. We can get the ECCI micrographs at lower electron beam energies (Naresh *et al.*, 2019; Han *et al.*, 2020). Though ECCI is very helpful to quantify surface defects but it cannot qualify the dislocations below the surface easily because ECCI technique is not efficient in determining exact sampling depth perfectly and also it has low surface sensitivity. Quantitative data on dislocations which lie below the surface could be obtained by changing the energy of the electron beam.

In Fig. 2.6 backscatter and forescatter geometries are illustrated. These two geometries are used to obtain ECCI micrographs. The backscatter geometry (Fig. 2.6(a)) allows the easiest imaging of large samples also as this geometry does not require a high tilt of the sample so a large correction of the image to account for tilt is not necessary. In this geometry the sample stays at approximately 90 degrees to the incident electron beam with the backscatter electron (BSE) detected by an electron-sensitive diode or diodes placed on the pole piece of the microscope. Compared to backscatter geometry, the forescatter geometry (Fig. 2.6(b)) has the upper hand that due to the increase in intensity of backscattered electrons here images show better signal-to-noise. In this geometry the sample is tilted to between 30° and 70° to the impinging electron beam and the forescatterd electrons detected by an electron- sensitive diode placed in front of the sample. To get quality ECCI micrographs a good amplifier with a large DC offset and high small signal gain should be used.

2.6 Estimation of experimental stacking fault energy

By adopting the X-ray analyses using Schramm & Reed method (1975) later modified by Dey *et al.* (2005), the SFE can experimentally be determined which considers the effect on dislocation parameters on SFE. This method can yield SFE values with higher statistics, but is based on several overgeneralized assumptions and often criticised due to indirect nature of estimation. On the other hand, there are two approaches under WBDF using TEM. According to Ruff (1970) SFE can be estimated through measuring the radii of isolated extended nodes. The other method of SFE estimation is through calculating the extension widths of $\frac{a}{2}\langle 111\rangle$ glide dislocations (Brown & Thölen, 1964; Ray & Cockayne, 1971). Though TEM approach is direct in nature but suffers from the shortcoming that it offers extremely low statistics, besides being strictly restricted to early deformation stages. Thus, considering the practical challenge to measure SFE experimentally, it is kept in mind that both the TEM and X-ray methods have their own merits and demerits and should be used concurrently for reliability of the results. The underlying principles of each methods are outlined below.

2.6.1 X-ray diffraction approach

Estimation of SFE using X-ray analysis according to the popular Schramm and Reed (1975) method is accomplished by utilizing the mean square microstrain $\langle \varepsilon_L^2 \rangle$ of the deformed austenite along $\langle 111 \rangle$direction, averaged over the distance of Fourier variable (coherence length), L =*50* Å and P_{sf} values. According to Dey *et al.* (2005) this is an oversimplified approach, which does not consider the effects of austenite dislocation density and arrangements on the microstrain distribution within the microstructure. In low SFE materials, microstrain broadening depend on hkl. According to Wilkens (1970) this dependency is due to the strain field anisotropy induced by the contrast factor of dislocations. Hence proper correction terms including dislocation contrast factor, arrangement and density should be combined in X-ray analyses for determination of SFE (Dey *et al.*, 2005).

From the above justification, it is evident that estimating the dislocation parameters are prerequisites for determination of SFE. It is established that in the presence of dislocation-induced strain broadening, the variation of strain field within the dislocation core can be described by the Wilkens strain function, given as (Wilkens, 1970):

$$\langle \varepsilon_L^2 \rangle = \rho \bar{C}_{hkl} \pi \left(\frac{b}{2\pi} \right)^2 \ln \left(\frac{R_e}{L} \right) \qquad (2.28)$$

where, $\vec{b}$ is the magnitude of Burgers vector of $\frac{a}{2}\langle 110 \rangle$ perfect dislocations determined from the Rietveld analysis, $\bar{C}_{hkl}$ is the average contrast factors for the different Bragg reflections (hkl), ρ is the dislocation density and R_e is the effective outer cut-off radius of the dislocations, signifying the range over which the distribution of dislocations is random. These parameters are directly determined from the graphical plots of modified Williamson-Hall equation and modified WA procedure, as described by Eq. (2.24). The modified Schramm and Reed method utilizes the relationship between the SFE of the steel (γ), stacking fault probability (P_{sf}), dislocation density (ρ) and lattice parameter (a) that was derived by Smallman and Westmacott (1957)

$$\gamma = \frac{K_{111} \omega_0 G a A^{-0.37}}{\sqrt{3} \pi P_{sf}} \left\{ \left(\frac{b}{2\pi} \right)^2 (\rho \bar{C}_{111} \pi)\, ln \left(\frac{R_e}{L} \right) \right\} \qquad (2.29)$$

where, $G \approx 72$ GPa is the shear modulus of the steel considered throughout and $A \approx 3.43$ is an anisotropy factor related to the X-ray elastic constants and determined according to Pierce *et al.* (2014) and $K_{111}\omega_0$ is a proportionality constant with a value of 6.6 (Martin *et al.*, 2016) and and $\bar{C}_{111}$ is the average contrast factor of dislocations for the austenite (111) Bragg reflection. It is noteworthy that the SFE of a deformed specimen estimated according to Eq. (2.29) essentially yields the effective SFE, but not the ideal SFE. In the presence of other defects, the ideal and the effective SFEs of a real crystal are related as (Müllner & Ferreira, 1996):

$$\gamma_{eff} = \gamma_{\infty} + \frac{\partial E_{str}}{\partial A} \qquad (2.30)$$

Where, γ_{eff} and γ_{∞} are the effective and ideal SFEs, respectively and $\frac{\partial E_{str}}{\partial A}$ is the increase in elastic coherency strain energy of the SF per unit area. However, this treatment assumes the coherency strain energy is conserved in volume, unlike the treatment of Olson & Cohen (1976), which assumes that elastic coherency strain energy comprises of two components as:

$$E_{str} = E_{dil} + E_{sh} \qquad (2.31)$$

where, E_{str} is the dilatation energy due to volumetric strain associated with volume change during $\gamma_{eff} \rightarrow \varepsilon_{hcp}$ martensitic transformation and E_{sh} is the shear energy involving the shear strain components. The studied deformation conditions considered in the present dissertation do not reveal any significant $\gamma_{eff} \rightarrow \varepsilon_{hcp}$ transformation and hence the treatment of Olson & Cohen (1976) is not tenable here and the Mullner & Ferreira (1996) approach was adapted to interpret the experimentally estimated SFE of austenite.

2.6.2 Transmission electron microscopy approach

Brown & Tholen (1964) proposed a method of estimation of SFE from the extended node by considering an idea of symmetric nature of extended node according to isotropic elasticity. This approach also tells us that the self-stress of a dislocation can be calculated by calculating the line integrals over the dislocation at the dislocation core. An iterative method helps to calculate the extended nodes by the way that dislocation core points are displaced successively until resultant stress acted upon them (self-stress plus stress due to SF and other partials) totally vanishes. As it is found in an isotropic medium that the self-stress due to curved screw dislocations can be much greater than the self-stress due to curved edge dislocations so, a difference always appears between nodes formation of screw and edge dislocations. According to nature of partials of edge or screw-type dislocation the relationship of SFE with the radius of curvature of the partials in the node is controlled. If we assume that the width of the node does not explicitly depend on the character of the dislocations rather curvature of the partials then SFE can be measured approximately by only measuring the width of the node through the following equations proposed by them within acceptable accuracy.

$$\frac{\gamma_{eff} \times R_1}{G b_p^2} = 0.27 - 0.08\left(\frac{\nu}{1-\nu}\right) cos2\alpha'' + \left\{0.104\left(\frac{2-\nu}{1-\nu}\right) + 0.24\left(\frac{\nu}{1-\nu}\right) cos2\alpha''\right\} log_{10}\frac{R_1}{e} \qquad (2.32)$$

$$\frac{\gamma_{eff} \times R_2}{G b_p^2} = 0.055\left(\frac{2-\nu}{1-\nu}\right) - 0.06\left(\frac{\nu}{1-\nu^2}\right) cos2\alpha'' + \left\{0.018\left(\frac{2-\nu}{1-\nu}\right) + 0.036\left(\frac{\nu}{1-\nu}\right) cos2\alpha''\right\} log_{10}\frac{R_2}{e} \qquad (2.33)$$

Where, G refers to the shear modulus, ν is the Poisson's ratio, $\vec{b}_p$ considered as Burger's vector of the partial dislocation, e refers to the vector normal to the dislocation line and related to Burger's vector, $R_1$and R_2 are defined in Fig.2.7, α'' refers to the character of the partials at points L, M and N in Fig. 2.7.

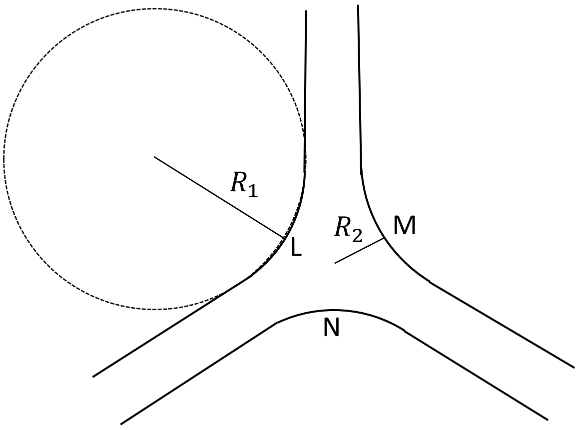

Fig. 2.7: An extended three-fold node and the parameters used to determine SFE according to Eqs. (2.32) and (2.33).

In the extension width method, it is considered that an equilibrium configuration is created when repulsive elastic force acted between the two partials is balanced by the attractive force due to increase of area of the SF. In equilibrium condition, if we take experimental separation values and fit with the theoretical curves predicted by Hirth & Lothe in 1982 through approximation of anisotropic dislocation theory then SFE can be determined by the following equation:

$$\gamma = \frac{G b_p^2}{8\pi x_{eq}(1-\nu)}(2 - \nu - 2\nu \cos 2\alpha'') \qquad (2.34)$$

where, $\vec{b}_p$considered as the Burgers vector of the Shockley partial dislocations (SPD), calculated from the austenite lattice parameters, x_{eq} refers to separation distance of the partial dislocation pairs at equilibrium configuration, ν is the Poisson's ratio of the studied steel and α'' is the angle between the perfect dislocation line and Burgers vector. Teutonico (1967) suggested that both anisotropic as well as isotropic theory agrees well for the extension width of the dislocations when partial $\frac{a}{2}\langle 110\rangle$ dislocations gliding on $\{111\}$ planes in case of fcc material. This made it possible to approximate the isotropic theory of elasticity in the present discussion. In visible condition of both partial dislocations under weak $\langle 220\rangle$ reflection it is possible to measure the angle made by the Burgers vector of the perfect dislocation with dislocation line on $\mathrm{g} - 3\mathrm{g}$ WBDF micrographs (Kim *et al.*, 2011). Several measurements are yet to be done along the length of straight parallel sections at equilibrium configuration of isolated dislocations, avoiding the areas which is affected by constrictions.

References

Barman, H., Hamada, A.S., Sahu, T., Mahato, B., Talonen, J., Shee, S.K., Sahu, P., Porter, D.A. & Karjalainen, L.P. (2014). *Metall. Mater.Trans. A.* **45**, 1937-1952.

Barret, C. S. (1952). *Imperfections in nearly perfect crystal*, Chap. III, John. Wiley, New York.

Brown, L. M. & Thölen, A. R. (1964). *Disc. Faraday Soc.* **38**, 35-41.

Bryne, J.G. (1965). *Recovery Recrystallization and Grain Growth*, McMillan CO, NY.

Crimp, M. A; Simkin, B. A. & Ng, B. C. (2001) *Philos. Mag. Lett.* **81**, 833-837.

Dey, S. N., Chatterjee, P. & Sen Gupta, S. P. (2005). *Acta. Mater*. **53**, 4635-4642.

Dingley, D. J. (1984) *Scanning Electron Microscopy* **2**, 569-575.

Enzo, S., Fagherazzi, G. Benedetti, A. & Polizzi, S. (1988) *J. Appl. Crystallogr*. **21**, 536-542.

Garabagh, M. R. M., Nedjad, S.H., Shirazi, H., Mobarekeh, M.I. & Ahmadabadi M.N. (2008). *Thin Solid Films.* **516**, 8117-8124.

Gevers, R. (1954a). *Acta Cryst.* **1**, 337-343.

Gevers, R. (1954b). *Acta Cryst.* **1**, 740-744.

Greenough, G. B. (1952). *Prog. Metal. Phys.* **3**, 176-219.

Han, H; Hantschel, T; Strakos, L; Vystavel, T; Baryshnikova, M; Mols, Y; Kunert, B; Langer, R; Vandervorst, W. & Caymax, M. (2020) *Ultramicroscopy* 210, 112928.

Hirth, J. P. & Lothe, J. (1982). *Theory of Dislocations*, Wiley, New York.

Huang, B. X., Huang, X. D., Wang, L. & Rong, Y.H. (2008) *Metall. Mater. Trans*. A. **39A**, 717-724.

Joy, D. C; Newbury, D. E; & Davidson, D. L. (1982) *J. Appl. Phys.* **53**, 81-122.

Joy, D.C. & Booker, G. R. (1971) *J Phys E Sci Instrum* **4**, 837.

Keijser, de Th. H. & Mittemeijer, E. J. (1980). *J. Appl. Cryst.* **13**, 74-77.

Kim, J. Y., Lee, S. J. & De Cooman, B.C. (2011). *Scr. Mater.* **65**, 363-366.

Lassen, N. C. K. (1996) *Mater Sci Technol.* **12**, 837-843.

Lassen, N. C. K; Jensen, D. J. & Conradsen, K. (1992) *Scanning Microsc.* **6**, 115-121.

Li, X.W. (2009). *Adv. Mater. Res.* **79-82**, 215-218.

Martin, S., Wolf, S., Martin, U., Krüger, L. & Rafaja, D. (2016) *Metal. Mater. Trans.* A. **47**, 49-58.

Mittemeijer, E. J. & Delhez, R. (1978). *J. Appl. Phys.* **49**, 3875-3878.

Müllner, P. & Ferreira, P.J. (1996). *Philos. Mag. Lett.* **73**, 289-297.

Naresh-Kumar, G; Trager-Cowan, C. & Mingard, K. P. (2019) *Microsc. Microanal.* **25**, 504-505.

Nishikawa, S. & Kikuchi, S. (1928a) *Nature* **122**,726-726.

Nishikawa, S. & Kikuchi, S. (1928b) *Nature* **121**,1019-1020.

Olson, G.B. & Cohen, M. (1976). *Metall. Trans. A.* **78**, 1897-1923.

Paterson, M. S. (1952). *J. Appl. Phys.* **23**, 805-811.

Pereira-da-Silva, M. de Assumpçao. & Ferri, F.A. (2017) Scanning electron microscopy *Nanocharacterization Techniques*, William Andrew Publishing, 1-35.

Pierce, D.T., Jimenez, J.A., Bentley, V., Raabe, D., Oskay, C. & Witting, J.E. (2014). *Acta Mater.* **68**, 238-253.

Ray, I.L.F. & Cockayne, D. J. H. (1971). *Proc. R. Soc. Lond. A.* **325**, 543-554.

Ruff Jr. A.W. (1970). *Metall. Trans.* **1**, 2391-2413.

Sahu, P., Shee, S. K., Hamada, A. S., Rovatti, L., Sahu, T., Mahato, B., Ghosh Chowdhury, S., Porter, D.A. & Karjalainen, L.P. (2012). *Acta Mater.* **60**, 6907-6919.

Scherrer, P. & Gottinger Nachrichten (1918). **2**, 98-100.

Schmidt, N. H; Bildesorensen, J. B. & Jensen, D. J. (1991) *Scanning Microsc.* **5**, 637-643.

Schramm, R.E. & Reed, R.P. (1975). *Metall. Trans. A.* **6**, 1345-1351.

Singh, J.B., Sundaraman, M., Mukhopadhayay, P. (1988). *Phillos. Mag. A*, **57**, 499-523.

Smallman, R.E. & Ngan, A.H.W. Physical Metallurgy and Advanced Materials, Seventh edition, Elsevier Ltd, 2007.

Smallman, R.E.& Westmacott, K.H. (1957) *Philos. Mag.* **2**, 669-683.

Stokes, A. R. (1948). *Proc. Phys. Soc.*, London, **61**, 382-391.

Talonen, J., & Hanninen, H. (2007) *Acta Mater.* **55**, 6108-6118.

Teutonico, L.J. (1967). *Philos. Mag.* **15**, 959-967.

Trager-Cowan, C; Alasmari, A; Avis, W; Bruckbauer, J; Edwards, P R; Hourahine, B; Kraeusel, S; Kusch, G; Jablon, B. M; Johnston, R; Martin, R W; Mcdermott, R; Naresh-Kumar, G ; Nouf-Allehiani, M; Pascal, E; Thomson, D; Vespucci, S; Mingard, K; Parbrook, P J; Smith , M D; Enslin, J; Mehnke, F; Kneissl, M; Kuhn, C; Wernicke, T; Knauer, A; Hagedorn, S; S Walde, S; Weyers, M; Coulon, P-M; Shields, P A; Zhang, Y; Jiu, L; Gong, Y; Smith, R M; Wang, T & Winkelmann, A (2020) *IOP Conf. Ser.: Mater. Sci. Eng.* **891**, 012023.

Trager-Cowan, C; Sweeney, F; Trimby, P W; Day, A. P; Gholinia, A; Schmidt, N. H; Parbrook, P. J; Wilkinson, A. J. & Watson, I. M. (2007) *Phys. Rev. B.* **75**, 085301.

Turunen, M. J., Keijser, Th.H. de., Delhez, R., van der Pers, N. M. (1983). *J.*

Ungár, T. & Borbe´ly A. (1996). *Appl. Phys. Lett.* **69**, 3173-3175.

Ungar, T. & Ribarik, G. (2017) IOP Conf. Ser. Mater. Sci. Eng. **194**, 1-8.

Ungár, T. (2001). *Mater. Sci Eng. A.* **309-310**, 14-22.

Ungar, T., Dragomir, I., Revesz, A., Borbely, A. (1999) *J. Appl. Crystallogr.* **32**, 992-1002.

Ungár, T., Groma, I. & Wilkens, M. (1989). *J. Appl. Cryst.*, **49**, 26-34.

Ungár, T., Ott, S., Sanders, P., Borbély, A. & Weertman, J.R. (1998). *Acta Mater.* **46**, 3693-3699.

Ungar, T., Revesz, A. & Borbely, A. (1998) *J. Appl. Crystallogr.* **31**, 554-558.

van Berkum, J. G. M., Vermeulen, A. C., Delhez, R., de Keijser, Th.H.. & Mittemeijer, E. J. (1994). *J. Appl. Cryst.* **27**, 345-357.

Venables, J. A. & Harland, C. J. (1973.) *Philos. Mag.* **27**,1193-1200.

Veyssier, P. (1991). *ISIJ International.* **31**, 1028-1048.

Warren, B. E. & Averbach, B. L. (1950). *J. Appl. Phys.* **21**, 595-599.

Warren, B. E. & Averbach, B. L. (1952). *J. Appl. Phys.* **23**, 497-498.

Warren, B. E. (1959). *Prog. Met. Phys.* **8**, 147-202.

Warren, B. E. (1969). *X-ray diffraction*, Addison-Wesley, Reading, Mass.

Wells, O. C. (1999) *Scanning*. **21**,368-371.

Wilkens, M. (1970) *Phys. Status Solidi* (a) **2**, 359-370.

Wilkens, M. in: J.A. Simmons, R. de Wit, R. Bulloug (Eds.), (1970) Fundamental Aspects of Dislocation Theory Vol. II, Natl Bur. Stand. Publ., Washington, 1195-1221.

Wilkinson, A. J. & Hirsch, P. B. (1997) *Micron*. 28, 279-308.

William, D.B. & Carter, C.B. (2010). *Transmission Electron Microscopy*, second ed., Springer Science, NY, Vol-3.

Williamson, G.K. & Hall, W.H. (1953) *Acta Metall.* **1,** 22-31.

Part B

Case study with fine grain Fe-Mn-Al-C steel

Chapter 3

Material, its processing & the flow stress behavior

3.1 Material and experimental

A high-Mn steel with the nominal composition Fe-26Mn-1Al-0.14C (all compositions are in wt.%) was prepared by induction furnace melting followed by homogenization and hot rolling to an 8 mm strip at 1100°C with subsequent water quenching. It was then cold rolled without reversing the rolling direction in several passes to 50% reduction, with a pass strain about 10% and inter-pass time of 30 seconds. The cold rolling is followed by recrystallization heat treatment under protective argon environment at 700°C for 30 min, and final water quenching to RT, produced an area averaged grain size ~ 5μm. The initial microstructure was studied using EBSD in a Hitachi SU7000 ultra high-resolution scanning electron microscope at 20 kV, 6nA. Another specimen was also heat treated at 950°C for 30 min, and water quenched to RT, to obtain a coarse-grained microstructure with the average grain size of ~35 μm. Uniaxial tensile tests were carried out using A30 specimens (the cross-section: 6 × 2 mm (width × thickness) and the gauge length 30 mm) until failure in a Zwick Z 100 tensile testing machine (ZwickRoell, GmbH) at RT with a quasi static strain rate of $10^{-4\ s^{-1}}$.To minimise the scope of SFE alteration, the quasi static strain rate was chosen during deformation through adiabatic heating. The tensile tests were interrupted at 2%, 5% and 10% true strain levels to identify the early dislocation activity and also at 20% true strain to study the intermediate microstructure evolution. Some tensile tests were also performed until complete failure of the specimen, occurring at ~50% true strain.

The uniformly strained gauge regions of deformed samples were electrolytically polished to produce surfaces suitable for XRD, EBSD and ECCI investigations. XRD data acquisition of the differently strained specimens is carried out with an X-ray powder diffractometer (Bruker D8 Advance) operating in the Bragg-Brentano geometry using Ni-filtered CuK_α radiation that eliminates the K_β radiation in the X-ray spectrum. A step size of 0.02° and scan rate of 0.2°/min were adopted in the angular range of 40° - 150° during XRD experiments. The instrumental broadening and the peak shape parameters were evaluated from the X-ray powder patterns of LaB6, NIST SRM660b specimen. The EBSD and ECCI measurements of the deformed specimens were performed using a high-resolution field emission scanning electron microscope (FE-SEM, LEO 1530, Carl Zeiss SMT AG, Germany) equipped with an EBSD system (Channel 5, HKL software), a retractable standard four-quadrant BSE detector (KE developments), a beam current of 6 nA at 20 kV acceleration voltage and 120 μm aperture. The ECCI images were obtained operating at the working distance of 3–4 mm using signals of the BSE detector.

The tensile tested specimens were mechanically ground to about 100 μm thickness and few 3 mm disks were punched for TEM investigations. The disks were subsequently electropolished with a TenuPol–5 operating at 30 V DC and 40 mA using an electrolyte comprising of 90% methanol and 10% perchloric acid maintained at -20°C. TEM observations are carried out on a JEOL 2200FS electron microscope operating at 200 kV and equipped with a GATAN 994UltraScan® 1000XP imaging system.

3.2 Flow stress behavior

The true stress-strain ($\sigma - \varepsilon$) curve of the studied steel ('steel' subsequently refers to the fine-grained specimen, unless stated otherwise), along with the strain-hardening rate (SHR) curve as the secondary axis is plotted in Fig. 3.1(a). The coarse-grained specimen was also subsequently tensile tested under similar conditions and the true flow stress curve and the corresponding SHR are superimposed in Fig. 3.1(a). A direct comparison of the plastic flow behavior of two different grain-sized specimens in Fig. 3.1(a) indicate that grain refinement had almost no effect on the flow stress and that both specimens exhibit a comparably high final true stress and fracture strain, although the coarse-grained specimen shows marginally higher uniform elongation. The deformation behavior of coarse-grained high-Mn steels are amply reviewed in the literature (. De Cooman *et al.*, 2018). Thus, investigating grain size dependence of the flow stress was not the objective here, but the emphasis was on to critically examine the strain hardening behavior of the fine-grained steel and to identify the reason(s) for any twin deficiency.

It can be observed from Fig. 3.1(a) that the steel after some initial discontinuous yielding exhibits high tensile strength (true stress value) ~1.3 GPa with a failure true strain of ~ 50%. Interestingly, the corresponding SHR curve in Fig. 3.1(a) shows a nearly stable SHR of ~ 2 GPa (~ $\frac{G}{35}$, G is the shear modulus of the steel ~72 GPa) after yielding. This is in strong opposition with the strain hardening behavior of high-Mn steels containing 0–2 wt.% Al (Jin, & Lee, 2012), as they generally exhibit a five-stage strain hardening. In such steels, the SHR rapidly decreases after the onset of plastic deformation (stage A), followed by nearly constant region (stage B) and subsequent decrease (stage C). Another short constant hardening is observed at higher strains (stage D), and then SHR rapidly decreases near failure strain (stage

E) (Jin, & Lee, 2012; Gutierrez & Raabe, 2012). A noteworthy aspect in Fig. 3.1(a) is the absence of serrated flow behavior indicating absence of dynamic strain ageing (DSA), which is observed even at RT, but at high strains and commonly interpreted in terms of high interstitial C content of the steel (De Cooman *et al.*, 2018).

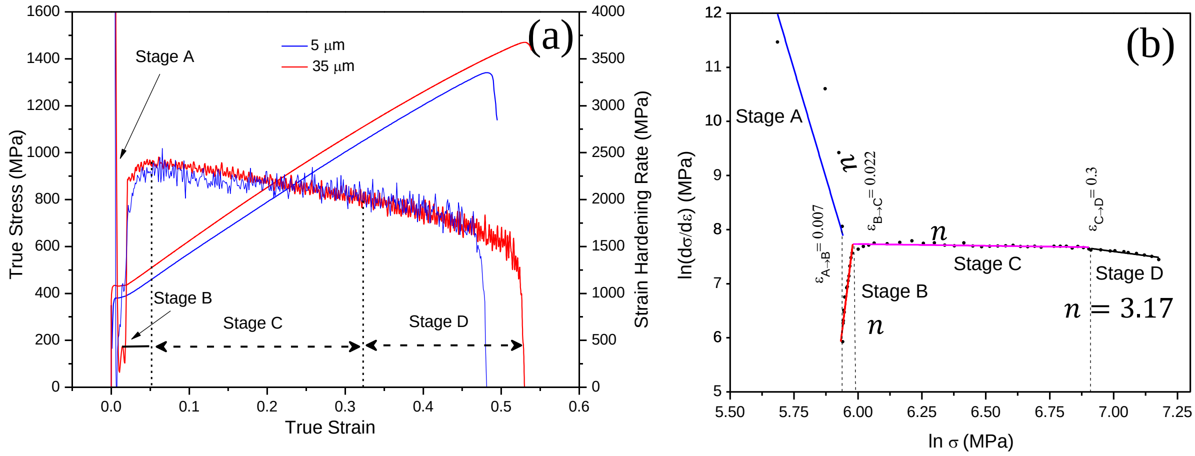

Fig. 3.1: (a) True stress-strain $(\sigma - \varepsilon)$ response and strain hardening rate curve of the steels. (b) $\ln\left(\frac{\mathrm{d}\sigma}{\mathrm{d}\varepsilon}\right) - \ln\sigma$ plot for modified C-J analysis for the fine grain

The strain hardening behavior of the present steel in Fig. 3.1(a) is further investigated following a modified Crussard–Jaoul (C-J) analysis (Jin & Lee, 2009) based on the Swift equation (Swift, 1952) and plotted in Fig. 3.1(b). The $\ln\left(\frac{d\sigma}{d\varepsilon}\right)$ vs. $\ln\sigma$ plot demonstrates four distinct stages (A–D) having different slopes $\left(1 - \frac{1}{n}\right)$ in between the transition strains ε_1, ε_2 and ε_3, wherein n is the strain-hardening exponent. The C-J analysis, Fig. 3.1(b), further shows that after a sharp drop in the strain range of 0–0.007 (ε_1 and stage A), the SHR increases in stage B to reach the constant level at a quite low strain ε_2 = 0.02, marking the onset of stage C that continues until ε_3 = 0.3, and thereafter the SHR decreases slightly in stage D, until the failure strain ~0.5. The respective n values for the deformation stages were 0.06, 0.03, 1.07 and 3.17. The n values interestingly indicate that the steel hardens at a constant rate within a wide strain range 0.02–0.3, which is not commonly reported in the literature for high-Mn steels. The present steel does, however, not reveal any stage E, while at the same time, stages C and D do not show any significant difference in Fig. 3.1(b), until the fracture. Thus, it is obligatory to investigate the intermediate microstructures to interpret the strain hardening behavior, which is described in the next chapters.

References

Jin, J.-E. & Lee, Y.-K. (2009) *Mater. Sci. Eng.* A. **527**, 157-161.

Jin, J.-E. & Lee, Y.-K. (2012) *Acta Mater.* **60**, 1680-1688.

Gutierrez-Urrutia, I. & Raabe, D. (2012) *Acta Mater.* **60**, 5791-5802.

De Cooman, B.C., Estrin, Y. & Kim, S.K. (2018) *Acta Mater.* **142**, 283-362.

Swift, H.W. (1952) *J. Mech. and Phys. Sol.* **1**, 1-18.

Chapter 4*

Electron Backscattered Diffraction and Electron Channelling Contrast Imaging studies of the deformation microstructure

---

* This chapter is unpublished.

4.1 The pre-deformation microstructure

Notwithstanding few exceptions, it is accepted that the grain refinement down to the sub-micron regime (≤ 0.1 µm) results in a drop of strain hardening and in a reduction of the uniform elongation (Valiev *et al*., 2006; Estrin & Vinogradov, 2013). Fig. 4.1(a) shows the inverse pole figure (IPF) map of the initial recrystallized fine grain microstructure and the corresponding

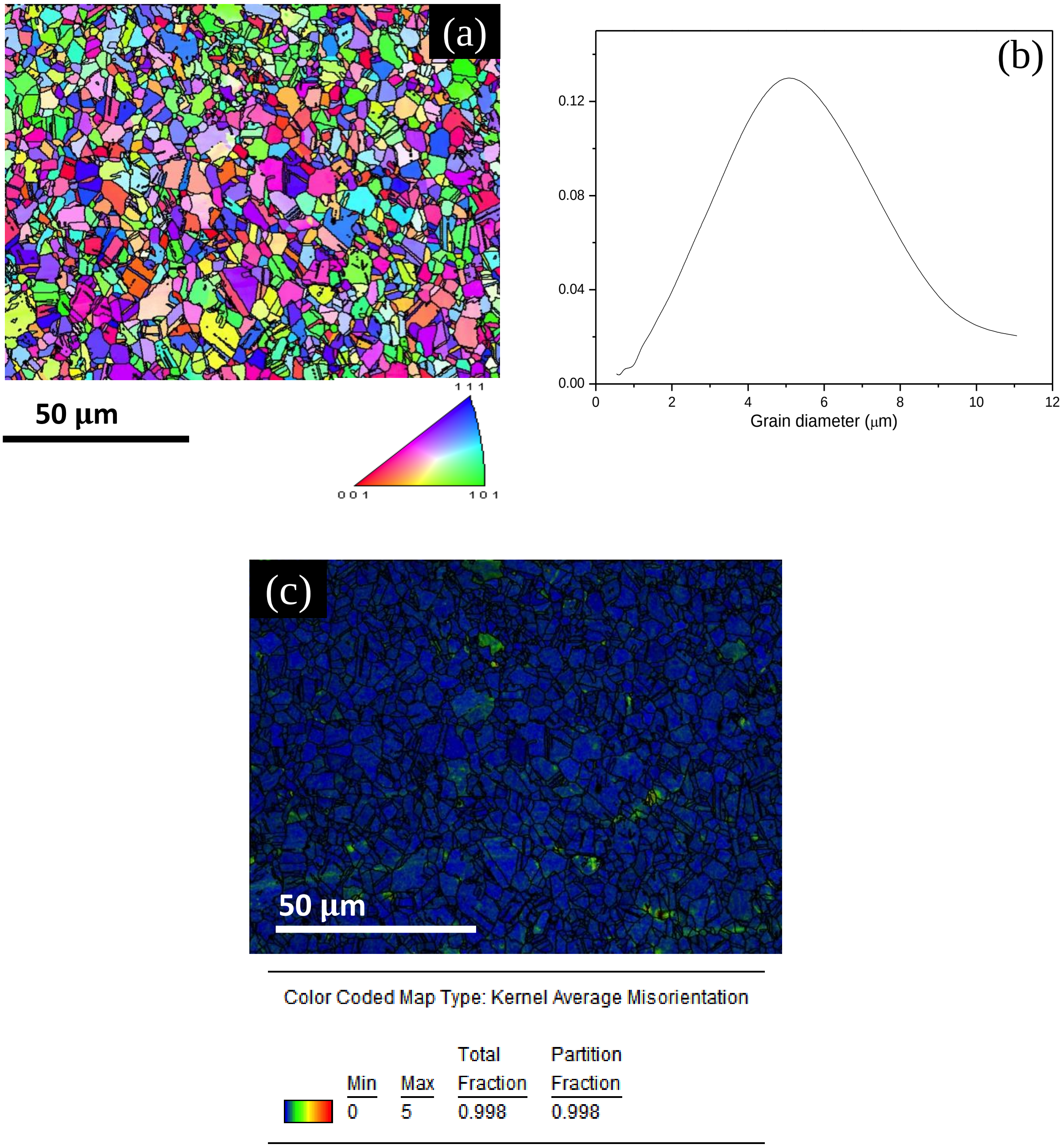

Fig. 4.1: (a) EBSD IPF map of the initial recrystallized microstructure. (b) Grain size distribution of EBSD micrograph (a). (c) KAM map corresponding to (a).

grain size distribution is displayed in Fig. 4.1(b). The thermomechanical treatments produced an average grain size ~ 5μm, measured from grain size distribution curve presented in Fig. 4.1(b). The corresponding Kernel Average Misorientation (KAM) map in Fig. 4.1(c) indicates that the specimen is in fully recrystallized condition.

4.2 HR-ECCI observations

Twins in high-Mn steels are reported to nucleate at stage B, corresponding to 2–5% true strains (Mahato *et al*., 2015; Idrissi *et al*., 2010; Mahato *et al*., 2017). Thus, corresponding microstructures were extensively investigated using microscopy techniques in the present

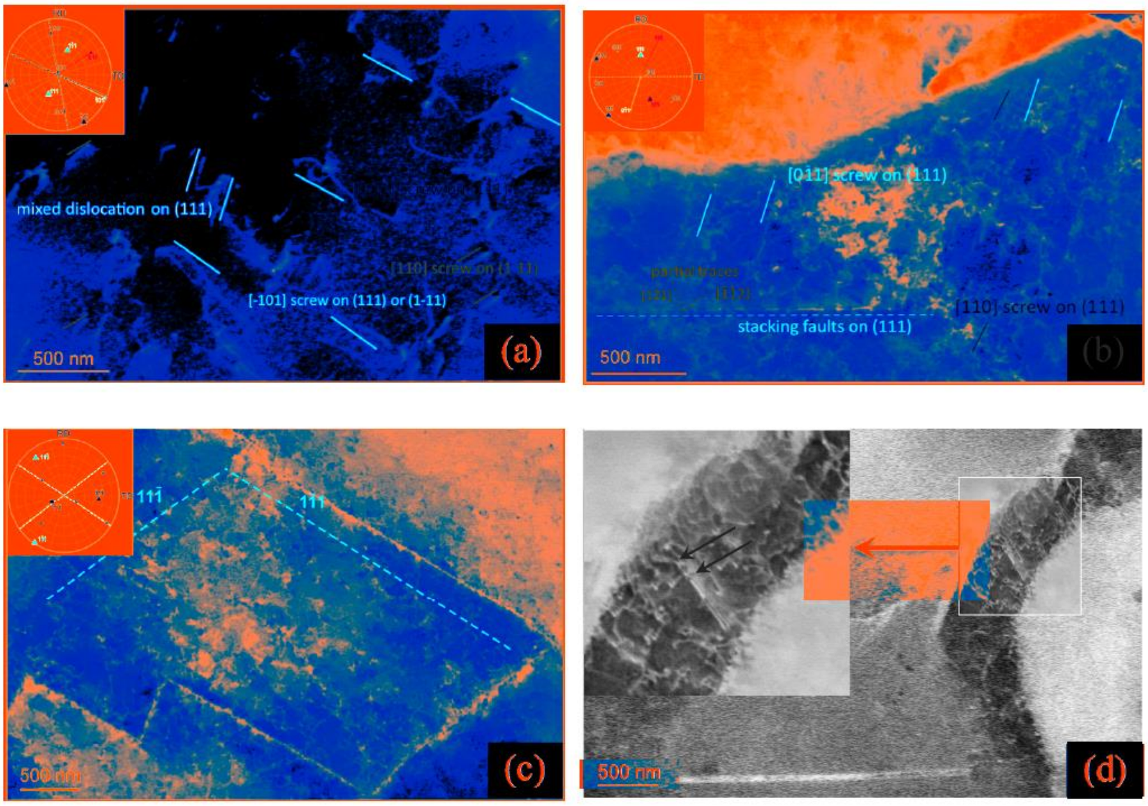

Fig. 4.2: SEM ECCI microstructure of low deformed specimens: (a) activation of multiple slip at 2% strain with screw dislocations dominating (b) formation of a rare SF on the primary slip system at 5% strain. The corresponding Shockley partials in (b) dissociate with distinct difference of the individual Schmid factors (Δm = 0.12). The traces of the dislocations in (a)-(c) are highlighted with respect to the stereographic projection of the corresponding grains presented as insets. (c) developments of dislocation tangles and Taylor lattice after 5% strain (d) nucleation of a deformation twin through overlapping SFs within weak dislocation cells after 10% strain. The periodic fringe contrasts of the individual SFs are indicated by a pair of black arrows in the enlarged region of the inset.

study. Figs. 4.2 and 4.3 show a set of differently oriented multi beam ECC images at different early strain levels representing the morphological evolution of various crystal defects, namely, dislocations, SFs and twins. The actual line directions of dislocations were estimated from the line trace and inclination (Gutierrez *et al.*, 2011). Fig. 4.2(a) reveals that multiple slip is activated at 2% strain on at least two sets of {111} planes and the dislocations appear as white lines in the enlarged ECC image. At least three distinguishably different sets of straight and slightly curved dislocations belonging to either screw or mixed character could be identified, whose traces are plotted in the stereographic projection (inset to Fig. 4.2(a)). Besides, some very short $\frac{a}{2}[0\bar{1}1]$ screw type dislocations on (111) planes could also be observed and labeled in green. Another observation at this stage is that dislocation activity was not only confined to activation of multiple slip but also protracted to the presence of few $\frac{a}{2}[0\bar{1}1]$ forest dislocations on {111} planes, also indicating about cross-slip and pronounced interaction among the dislocations at early strain. However, an astonishing feature of this microstructure is the absence of long SFs and it is unanimously accepted that SFs are ubiquitous in high-Mn steels, without which twinning cannot sustain in such steels, since they serve as the nuclei of twins (Idrissi *et al.*, 2010; Mahato *et al.*, 2015; Mahato *et al.*, 2017).

As the straining proceeds to 5%, Fig. 4.2(b) shows that the screw dislocations are elongated in their screw direction and that they trail wavy traces corresponding to extensive cross-slip between primary and conjugate planes. An isolated SF on the (111) plane was first observed in this microstructure at this strain (Fig. 4.2(b)), and this is indeed a sporadic observation for the high-Mn steels, which reveal profuse twinning, unless restricted by an ultrafine grain size (Ueji *et al.*, 2008). One might contend that the SFs can easily be misinterpreted with dislocations in ECCI. However, SFs, unless extinct in agreement with the $\vec{g}.\vec{R}$=0 criterion, always appear as sharp straight white lines, while dislocations are seldom perfectly straight. The absence of randomly distributed SFs in the microstructure could also be justified by the low SF probability values (~ 10^{-4}). The SF in Fig. 4.2(b) further reveals the traces of Shockley partials with Burgers vectors $\frac{a}{6}[1\bar{2}1]$ and $\frac{a}{6}[\bar{1}\bar{1}2]$, which are created according to the following dislocation reaction:

$$\frac{a}{2}[0\bar{1}1]_{(111)} \rightarrow \frac{a}{6}[1\bar{2}1] + \frac{a}{6}[\bar{1}\bar{1}2] \qquad (4.1)$$

Further at this strain (5%), multiple slip becomes pronounced in all examined grains of Fig. 4.2(c), showing the slip traces and the corresponding stereographic projection in inset. A newer phenomenon in the microstructure of Fig. 4.2(c) is presence of dislocation tangles and arrays resembling Taylor lattice, a well-known phenomenon related to planar slip. The high-Mn steels are known to have a SFE ranging between ~ 20 and 40 mJ/m^2. The dislocation cell formation in such steels is rarely reported in the early stages of deformation (Gutierrez *et al*., 2011, 2013). Tangled dislocation structure in the present steel at early strain indicative of strong interaction between the dislocations also implicates that planar slip is gradually transformed to wavy slip, which is known to be beneficial towards excellent strength-ductility combinations in Fe-30Mn-2Al-1.2C (Gutierrez *et al*., 2016). Subsequently, the microstructure at 10% strain shows in Fig. 4.2(d) the first evidence of a nucleating twin amid weak dislocation cells, and that they also reveal the signature periodic contrast variation of the overlapping intrinsic-extrinsic SF pair constituting the twin lamella. Such contrast variations are usually observed under two–beam conditions in TEM (Mahato *et al*., 2015; Mahato *et al*., 2017) and could also be observed in ECCI, as indicated using a pair of white arrows in the magnified inset of Fig. 4.2(d).

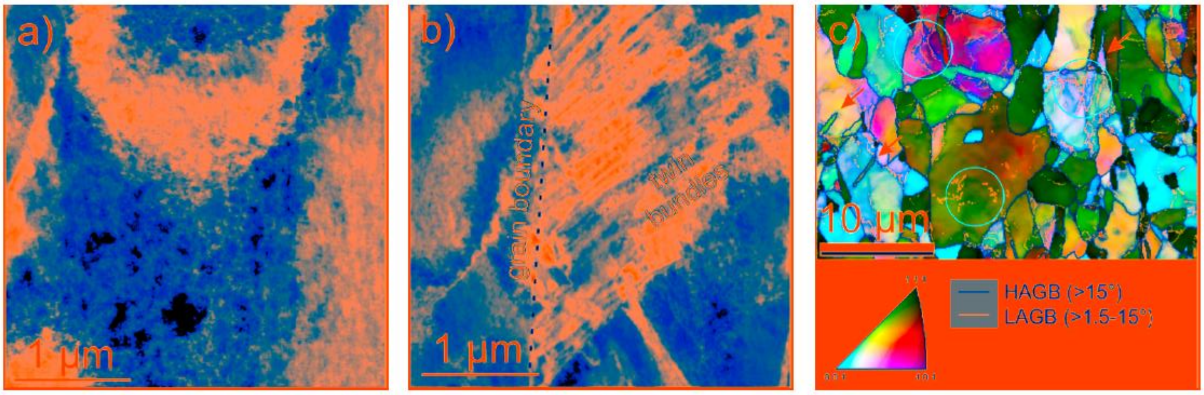

Fig. 4.3: SEM characterization of the microstructure at failure strain (~50%): (a) ECC-image showing pronounced dislocation cells (b) occasional deformation twin bundles in the vicinity of grain boundary (c) EBSD orientation map showing well developed orientation gradients originating from dislocation cells (some highlighted by circles) and some deformation nano twin bundles (arrows)

The presence of a prominent deformation twin bundle in the present steel could first be noted in the failed microstructure corresponding to 50% strain. However, the microstructure was still dominated by the dislocation tangles, and cells and twins were rather infrequently observed only within few relatively larger grains, which are presented in Figs. 4.3(a) and (b), respectively. It is known that the grain orientation with respect to the deformation direction plays a key role in activation and kinetics of twinning (Favier & Barbier, 2012) and is accountable towards activation of twinning system (Gutierrez *et al.*, 2010, 2011; Beladi *et al.*, 2011) in high-Mn steels. The grains oriented along ⟨111⟩ tensile axis are reported to be most preferred for twinning (Gutierrez *et al.*, 2011), while the ⟨001⟩ grains reveal dislocation cells with minimal or no deformation twins (Gutierrez *et al.*, 2010, 2016). In the present study, relatively larger grains revealed strong orientation gradients (Fig. 4.3(c)), which are attributable to the dislocation glide (planar and wavy). However, only one large deformation twin bundle could be detected in Fig. 4.3(b) and even the ⟨111⟩ grains remained devoid of twinning.

References

Beladi, H., Timokhina, I., Estrin, Y., Kim, J., De Cooman, B. C. & Kim, S. (2011) *Acta Mater.* **59**, 7787-7799.

Favier, V. & Barbier, D. (2012) *Scr. Mater.* **66**, 972-977.

Gutierrez-Urrutia, I. & Raabe, D. (2011) *Acta Mater.* **59**, 6449-6462.

Gutiérrez-Urrutia, I. & Raabe, D. (2016) *Acta Mater.* **60**, 5791-5802.

Gutierrez-Urrutia, I., Zaefferer, S. & D. Raabe. (2013) *JOM.* **65**, 1229-1236.

Gutierrez-Urrutia, I., Zaefferer, S. & Raabe, D. (2010) *Mater. Sci. Eng.* A. **66**, 3552-3560.

Idrissi, H., Renard, K., Ryelandt, L., Schryvers, D. &. Jacques, P. J. (2010) *Acta Mater.* **58**, 2464-2476.

Mahato, B., Sahu, T., Shee, S.K., Sahu, P., Sawaguchi, T., Kömi, J. & Karjalainen, L.P. (2017) *Acta Mater.* **132**, 264-275.

Mahato, B., Shee, S.K., Sahu, T., Ghosh Chowdhury, S., Sahu, P., Porter, D.A. & Karjalainen, L.P. (2015) *Acta Mater.* **86**, 69-79.

Ueji, R., Tsuchida, N., Terada, D., Tsuji, N., Tanaka, Y., Takemura, A. & Kunishige, K. (2008) *Scr. Mater.* **59**, 963-966.

Valiev, R. Z., Estrin, Y., Horita, Z., Langdon, T. G., Zehetbauer, M. J. & Zhu, Y. T (2006) *JOM.* **58**, 33-39.

*Chapter 5**

X-ray diffraction studies of the deformation microstructure

---

*This chapter is published in Materials Characterization, 172 (2021) 110833. (No. 1 in the list of publications)

5.1 X-ray line profile analysis (XLPA) of the deformation microstructure

X-ray line profile analysis (XLPA) has been an important characterization method in the study of deformed metals and alloys since it has immense potential to reveal the microstructural information through the estimations of dislocation density, crystallite size, faulting propensity and the active slip systems. In this chapter, the microstructural parameters of differently deformed microstructures are evaluated according to XLPA and reported in the following sections.

5.1.1 Normalized intensity profiles and the planar faults

The XLPA results of the differently deformed microstructure are presented in Table 5.1. The lattice parameters in Table 5.1 were estimated by extrapolating the apparent lattice parameters corresponding to individual Bragg reflections of the diffraction profiles at each strain levels to zero ($\theta = 90°$) of Nelson-Riley function: $f(\theta) = \frac{1}{2}\left(\frac{cos^2\theta}{sin\theta} + \frac{cos^2\theta}{\theta}\right)$ (Cullity & Stock, 2001). The normalized measured X-ray diffraction profiles for the first six Bragg reflections of specimens at 5% and failure (50%) strains are presented in Fig. 5.1, as a representative. These profiles expressed using normalized intensity versus $\frac{2(\sin\theta - \sin\theta_m)}{\lambda}$, where θ_m is the angular maxima of the corresponding Bragg reflections are essentially convolution of the instrumental profile and the true line broadened profile and thus, the parameters reported in Table 5.1 were

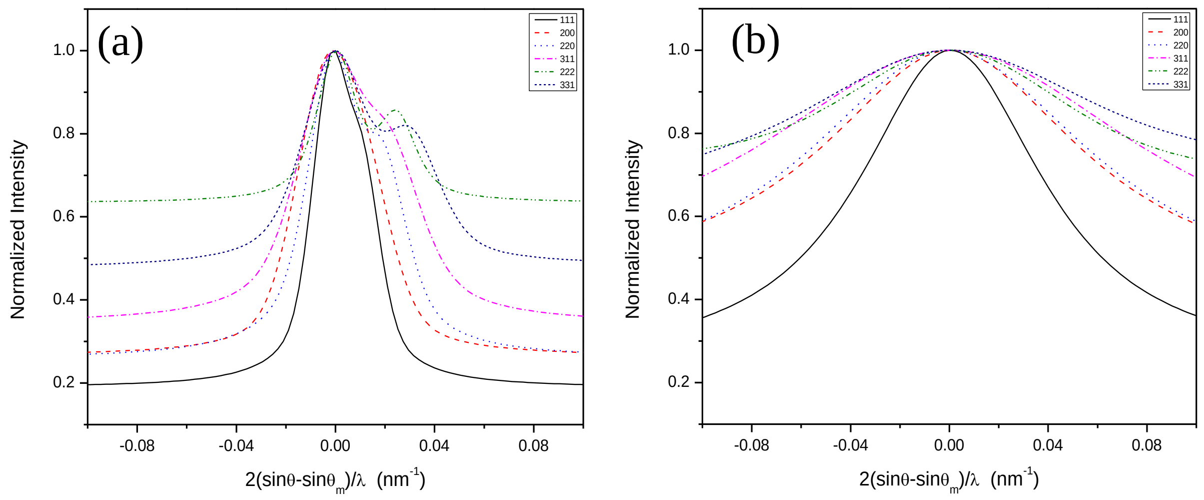

Fig. 5.1: Normalized X-ray diffraction profiles expressed in the intensity versus $2(\sin\theta - \sin\theta_m)/\lambda$ for specimens at: (a) 5% strain (b) failure (~ 50%) strain. The shoulders on the high angle side of profiles in (a) correspond to $K_{\alpha1} - K_{\alpha2}$ doublet.

subsequently estimated after deconvoluting the measured profiles according to methodology proposed by Enzo *et al.* (1988), which also accounts the consideration of $K_{\alpha1} - K_{\alpha2}$ doublet in the XLPA. It is seen from Fig. 5.1 that a larger broadening can be observed in the failed specimen Fig.5.1(b), compared to the 5% deformed specimen in Fig.5.1(a). It is further observed from Fig.5.1 that the (111) diffraction profile suffers from the minimum broadening, while the remaining Bragg reflections show higher broadening.

The planar faults in a deformed close-packed microstructure could be estimated in a statistically significant manner using XLPA, and two commonly used approaches, namely, Warren's (1969) and Balogh *et al*. (2006) approaches are available in the literature. In both these approaches, it is agreed that planar faults influence several aspects of a diffraction profile, namely, its shift, broadening and asymmetry, while Warren (1969) ascribed any asymmetry in the diffraction profile only to twin faults, especially through asymmetry in the (200) profile. Nonetheless, the planar fault analysis in the present study was carried out using Warren's approach of peak shift analysis (Warren, 1969), also reported previously (Mahato *et al.*, 2015).

Table 5.1: Microstructural parameters obtained using X-ray line profile analyses.

Strain	Lattice parameter, Å ±(0.0003-0.0006)	Contrast factor, C_{111} ± (0.01-0.02)	Dislocation character parameter, q	Dislocation density, ρ ($\times 10^{14}$ m^{-2}) ± (0.12-3.95)	Outer cut-off radius of dislocation, R_e (nm) ± (2-4)	Stacking fault probability, ($P_{sf}\times 10^{-4}$) ±(0.00001 - 0.0004)	Dislocation arrangement parameter, $M(= R_e\sqrt{\rho})$	SFE, γ (mJ/m^2) ± (5.5)
2%	3.6146	0.049	2.46	1.18	34	0.25	0.369	60
5%	3.6162	0.074	2.18	1.44	36	0.46	0.432	
10%	3.6133	0.065	2.29	1.78	37	0.51	0.494	
Failure (50%)	3.6088	0.095	1.96	24.86	43	11.02	2.144	

The absence of SFs in the differently deformed microstructure of the present steel could be directly interpreted from the negligible peak shift observed in Fig. 5.2(a) and 5.2(b), with respect to the annealed specimen, wherein, the normalized intensities of (111) and (200) Bragg reflections of differently strained specimens are plotted against $\frac{2(\sin\theta - \sin\theta_0)}{\lambda}$, where, θ_0 indicates the corresponding peak maxima of the annealed specimen. Also the corresponding peak shifts of (111) and (200) peak profiles for the differently deformed specimens are shown separately in Fig. 5.2(c), which were used to estimate the P_{sf} values reported in Table 5.1.

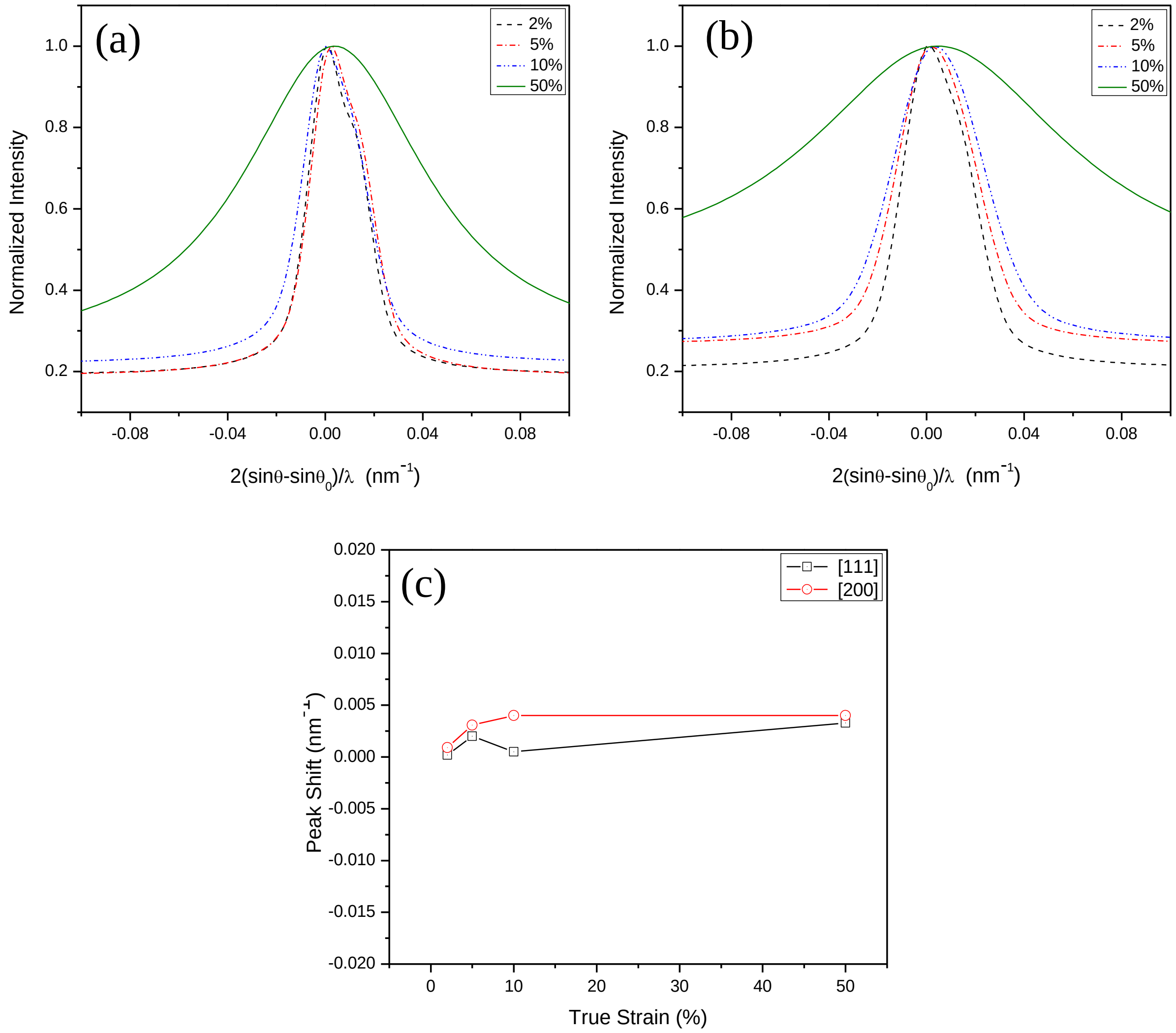

Fig. 5.2: Variation of normalized intensity with $2(\sin\theta - \sin\theta_0)/\lambda$ of differently strained specimens: (a) (111) Bragg reflections (b) (200) Bragg reflections (c) peak shifts of (111) and (200) Bragg reflections.

As revealed from Table 5.1, very low P_{sf} values (~ 10^{-4}) were obtained for the present steel. Such observation in deformed high-Mn steel is quite intriguing, for it is reported that high-Mn steels contain a high density of SFs (~ 10^{-3}), and that those SFs subsequently overlap to create a twin (Mahato *et al*., 2015; Lee *et al*., 2014). Further, the absence of prominent anisotropy in the diffraction profiles of Fig. 5.1 allows us to conclude that alike the SFs, no significant deformation twins are also present in the microstructure. At the same time, any anisotropy in the diffraction profiles, other than that induced by the presence of $K_{\alpha 1} - K_{\alpha 2}$ doublet should be attributed to stray occurrence of SFs in grains unfavorably oriented for observing such faults that can subsequently overlap to create twins (Gutierrez *et al*., 2010). The presence of twinning in the microstructure will be further inspected during the TEM observations (to be discussed subsequently in Chapter 6).

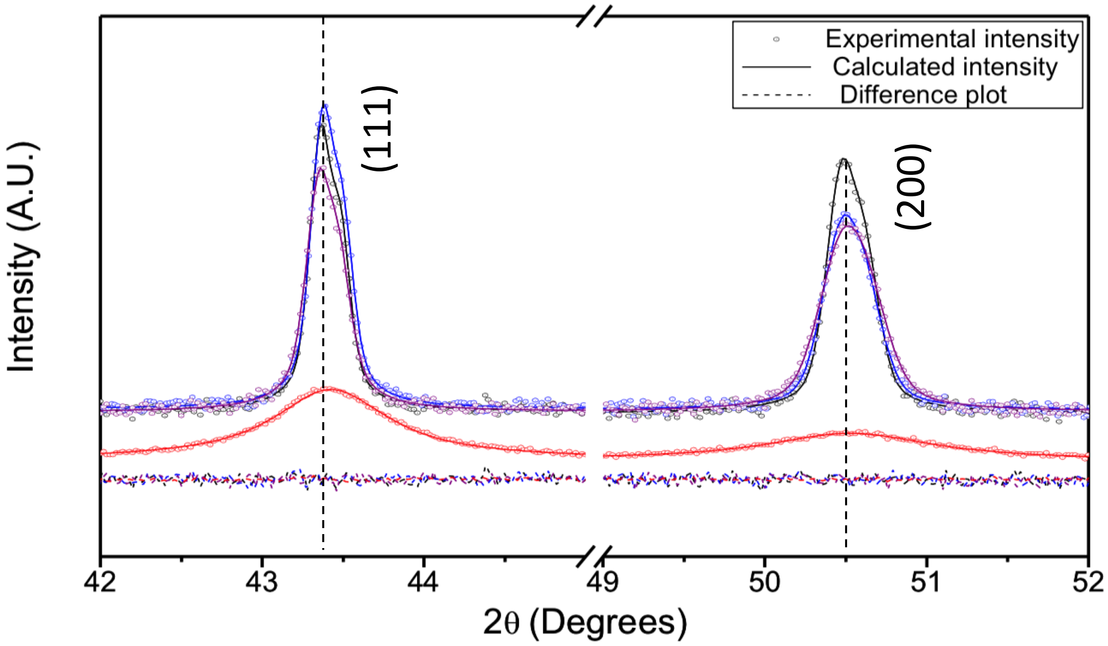

Fig. 5.3: pseudo-Voigt function fitted to (111) and (200) Bragg reflections of differently strained steel specimens: 2% (black), 5% (blue), 10% (purple) and 50% (red). The absence of opposite shifts in (111)–(200) Bragg reflections indicates insignificant contributions from stacking and twin faults in the microstructure.

It is well known from Warren's theory (Warren, 1969) that the presence of significant planar faults like SFs and twins in the microstructure bear their signature in the respective XRD patterns through manifestation of asymmetry and selective opposite shifts in the (111) and (200) Bragg reflections. In the presence of planar faults, the (111) reflection is shifted to a higher diffraction angle, while the (200) reflection is shifted towards lower angles, and also previously observed for high-Mn steels containing significant planar faults (Mahato *et al.*, 2015). On the other hand, twins (i.e. overlapping SFs) do not cause any opposite shifts, but they introduce asymmetry in the (111) diffraction profile. It is seen that the XLPA analyses of the (111) and (200) X-ray line profiles of austenite for different strain levels presented in Fig. 5.3 reveal neither asymmetry nor any noticeable opposing shifts. A detailed description about the peak shape parameters in the differently deformed specimens transcends the scope of the present report, but it has been described elsewhere and negligibly small densities of the planar fault parameters were estimated. Further, the relative intensities of the characteristic Bragg reflections at all terminal strains were in good agreement with values reported in the International Centre for Diffraction Data (ICDD), indicating weak texture development during uniaxial tension, which is also an important requirement for estimating planar faults in the microstructure using XLPA methods since such a situation would not violate the requirement of randomness in X-ray powder diffraction. It must be mentioned here that absence of planar faults in a deformed high-Mn steel microstructure is completely uncharacteristic in nature for such steels, as they have a major role in their deformation (De Cooman *et al.*, 2018). Therefore, in dearth of planar faults, it is expected that dislocations would be the key to controlling the deformation behavior of such steels, which is assessed in terms of the various dislocation related parameters accessible through contrast factor treatment of XLPA (Ungar *et al.*, 1998).

5.1.2 Influence of strain anisotropy on the Williamson-Hall plots

It is known that presence of dislocation induced strain broadening in the microstructure is confirmed through manifestation of scatter in conventional W-H plot, which is reassessed in Fig. 5.4(a) for the studied steel. The FWHMs obtained from Fig. 5.1 when further utilized in Eq. (2.15) (Chapter 2.2.4) to obtain the conventional W-H plots shown in Fig. 5.4(a), shows a significant scatter as a function of the diffraction vector, K, which indeed reaffirms the presence of significant dislocation induced anisotropic strain broadening. It is therefore imperative to invoke the concept of W-H plots modified according to Eq. (2.16) (Chapter 2.2.4), to assess if the presence of dislocation strain broadening be accounted for by the dislocation contrast factor approach (Ungar *et al.*, 1998).

Anisotropic crystallite sizes were obtained in the present study, which at 2% strain respectively had values: 131 nm and 95 nm along $\langle 111 \rangle$ and $\langle 200 \rangle$, and that they individually decrease to 19 nm and 12 nm at failure strain (~ 50%). However, a detailed description on the crystallite size variation with deformation is delimited here since the objective was to assess the parameters related to dislocations i.e. the dislocation strain broadening. Further, the parameter q in Eq. (2.18) (Chapter 2.2.4), signifying the character of dislocations within austenite is estimated directly from a linear fitting of Eq. (2.20) (Chapter 2.2.4) without assuming priori that equal proportion of $\frac{a}{2}\langle 110 \rangle$ edge and screw dislocations are present in the microstructure, and presented in Fig. 5.4(b) for varying tensile strains. The respective q values at each terminal strains are also shown in Table 5.1. Interestingly, the q value for the present steel was estimated to be: ~ 2.46 at 2% strain, remains stable within the accuracy limit until 10% strain, and finally dropping to ~ 1.96 at failure strain (~ 50%), signifying that the $\frac{a}{2}\langle 110 \rangle$ dislocations' character at early strain (until 10%) is predominantly screw type, while their population decreases at the failure strain i.e. the highest imposed strain. This interpretation is based on the reported values of q in austenite for pure edge and screw dislocations as: 1.71 and 2.46, respectively (Shintani & Murata, 2011). The variation of q values in the present steel with deformation (Table 5.1) is in contrast to several reports for austenitic and/or ferritic steels, wherein, the values were shown to increase monotonously with increasing deformation (Mahato *et al*., 2015; Simm, 2016).

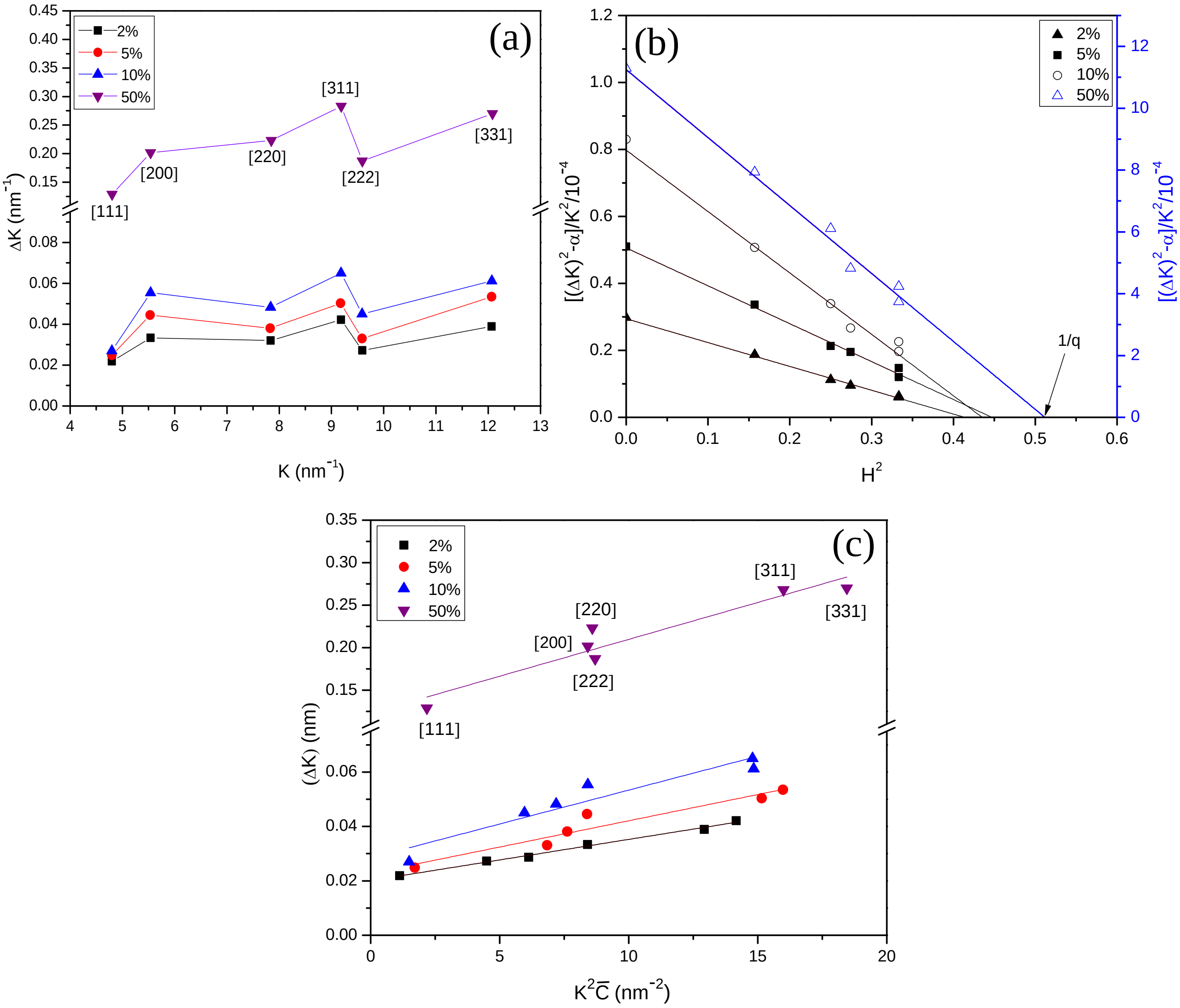

Fig. 5.4: (a) The *conventional* Williamson-Hall plot (b) linear fitting to the variation of $[(\Delta K^2)-\alpha]/K^2$ with H^2 according to Eq. (6) (c) the *modified* Williamson-Hall plot.

The predominance of screw dislocations in the present steel at early strains has the essential implication that cross-slip should be expected in the present steel at an early strain since the screw dislocations can easily change their habit planes by cross-slipping. On the other hand, a dropping q value ~ 1.96 in Table 5.1 at failure strain indicates towards some kind of decrease in the population of screw dislocations at this strain, viable through some kind of dislocation rearrangement that is synonymous to dynamic recovery of dislocations occurring near failure strain. It is worth mentioning that such a proposition to this effect is not put forward for high-Mn steels using an indirect method like the XLPA, while it is reported for Cu single crystals using TEM investigations (Gutierrez *at el.*, 2010), which will also be evaluated for the present steel in Chapter 6.

The same FWHMs of the differently deformed specimens from Fig. 5.1, when plotted against $K^2 C_{hkl}$ according to Eq. (2.16) (Chapter 2.2.4) reveal further in Fig. 5.4 (c) that significantly smoother curves are obtained for the early deformed specimens. It is however, also discernible from Fig. 5.4(c) that the scatters on the modified Williamson-Hall plots are not ignorable either in the specimen deformed to failure strain (~ 50%). A comparison of Figs. 5.4(c) and 5.4(a) thus indicate that invoking the effect of dislocation induced anisotropic strain broadening in XLPA analyses leads to significant improvement in the modified W-H plots, at least for low strains (until 10%), while any scatter in the modified W-H plots at higher strains could be due to some unexpected variations/rearrangement in the dislocation substructure before fracture, which will be investigated subsequently.

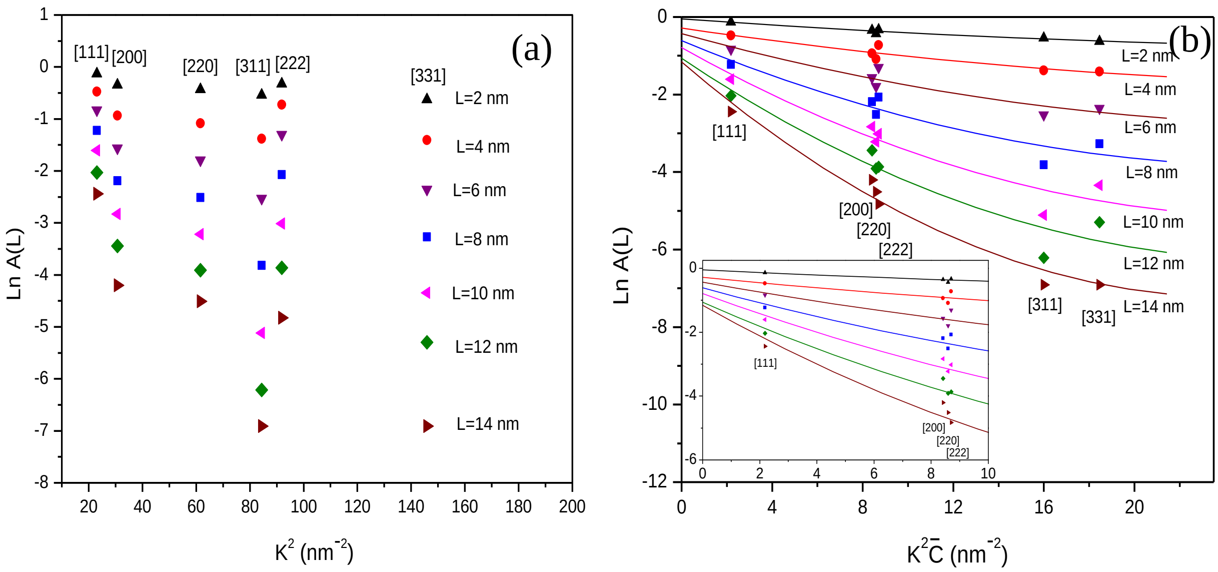

Fig. 5.5: Variation of logarithmic Fourier coefficient, $ln\,A(L)$, of the failed specimen ($\sim 50\%$ strain) at different L values according to: (a) *conventional* Warren-Averbach analysis (b) *modified* Warren-Averbach analysis.

5.1.3 Conventional and modified Warren-Averbach analysis

The real part of the Fourier coefficients, $A(L)$ for different Fourier lengths, (L), is calculated from the Fourier transformation of the normalized intensity versus $\frac{2(\sin\theta - \sin\theta_m)}{\lambda}$ plot

(Fig.5.1(a)), and scaled with the square of the diffraction vector, K^2, in Fig. 5.5(a) for the failed specimen, as a representative. It is again revealed from Fig. 5.5(a) that alike the conventional W-H plots in Fig. 5.4(a), $ln\,A(L)$s for different L in a conventional W-A plot reveal significant scatter, while comparatively smoother curves are obtained in Fig. 5.5(b) after fitting the quadratic curves according to modified W-A analysis when the $ln\,A(L)$s are scaled against $K^2\bar{C}$, wherein, $\bar{C}$ is related to $\bar{C}_{h00}$ and q through Eq. (2.18) (Chapter 2.2.4). It is additionally evident from the inset of Fig. 5.5(b) that a linear relationship between $ln\,A(L)$ and $K^2\bar{C}$ is maintained for all L values in the range of 2-10 nm, until first four Bragg reflections, and therefore, the slope of the liner region of $ln\,A(L)$ and $K^2\bar{C}$ plots would routinely determine $\rho\frac{\pi b^2}{2}L^2\ln\left(\frac{R_e}{L}\right)$, which will be discussed in the following.

5.1.4 Dislocation densities and characters in deformed microstructures

The outer cut-off radius and dislocation density values of the differently deformed specimens were calculated from the gradient and Y-intercept of Eq. (2.24) (Chapter 2.2.4), plotted in Fig.5.6 concerning the variation of $\frac{Y(L)}{L^2}$ with $ln(L)$. The corresponding parameters are also presented in Table 5.1, revealing that dislocation density is initially low (~10^{14} m^{-2}) at 2% strain, thereafter, increasing slowly until 10% strain, to attain the highest value (~10^{15} m^{-2}) at failure strain (~ 50%). Additionally, it is also noted from Table 5.1 that as the imposed plastic strain increases, the average contrast factor for (111) Bragg reflection, $\bar{C}_{111}$ also increases monotonously, implicating the profoundness in dislocation induced strain anisotropy at higher strains. The R_e values in Table 5.1 further reveal that they are quite low compared to other steel microstructures (Sahu *et al.*, 2012) and that they remain nearly constant until 10% strain (varies from 34 to 37 nm), while increasing moderately to ~ 43 nm at failure strain. The R_e values signify the level of shielding of the strain field of dislocations; and that a lower R_e value would suggest a higher degree of shielding of the strain field of dislocations by other dislocations, depending on the arrangement of dislocations (Wilkens *et al.*, 1970; Ungar *et al.*, 1998(b)).

Generally, R_e values for steel microstructures gradually decrease with increasing strains, essentially due to formation of strongly correlated dislocation substructures at large strains, namely, tangles, cells (Sahu *et al.*, 2012). In contrary, relatively low R_e values (~ 35 nm) were obtained in the present steel at the onset of deformation, while the highest R_e ~ 43 nm was estimated at failure strain (Table 5.1). Thus, the variation in R_e values in the present study indirectly indicate that the dislocations in the present steel become strongly correlated from the onset of deformation (2%), and that their correlation nearly remains invariant until 10% strain. The correlation however, decreases marginally at failure strain (50%), most likely through the occurrence of some dynamic recovery.

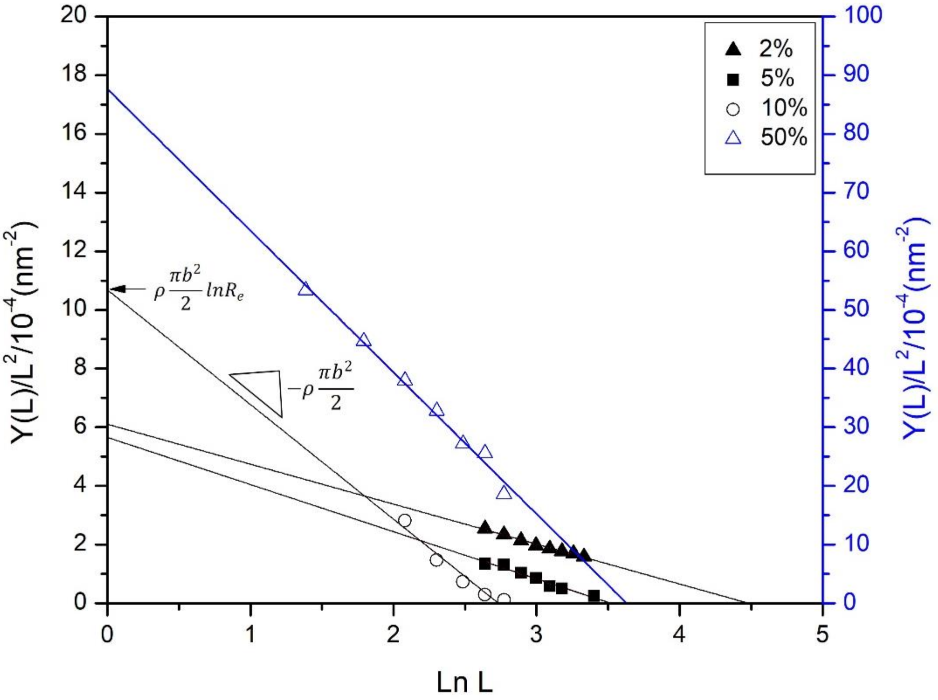

Fig. 5.6: Linear fitting to the variation of $Y(L)/L^2$ with $ln(L)$ according to Eq. (2.24).

An additional explanation could be put forward to explain the low R_e values observed in Table 5.1, and that when the strain fields of the individual dislocations screen each other, total distortion within the lattice is lowered, yielding a smaller value of R_e and consequently, the dislocations would arrange into dipoles and/or low angle grain boundaries (Gubicza, 2014). The application of this postulate in the present steel is being introspected subsequently using TEM. The dipole character of dislocations is further related to the dislocation arrangement parameter, M=$R_e\sqrt{\rho}$, signifying that the dipole arrangement is strong or weak in nature, depending on whether M is smaller or greater than unity, respectively (Wilkens, 1970; Borbely *et al.*, 2000). Interestingly, quite low value of M~ 0.36 was obtained in the present steel at the onset of deformation (2% strain) that slowly increases to M ~ 0.5 at 10% strain, and finally attaining a value M ~ 2.1 at the failure strain ~ 50% (Table 5.1).

It is therefore evident that dipole character of dislocation is prevalent in the studied steel even at early strain, which slowly decreases as the imposed strain increases. It is usually expected that at large strains, when newer dislocations are created in the microstructure, the dislocation densities increase and the dipole character becomes stronger (Ungar & Ribarik, 2017), which however, was not observed in the present study. In this case, the increasing plastic strain though had the effect of raising the densities of dislocations in Table 5.1, but their dipole character decreased gradually (gradually increasing M value in Table 5.1), which could be explained by the transformation of pre-existing dipoles created at 2% strain into more complex dislocation substructures at higher strains, namely, tangles and/or cells (Smallman & Ngan, 2000). It is noteworthy that such uncharacteristic evolution of the dislocation arrangement parameter with increasing plastic strain is not observed before in high-Mn steels, but seldom reported in dislocation cell forming metals like Cu (Ungar *et al.*, 1998), while its implication in the present steel will be directly investigated, based on TEM observations and which will be discussed in the Chapter 6.

5.1.5 Estimation of the stacking fault energy of austenite.

SFE is crucial for the deformation behavior of the austenitic steels (Martin *et al.*, 2016) and since the effective SFE value determined experimentally might be affected by the interaction of SFs with other microstructure defects (Mahato *et al.*, 2015; Rafaja *et al.*, 2014), I briefly outline here its estimation in the present study for completeness.

The complex nature of dislocation configurations in the present steel did not allow the estimation of SFE using the weak-beam dark-field imaging in TEM (Mahato *et al.*, 2015; Idrissi *et al.*, 2010). Therefore, the XRD approach proposed by Schramm and Reed (Schramm & Reed, 1975), and later modified by Dey *et al.* (2005) was employed for this purpose – in analogy with other recent studies (Mahato *et al.*, 2015, 2017). The modified Schramm and Reed method utilizes the relationship between γ, P_{sf}, ρ and a that was derived by Smallman and Westmacott (Smallman and Westmacott, 1957), and SFE of the steel is calculated according to Eq. (2.29) (Chapter. 2.6.1).

The various microstructural parameters used in the estimation of SFE according to Eq. (2.29) (Chapter. 2.6.1) are presented in Table 5.1 for different strain levels. The estimation of SFE from Eq. (2.29) (Chapter. 2.6.1) yields an average SFE value γ ~ 60 mJ/m^2, which is significantly higher than the values suggested by Kim and De Cooman (Kim & De Cooman, 2016) for such steels, although Welsch *et al.* (2016) reported high-Mn steels can have SFE value as high as: γ ~ 85 mJ/m^2. Also, the sub-regular solution model of SFE for high-Mn steels (Saeed–Akbari *et al.*, 2009) predicts γ ~ 25 mJ/m^2 for the present steel. However, it was shown previously (Mahato *et al*., 2015) that SFE in such steels is modified by several microstructural parameters related to various extended defects in the microstructure and thereby leading to the concept of effective or apparent SFE, which in such instances could manifest even more than two-fold increase from the ideal SFE (Mahato *et al*., 2015; Rafaja *et al*., 2014), while studying the energies of short interacting SFs in Cr–Mn–Ni steels have categorically reported that the classical method of SFE estimation (Schramm & Reed, 1975) does not hold well, when the various defects within the microstructure mutually interact. In the present instance, the microstructure features of the steel observed in TEM investigations indicated that the discrepancy between expected SFE and the effective SFE determined using XRD could be due to the presence of microstructural defects.

Intriguingly, Volosevich *et al.* (1976) proposed already in 1976 that the SFE of binary Fe-Mn alloys can be affected by the grain size. This hypothesis, which was later advocated by Takaki *et al*. (1993) and Lee and Choi (2000), is based on the grain size dependent internal stresses that cause a change in the dislocation dissociation width. A couple of propositions were put forward to explain the apparent SFE of high Mn steels, namely, the disequilibrium carbon concentration in the solid solution is high when the austenite is quenched from a relatively lower temperature or shorter time to produce a finer grain structure and then, the grain size might act as a geometric obstacle to the dissociation of dislocations, when it is smaller than the equilibrium width of SFs (Lee & Choi, 2000). There they also report that the effect is most pronounced when the grain size is 5 μm, and since the grain size in the present steel was identical and thus the high apparent SFE estimated through X-ray analyses could be corroborated from the report of Lee and Choi (Lee & Choi, 2000).

References

Balogh, L., Ribarik, G. & Ungar, T. (2006) *J. Appl. Phys*. **100**, 023512(1-10).

Borbely, A., Driver, J. H. & Ungar, T. (2000) *Acta mater*. **48**, 2005-2016.

Bracke, L., Kestens, L. & Penning, J. (2009) *Scr. Mater*. **61**, 220-222.

Cullity, B. D. & Stock, S. R. (2001). Elements of X-ray Diffraction, Third Edition. Prentice-Hall.

De Cooman, B. C., Estrin, Y. & Kim, S. K. (2018) *Acta Mater.* **142**, 283-362.

Dey, S.N., Chatterjee, P. & Sen Gupta, S. P. (2005) *Acta Mater*. **53**, 4635-4642.

Enzo, S., Fagherazzi, G., Benedetti, A. & Polizzi, S. (1988) *J. Appl. Cryst*. **21**, 536-542.

Gubicza, J. (2014) X-Ray Line Profile Analysis in Materials Science, IGI Global, Hershey.

Gutierrez-Urrutia, I., Zaefferer, S., Raabe, D. (2010) *Mater. Sci. Eng.* A. **527**, 3552-3560.

Idrissi, H., Renard, K., Ryelandt, L., Schryvers, D. & Jacques, P. J. *Acta Mater.* 58 (2010) 2464-2476.

Karaman, I., Sehitoglu, H., Chumlyakov, Y. I., Maier, H. J. & Kireeva, I. V. (2001) *Metall. & Mat. Trans.* A. **32**, 695-706.

Le Bail, A. (1985) Proc. 10th Colloque Rayons X. Siemens, Grenoble, 45-58.

Lee, S. J., Jung, Y. S., Baik, S. I., Kim, Y. W., Kang, M., Woo, W. & Lee, Y.K. (2014) *Scr. Mater.* **92**, 23-26.

Lee, Y.-K. & Choi, C. (2000) *Metall. Mater. Trans.* A **31**, 355-360.

Luo, Z. C. & Huang, M. X. (2018) *Scr. Mater.* 142, 28-31.

Lutterotti, L. & Scardi, P. (1990) *J. Appl. Cryst.* **23**, 246-252.

Mahato, B., Sahu, T., Shee, S.K., Sahu, P., Sawaguchi, T., Kömi, J. & Karjalainen, L.P. (2017) *Acta Mater.* **132**, 264-275.

Mahato, B., Shee, S.K., Sahu, T., Ghosh Chowdhury, S., Sahu, P., Porter, D.A. & Karjalainen, L.P. (2015) *Acta Mater.* **86**, 69-79.

Martin, S., Wolf, S., Martin, U., Krüger, L. & Rafaja, D. (2016) *Metal. Mater. Trans.* A. **47**, 49-58.

Rafaja, D., Krbetschek, C., Ullrich, C. & Martin, S. (2014) *J. Appl. Cryst.* **47**, 936-947.

Saeed–Akbari, A., Imlau, J., Prahl, U. & Bleck, W. (2009) *Metall. Mater. Trans.* A. **40**, 3076-3090.

Sahu, P., Shee, S.K., Hamada, A.S., Rovatti, L., Sahu, T., Mahato, B., Ghosh Chowdhury, S., Porter, D.A. & Karjalainen, L.P. (2012) *Acta Mater.* **60**, 6907-6919.

Scardi, P., Ermrich, M., Fitch, A., Huang, E-Wen., Jardin, R., Kuzel, R., Leineweber, A., Mendoza. Cuevas, A., Misture, S. T., Rebuffi, L. & Schimpf, C. (2018) *J. Appl. Cryst.* **51**, 831-843. 5-599.

Shintani, T. & Murata, Y. (2011) *Acta Mater.* **59**, 4314-4322.

Simm, T. H., Withers, P. J. & Quinta da Fonseca, J. (2016) **111**, 331-343.

Smallman, R. E. & Ngan, A. H.W. (2007) *Physical Metallurgy and Advanced Materials*, Seventh edition. Elsevier Ltd.

Smallman, R. E. & Westmacott, K. H. (1957) *Philos. Mag.* **2**, 669-683.

Stokes, A. R. & Wilson, A. J. C. (1944) *Proc. Phys. Soc.* **56**, 174-181.

Takaki, S., Nakatsu, H. & Tokunaga, Y. (1993) *Mater. Trans. JIM.* **34**, 489-495.

Ueji, R., Tsuchida, N., Terada, D., Tsuji, Y., Tanaka, Y., Takemura, A. & Kunishige, K. (2008) *Scr. Mater.* **59**, 963-966.

Ungar, T. & Borbely, A. (1996) *Appl. Phys. Lett.* **69**, 3173-3175.

Ungar, T. & Gubicza, J. (2007) *Z. Kristallogr.* **222**, 114-128.

Ungar, T. & Ribarik, G. (2017) *IOP Conf. Ser. Mater. Sci. Eng.* **194**, 1-8.

Ungar, T. (2008) *Powder Diffr.* **23**, 125-132.

Ungar, T., Dragomir, I., Revesz, A. & Borbely, A. (1999) *J. Appl. Cryst.* **32**, 992-1002.

Ungar, T., Gubicza, J., Ribarik, G. & Borbely, A. (2001) *J. Appl. Cryst.* **34**, 298-310.

Ungar, T., Ott, S., Sanders, P. G., Borbely, A. & Weertman, J R. (1998) *Acta Mater.* **46**, 3693-3699.

Ungar, T., Revesz, A. & Borbely, A. (1998) *J Appl. Cryst.* **31**, 554-558.

Ungar, T., Victoria, M., Marmy, P., Hanak, P. & Szenes, G. (2000) *J. Nucl. Mater.* **276**, 278-282.

Volosevich, P., Gridnev, V. & Petrov, Y. (1976) *Phys. Met. Metallogr.* **42**, 126-130.

Warren, B.E. (1969) X-ray diffraction, Addison-Wesley. Reading.

Welsch, E., Ponge, D., Hafez Haghighat, S.M., Sandlobes, S., Choi, P., Herbig, M., Zaefferer, S. & Raabe, D. (2016) *Acta Mater.* **116**, 188-199.

Welsch, E., Ponge, D., Hafez Haghighat, S.M., Sandlobes, S., Choi, P., Herbig, M., Zaefferer, S., Schramm, R.E. & Reed, R.P. (1975) *Metall. Trans.* A. **6**, 1345-1351.

Wilkens, M. (1970) *Phys. Status. Solidi* (a). **2**, 359-370.

Wilkens, M. (1970) J. A. Simmons, R. de Wit, R. Bulloug Eds., Vol. II, Natl Bur. Stand. Publ., Washington, , 1195-1221.

Chapter 6*

TEM investigations of the deformation microstructure and the paradigm of twinning

---

*The contents of this chapter are published in Materials Characterization, 172 (2021) 110833 (No. 1 in the list of publications), Materialia 15 (2021) 101042 (No. 2 in the list of publications), Materials Letters, 300 (2021) 130216 (No. 3 in the list of publications) & communicated to Metallurgical and Materials Transactions A.

6.1 Transmission electron microscopy investigations and its implications on the deformation mechanism

In this chapter, TEM investigations of the differently deformed specimens are reported and the corresponding implications on the deformation mechanism(s) are critically introspected. The following sections aim to reveal the active deformation mechanism prevailing in the steel at various strain levels from a TEM point of view and its correlation to the identified deformation behavior.

6.1.1 Planarity of slip and low energy dislocation structures at early strains (2% and 5%)

The early deformation microstructures of high-Mn steels reveal important information about the deformation mechanism(s) for that the nucleation of twins and/or early dislocation activities generally becomes clear before 5% true strain (De Cooman *et al.*, 2018). The early dislocation activities in the steel are presented through a set of bright field (BF) and dark field (DF) TEM micrographs shown in Fig. 6.1. Fig. 6.1 shows a set of high magnification micrographs of the 2% deformed specimen acquired along electron beam direction $B \approx [111]$, revealing the activation of multiple slip which is also observed in ECCI (Fig. 4.2(a) in Chapter 4.2) and the interaction among different $\frac{a}{2}\langle 110\rangle$ dislocations on the $\{111\}$ planes. The BF image in Fig. 6.1(a) demonstrates the first case, where the impingement between $\frac{a}{2}[01\bar{1}]$ and $\frac{a}{2}[\bar{1}01]$ dislocations having screw components and a $\frac{a}{2}[1\bar{1}0]$ dipole dislocation takes place on parallel (111) planes.

The corresponding weak beam dark field (WBDF) image in Fig. 6.1(a) under a $\mathrm{g} - 3\mathrm{g}$ diffraction condition in selected area diffraction (SAD) pattern inset, reveals that the dislocation segment having the Burgers vector $\frac{a}{2}[01\bar{1}]$ is showing a strong contrast and is also parallel to the $\mathrm{g}_{02\bar{2}}$ diffraction vector. Hence, it is in a near screw orientation and pinned at the two points indicated by red arrows. In other words, it is locked in the screw direction, while the dipole segment (*i.e.* $\frac{a}{2}[1\bar{1}0]$) showing weaker contrast is predominantly edge in nature (the character angle between the diffraction vector and dislocation line, $\beta' \sim 60°$) (Pierce *et al.*, 2014; Mahato *et al.*, 2015; Laplanche *et al.*,2017), bows under the action of the local stress field. Hence, a jog is formed on either side of the $\frac{a}{2}[1\bar{1}0]$ dipole dislocation, considering that the impingement of the two dislocations is on parallel slip planes (see legend in Fig. 6.1(a)).

The locked dislocation ($\frac{a}{2}[01\bar{1}]$ or $\frac{a}{2}[\bar{1}01]$) prevents the pivot point from being trailed in the cross-slip plane under the tension exerted by the bowing dislocation (*i.e.* $\frac{a}{2}[1\bar{1}0]$ segment). This would result in an L-shaped, hairpin like dislocation configuration along the moving

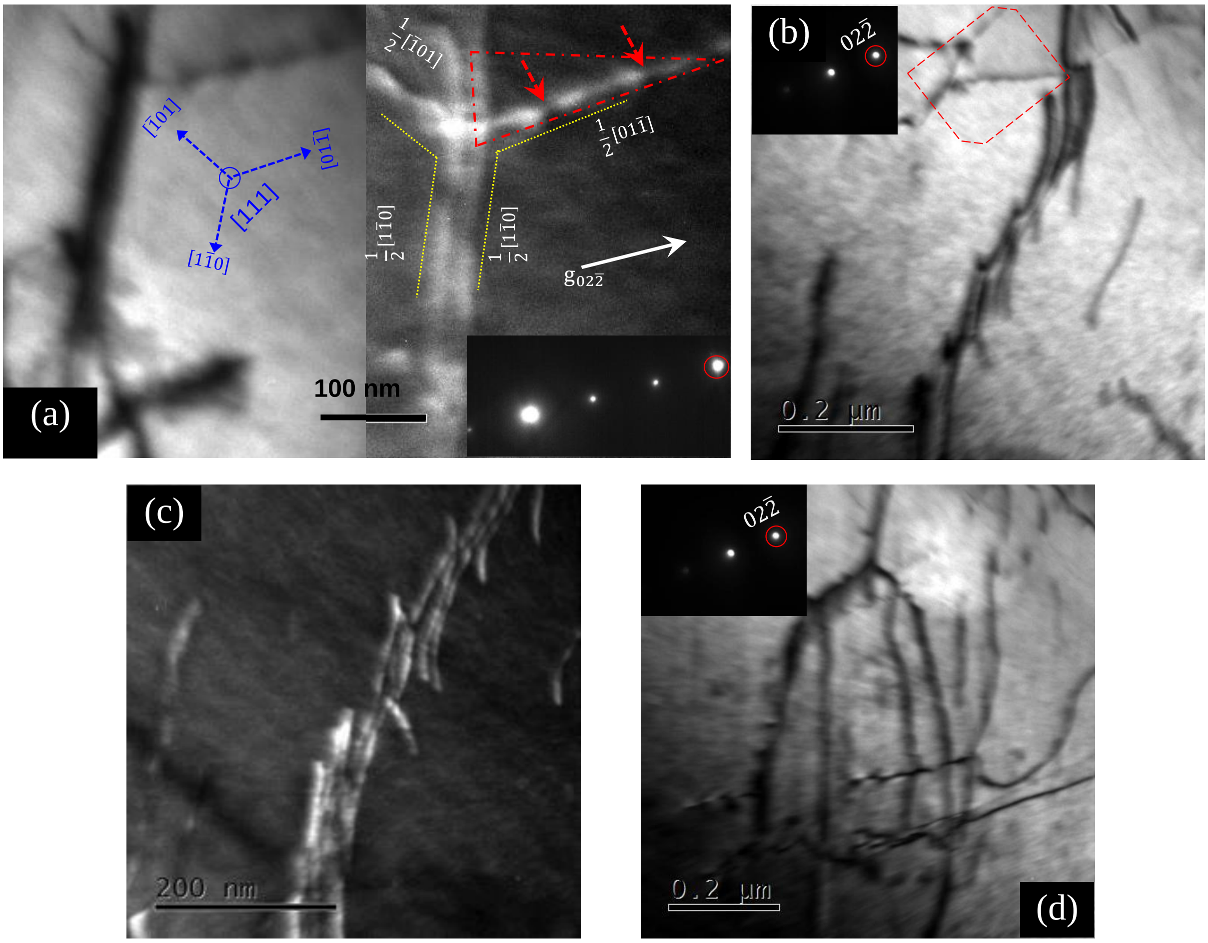

Fig. 6.1:Micrographs at 2% strain showing early dislocation activities: (a) high magnification BF and DF imaging in $B \approx [111]$ with strong and weak $g_{02\bar{2}}$ beam, respectively, showing impingement of pinned $\frac{a}{2}[01\bar{1}]$ and $\frac{a}{2}[\bar{1}01]$ screw dislocations with $\frac{a}{2}[1\bar{1}0]$ dipole dislocation. The dotted yellow segments on either side of the $\frac{a}{2}[1\bar{1}0]$ dipole will be jogged for impingement on parallel (111) planes. The unpinned segment having Burgers vector: $\frac{a}{2}[1\bar{1}0]$ would bow under the external stress to form a cross-slip loop string. (b) Formation of dislocation multipoles with strong $g_{02\bar{2}}$ beam. A truncated loop string is delineated using the red lines. (c) The corresponding weak beam image of (b). (d) The early stages of a Taylor lattice formation under two-beam BF condition in $B \approx [111]$.

dislocation, better known as prismatic loop strings formed through truncation of the dipole by coordinated cross-slip (Steeds, 1966; Shiet *et al*., 1995). This mechanism, interpreted as cross-slip truncation (CST) mechanism, involves the impingement of two dislocations moving on parallel slip planes with different velocities such that they mutually annihilate by coordinated cross-slip (Veyssiere & Gregori, 2002a). These loop strings are usually only observed in some single crystals deformed in single slip involving $\frac{a}{2}\langle 110\rangle$ dislocations with screw components (Veyssiere & Gregori, 2002a): they have never been reported in high-Mn steels. A prismatic loop string forms when the red delineated region in Fig. 6.1(a) truncates from the initial jogged configuration through cross-slip. In agreement with this, the BF micrograph presented from a different grain in Fig. 6.1(b) shows a truncated loop string in the region outlined in red, which seemingly terminated from the jogged configuration seen in Fig. 6.1(a) (Veyssiere & Gregori, 2002b) formed through the pinning of $\frac{a}{2}\langle 110\rangle$ screw dislocations (Cailllard & Legros, 2013). Fig. 6.1(b) further shows a group of bowed dislocation multipoles under a strong $g_{02\bar{2}}$ reflection. The corresponding WBDF image depicted in Fig. 6.1(c) shows the near edge nature (β' ~ 70°) of the dislocations constituting the multipoles. These multipoles align along the primary slip direction, and are formed by the cross-slip led juxtaposition of edge dislocations (Jackson, 1983). To our knowledge, Kim *et al*. (2019) have reported only about the role of dislocation multipoles in the plasticity of high-Mn steels. They observed that such multipoles are created through successive cross-slip events and represent an energetically stable configuration.

Fig. 6.1(d) further exemplifies the situation in a new grain; wherein, the interaction of $\frac{a}{2}\langle 110\rangle$ dislocations via selective planar glide occurs on a single $\{111\}$ plane. This glide of $\frac{a}{2}\langle 110\rangle$ dislocations is a consequence of the 'glide plane softening effect', arising from the short-range ordering (SRO) induced by Al, resulting in well-known Taylor lattice formation (Park, 2013). A Taylor lattice forms at early strains as a result of pronounced planar glide on the most highly stressed glide planes without any systematic lattice rotations and/or also through alignment of cross-slip led edge components of the loop strings (Kuhlmann-Wilsdorf, 1989). Taylor lattice and loop strings are LEDS, whose contribution to strain hardening is still unclear (Park, 2013; Kuhlmann-Wilsdorf, 1989).

The high magnification BF micrograph, Fig. 6.2(a), reveals that a Taylor lattice is formed at 2% strain through the activation of at least two non-coplanar slip system.

Furthermore, two low magnification overview BF micrographs are also presented as Fig. 6.2(b) corresponding to the specimen deformed at 5% strain. The main image in Fig. 6.2(b) demonstrate that at this strain (5%), a dislocation substructure engulfs the whole grain delineated using red, while the lower insert confirms that the Taylor lattice is also extended to

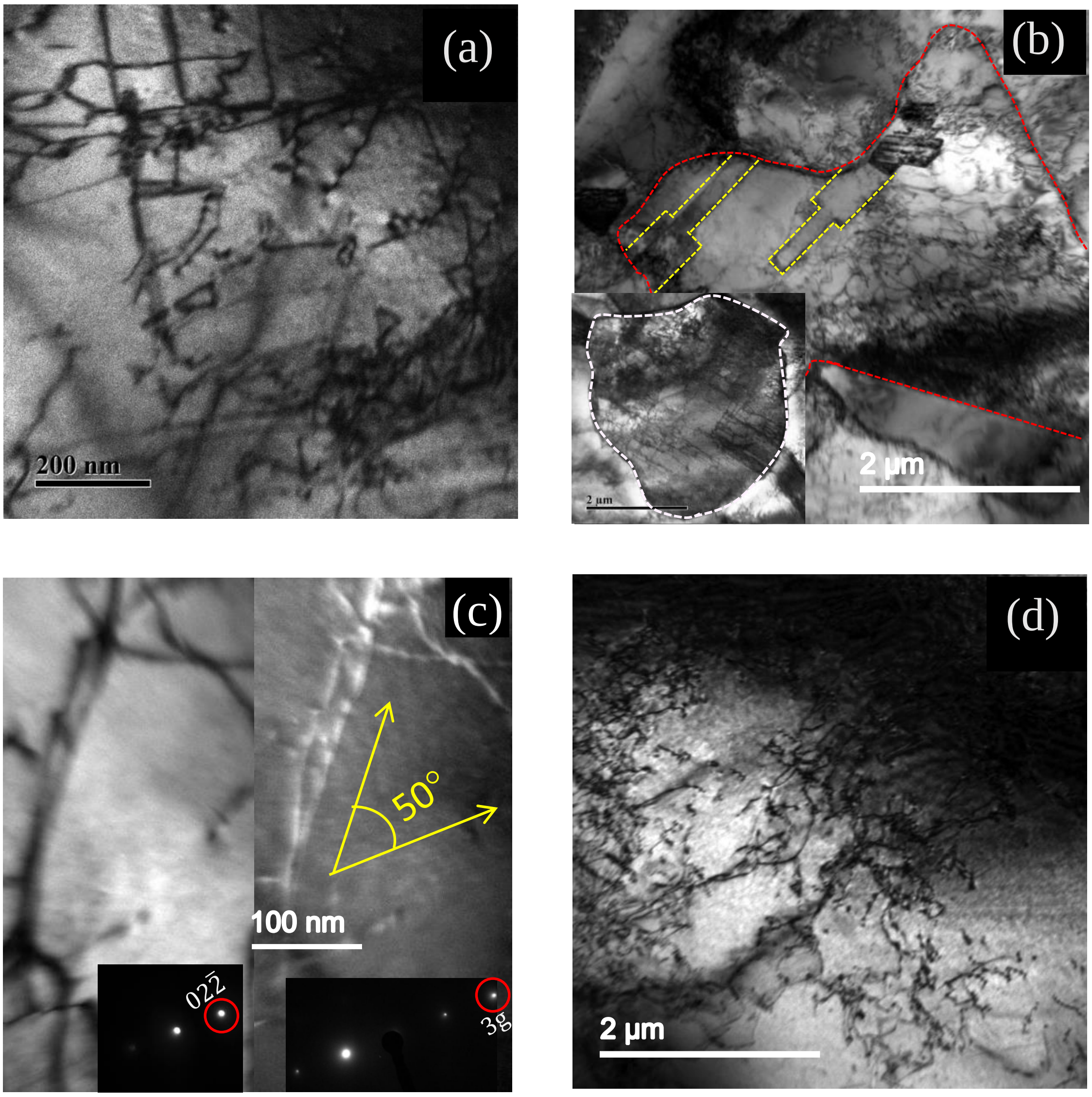

Fig. 6.2: Low-deformed TEM microstructures along $B \approx [011]$ showing: (a) a high magnification multi-beam BF image of Taylor lattice at 2% strain (b) multi-beam BF images of dislocation substructure extending to grain interior at 5% strain (under low magnification) – the grain is delineated using red and the grain also contains two annealing twins outlined using yellow; the lower inset also shows an overview image of a grain (delineated using white lines) wherein the Taylor lattice is extended (c) dislocation dipole under BF and WBDF at 2% strain in two-beam and the corresponding g-3g conditions (d) a low magnification multi-beam BF image of weak tangles dislocations indicating transformation of planar slip to wavy slip at 5% strain.

the grain interior (demarcated using white) at 5% strain and previously at this strain (5%) Taylor lattice observed in ECCI (Fig. 4.2(c) in Chapter 4.2). Alongside, two annealing twins outlined using yellow lines are also noted in Fig. 6.2(b). Taylor lattice is a low energy dislocation structure (LEDS) consisting of organized planar dislocation array, which are observed in fcc metals/alloys. Such LEDS result from the interactions between the dislocations on the primary and secondary slip system and are uniformly distributed on the most highly stressed {111} glide planes (Yvell, 2018).

Kuhlmann-Wilsdorf (1989) suggested that a microstructure containing Taylor lattice alongside dipolar and multipolar dislocation arrays could easily be transformed into dislocation cell walls (*i.e.*, wavy glide) at higher strains. In an agreement to that proposition (Kuhlmann-Wilsdorf, 1989), a dislocation dipole is detected at 2% strain under a strong $\mathrm{g}_{02\bar{2}}$ reflection, as presented in Fig. 6.2(c). The corresponding WBDF micrograph in the $\mathrm{g}-3\mathrm{g}$ condition is presented in the right half of Fig. 6.2 (c) also establishes the dominating edge character of the dipole (β' ~ 50°). Such dislocation dipole/multipole configurations usually occur from juxtaposition of edge dislocations due to cross-slip and that they are known to align along the primary slip direction (Jackson, 1983). These dipoles are known to be a consequence of successive cross-slip events and that they represent an energetically stable configuration (Jackson, 1983). These features are rarely observed in high-Mn steels and their role in plasticity is unclear (Kim *et al.*,2019). Alongside, the BF micrograph presented in Fig. 6.2(d) also indicates the transformation of planar slip to wavy slip and development of weakly tangled dislocations at 5% strain.

It is worth mentioning that slip planarity is favoured not by a low SFE alone, but also influenced by shear modulus, atomic size misfit, solute content, SRO, etc. (Hong & Laird, 1990). The presence of dipole and multipole in the present steel at low plastic strain, as observed in Fig. 6.2(c), can only occur when dislocations in secondary slip systems interact with those in the primary slip system and cross-slip takes place only over a short-range (Kuhlmann-Wilsdorf, 1989; Fujita, 1983). Gerold and Karnthaler (1989) further indicated that pronounced planar slip could also be observed in quite high SFE alloys and they suggested that well-developed SRO and/or short-range clustering (SRC) could also promote planar slip through the ‘glide plane softening’ effect. The sub-regular solution model of SFE in high-Mn steels predicts SFE of the present steel is (γ) ~ 25 mJ/m^2 (Saeed-Akbari *et al.*, 2009), while the experimental estimation of the SFE of the present steel during straining is ~ 60 mJ/m^2

(Chapter 5.1.5) and this mismatch could be attributed to the debated postulate of elevation of SFE due to grain refinement (Volosevich *et al.*, 1976; Lee *et al.*, 2000; Chen *et al.*, 2021) – though the exact reasons are still unclear, effect of SFE on the microstructure evolution will be described subsequently.

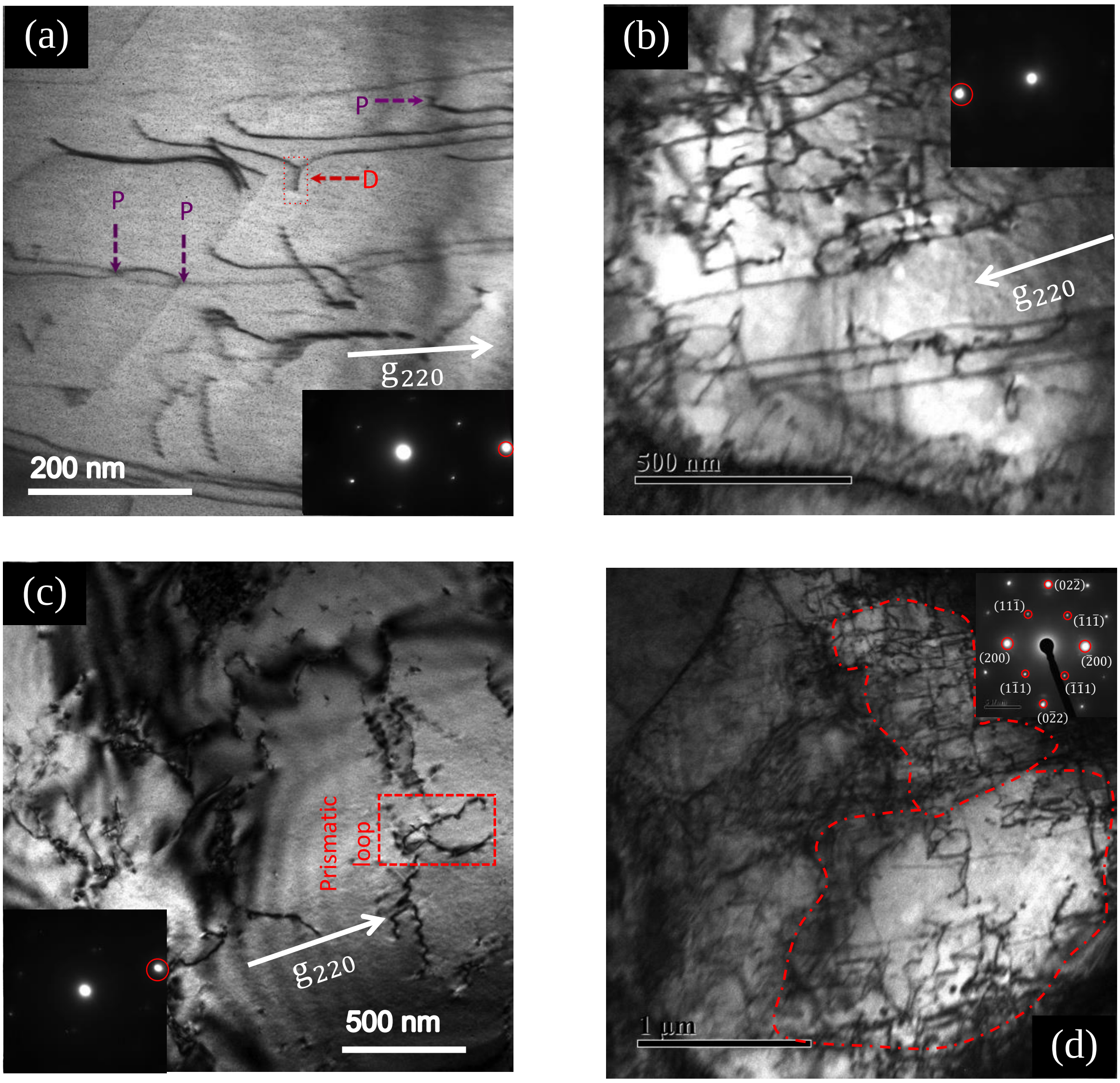

Fig. 6.3: BF TEM micrographs of differently strained specimen showing: along $B \approx [1\bar{1}0]$ for ((a) to (c)). (a) pinning of $\frac{a}{2}\langle 110 \rangle$ dislocations and dipole formation at 2% (b) planar glide and Taylor lattice formation at 5% (c) oscillating contrast of an incomplete prismatic loop at 5% strain (d) extension of Taylor lattice to whole grain at 5% strain imaged along $B \approx [011]$ and delineated using red.

A further set of BF microstructure is presented in Fig. 6.3, revealing that dislocations are nearly screw type at the lowest 2% strain, while most of them are also pinned, and indicated by dashed purple arrows and the letter P. Further, these dislocations are seen to trail a dipole loop, denoted by a dashed red arrow labeled D and that these dipoles play a very crucial role in the plastic accommodation mode of this steel. At 5% strain, a prominent Taylor lattice develops and presented in Fig. 6.3(b) which was also observed in Fig 4.2(c) (Chapter 4.2). Taylor lattices are LEDS, which are generally formed at early strains as a result of pronounced planar glide on highly stressed glide planes without requiring any systematic lattice rotations (Kuhlmann-Wilsdorf, 1989). The contribution of LEDS to strain hardening is still uncertain due to their scarce occurrences in high-Mn steels (Gutierrez & Raabe, 2012).

Thus, it is evident that the presence of nearly screw type pinned dislocations in Fig. 6.3(a) activates cross-slip in the studied steel at a quite low strain, which in turn produces prismatic loops, but not shear loops (Gregori & Veyssiere, 2002b). A high magnification BF image presented in Fig. 6.3(c) reveals the nucleation stage of one such incomplete prismatic loop at 5% strain showing oscillating contrast of a sharply inclined dislocation due to dynamical effects (Fultz & Howe, 2007). The low magnification $B \approx [011]$ multi-beam image in Fig. 6.3(d) demonstrates the proliferation of Taylor lattices to the entire grain at 5% strain.

6.1.2 Proliferation of wavy glide and scarcity of deformation twins at intermediate strains

At a relatively higher strain of 10%, new interesting features develop in the microstructure and they are presented through a couple of BF micrographs. Prismatic loops in Fig. 6.3(c) in the 5% strained specimen were found to attain an L– or V–shape after relaxing towards edge orientation (Veyssiere & Gregori, 2002). In agreement, a moderate population of such loops surrounded by forest dislocations is observed at 10% strain (Fig. 6.4(a)). Fig. 6.4(b) shows alongside several austenite grains at 10% strain containing weakly developed dislocation cell substructures, *i.e*. transformation of planar to wavy slip. Besides, a high magnification multi beam $B \approx [011]$ image of weak dislocation cells at 10% strain is presented in Fig. 6.4(c) and at this strain (10%), which are in excellent agreement with the weak dislocation cells in Fig 4.2(d) of (Chapter 4.2) – observed using ECCI.

Nevertheless, as an opposing observation, no sign of deformation twinning was observed until fracture (Idrissi *et al*., 2010; Mahato *et al*., 2015). Therefore, it is postulated that twinning is suppressed in the steel, while the plasticity is mediated by concomitant dislocation substructures produced through successive cross-slip. In an attempt to clarify the reason for twinning suppression in the steel, we present a two-beam BF micrograph in Fig. 6.4(d), which was obtained with g_{200} along $B \approx [011]$ from a grain of the 10% strained specimen containing relatively low density of defects. It nicely illustrates the reason for twin suppression in a single frame. Two distinct loop strings are again observed within the green regions (Fig. 6.4(d)), whose mobile segments bow under the action of the local stress field (the bowing direction

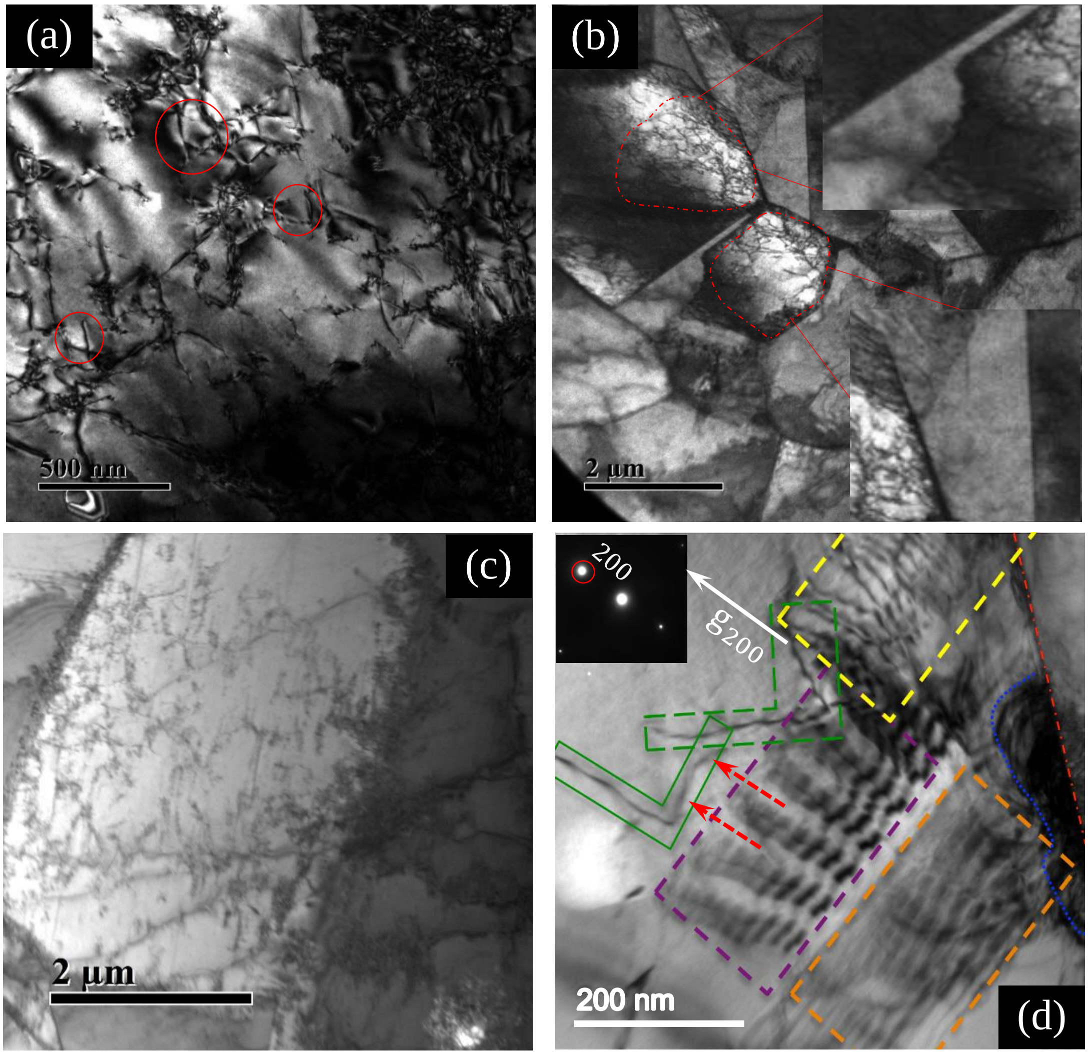

Fig. 6.4: BF micrographs of the specimen at 10% strain showing: (a) prismatic loops surrounded by forest dislocations imaged along $B \approx [1\bar{1}0]$. (b) weak dislocation cells at 10% strain at low magnification are delineated using red (c) high magnification image of weak dislocation cells in $B \approx [011]$ at 10% strain (d) a two-beam condition showing the nucleation and suppression of twinning at 10% strain.

indicated by a pair of red dashed arrows), which is in agreement with the WBDF micrograph in Fig. 6.2(a). Other regions delineated using different colors reveal important observations, which are now discussed. The grain boundary shown using a long dashed red line emits perfect dislocations, which are piled up on the primary slip plane (yellow region). Alongside, a region of high dislocation density in the form of dislocation forest/tangles (delineated by the blue line) is also discernible in Fig. 6.4(d).

Interestingly, the dislocation proliferations delineated by blue and yellow lines in Fig. 6.4(d) have different implications on the microstructure evolution of the steel. For instance, twin nucleation is observed within the purple region, through overlapping SFs, revealing periodic contrast of the Shockley twinning partials, as reported recently (Kubin & Kratochvil, 2000; Mahato *et al*., 2015; Mahato *et al*., 2017). SFs in this steel remained uncharacteristically absent, otherwise. Further, the dislocations piled up within the yellow region are expected to be perfect, since they do not reveal any fringe contrast, unlike the dislocations within the twinned region. Therefore, it is justifiable that the stress field associated with this sporadic pile-up (within yellow region) provides the nucleation stress for the fitful occurrence of twinning in Fig. 6.4(d) (De Cooman *et al*., 2018). On the other hand, the region demarcated by blue line, owing to its high local dislocation density would also possess a high local stress field, ruptures the regular arrangement of SFs within the orange outlined region. Consequently, any twinning opportunity is terminated. It is recently reported that presence of any dislocation stress field in the matrix is not conducive for observing twinning (Shyamal *et al*., 2021). In other words, this reaffirms the postulate of Boucher and Christian (1972) that presence of dislocation substructure in the matrix would strongly suppress any deformation twinning activity.

The chemical composition of the present steel although suggests it as a high-Mn steel, so that extended SFs serving as twinning precursors should be omnipresent here at early strains (Idrissi *et al*., 2010; Saeed-Akbari *et al*., 2009). Extended SFs were, however, never observed until 5% strain, implicating the absence of suitable twinning precursors. As shown in the multi-beam low magnification overview micrograph in Fig. 6.5(a), a long SF overlapping with few short SFs are discernible at 10% strain and such features are rarely observed in this steel. It is further seen from Fig. 6.5(a) that, compared to 5% strain, the wavy glide becomes enhanced at this strain level, which also indicates pronouncement in dislocation activity at this strain (10%).

Fig. 6.5(b) obtained with g_{200} along $\mathrm{B} \approx [011]$ shows an evidence of a deformation twin nucleation on the $\{111\}$ planes in the vicinity of a pile-up of dislocations. The region in

Fig. 6.5(b) demarcated by dashed yellow rectangle is an overlap of SFs on three successive {111} planes, revealed by the characteristic periodic contrast of the Shockley partials corresponding to $\vec{g}.\vec{b} = \pm\frac{1}{3}$ ($\vec{g}$ and $\vec{b}$ are the active diffraction vector and Burgers vector of the dislocation, respectively). Such overlapping SFs have previously been detected in the instance of nucleation of deformation twins. Such embryos do not manifest the trademark of twinning side spots in SAD, which are commonly observed from twin bundles (Mahato *et al*., 2015; Mahato *et al*., 2017; Kim *et al*., 2017).

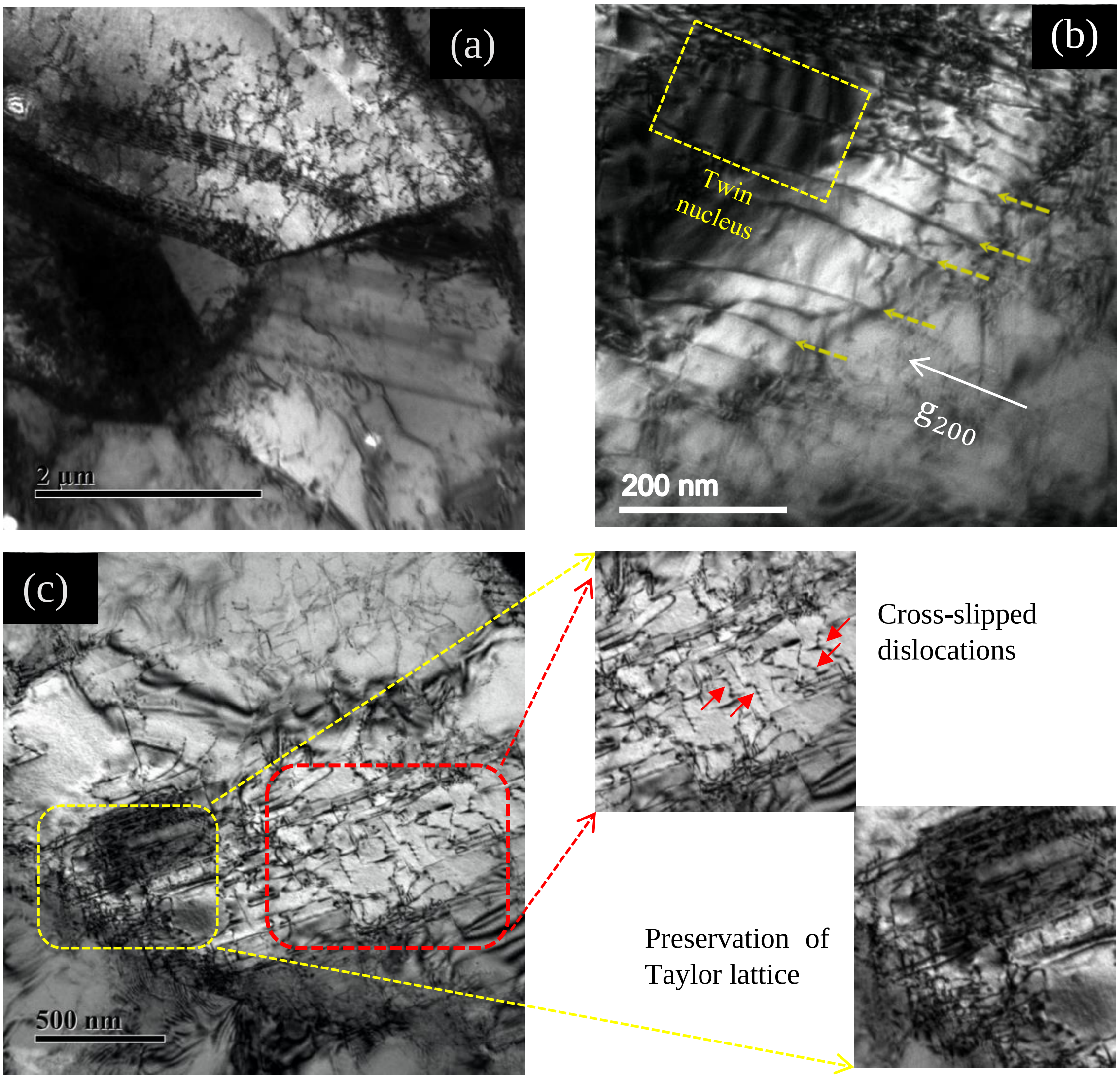

Fig. 6.5: BF TEM micrographs along $B \approx [011]$ at 10% strain, showing: (a) a low magnification multi-beam BF image of long SF overlapping with few others short SFs and surrounded by dislocation substructure. (b) A dislocation pile-up assisted twin nucleus in a two-beam condition. (c) Co-existence of region with short-range cross-slipped dislocations and Taylor lattice preserved region.

Interestingly, dislocations in the pile-up marked by the short yellow arrows in Fig. 6.5(b) are parallel to the dislocations within the adjacent rectangle, while the region in between the former dislocations do not show any SF fringe contrast like their Shockley counterparts within the dashed rectangular region. This can only be explained by considering that both sets (one marked by yellow arrows and another within the rectangular region) of piled up dislocations in Fig. 6.5(b) lie sufficiently close to each other and are in identical diffraction condition. Thus, the dislocations indicated using arrows are perfect dislocations but not Shockley partials, otherwise, they would have also revealed a fringe contrast. Further, those pile-up dislocations in Fig. 6.5(b), showing strong contrast, are nearly parallel to the active diffraction vector, g_{200}. Thus, they are likely to be $\frac{a}{2}[\bar{1}01]$ dislocations having a screw component and piled up on the primary plane – though such pile-up incidences were sporadic and its implications on the strain hardening of the steel will be discussed subsequently.

A noteworthy multi-beam BF micrograph is presented in Fig. 6.5(c), representing the microstructure at 20% strain. In this figure, two distinct regions are delineated using yellow and red colors, and a magnified view is also presented alongside. On one hand, the yellow region corresponds to the Taylor lattice region, i.e. a LEDS region, which were already observed to be formed at early strain of 2% or before (Fig. 6.2(a)). According to Kuhlmann-Wilsdorf (1989), the prevalence of LEDS in fcc metals/alloys is often associated with absence of hardening, as is observed in cyclic deformation. On the other hand, the red region reveals significant numbers of cross-slipped dislocations (some of them are indicated by red arrows). Thus, though the cross-slip in the present fine-grained steel is activated in between 2% strains (Fig. 6.2), the observations in Fig. 6.5(c) indicate that it is restricted only to short-range distances (Jackson, 1983), until intermediate strains.

6.1.3 Dislocation substructure at failure strain

The microstructures of the steel at the failure true strain (~ 50%) are presented in Fig. 6.6. It is revealed from the low magnification overview micrograph of Fig. 6.6(a) that sheet like dislocation cell boundaries showing a diffuse contrast are formed, and that the boundary dislocations are not distinguishable from the surrounding dislocations. Besides, a partially recovered region delineated using a yellow dashed line is also discernible in Fig. 6.6(a), which is presumably responsible for the slightly decreasing SHR observed in stage-D (Fig. 3.1(b)) (Chapter 3.2).

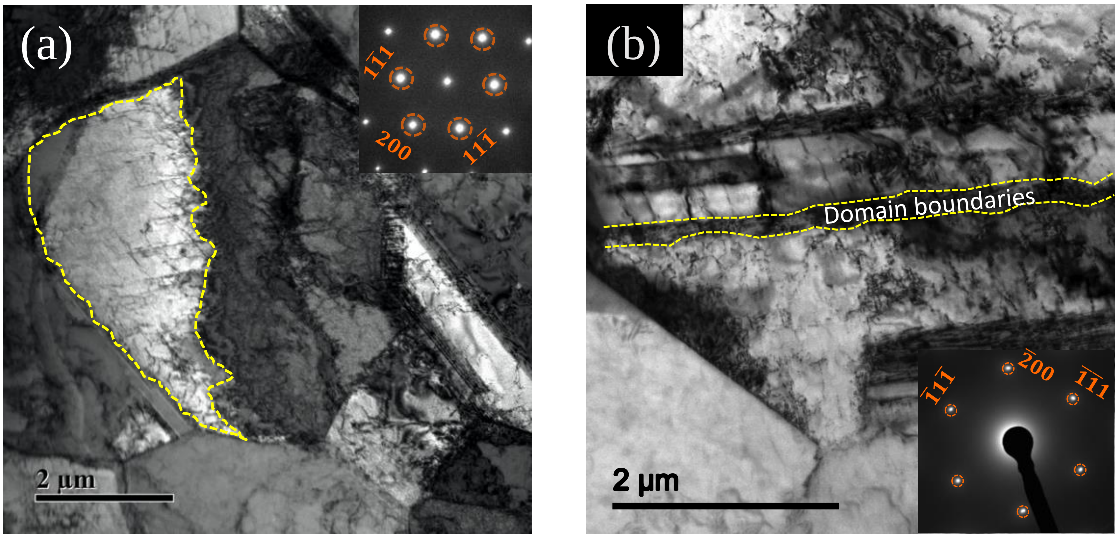

Fig. 6.6: Multi-beam TEM BF micrograph of failed specimen (~ 50% strain) in $B \approx [011]$ showing: (a) a recovered region delineated using yellow line and sheet like dislocation cell boundaries. (b) Domain boundaries (delineated using dashed yellow line) formation due to co-existence of differently oriented Taylor lattices. Inset SAD pattern reveals the absence of twinning side spots.

Another significant microstructural feature of failed specimen presented in Fig. 6.6(b) is densely developed boundaries, wherein, the resolved extra dislocations demark the boundary from the surrounding dislocations. The observed contrast in Fig. 6.6(b) occurs when two adjacent regions containing dislocations are misoriented with each other across the boundary (Kuhlmann-Wilsdorf, 1989). Such boundaries are known as domain boundaries, which are actually coexist regions of differently oriented Taylor lattices (Kuhlmann-Wilsdorf, 1989). A domain boundary is formed when regions of significantly different dislocation arrangements coexist, wherein a changeover between coplanar Burgers vector takes place on the active glide plane (Kuhlmann-Wilsdorf, 1989). Moreover, no twin side spots were observed in the indexed SAD patterns, presented as insets to the BF micrographs of Fig. 6.6.

It is known that Taylor lattices can easily transform into dislocation cells and when the glide takes place on more than one plane (Kuhlmann-Wilsdorf, 1989). Fig. 6.7(a) reveals the copious dislocations debris observed in a specimen that failed at 50% strain, which interestingly possesses a pair of dislocation segments, indicated by the short arrow within the sepia inset, whose SAD pattern is shown in Fig. 6.7 (b). Veyssiere and Gregori indirectly made a conclusion that such L or V-shaped dislocation segments arise from termination of the loop

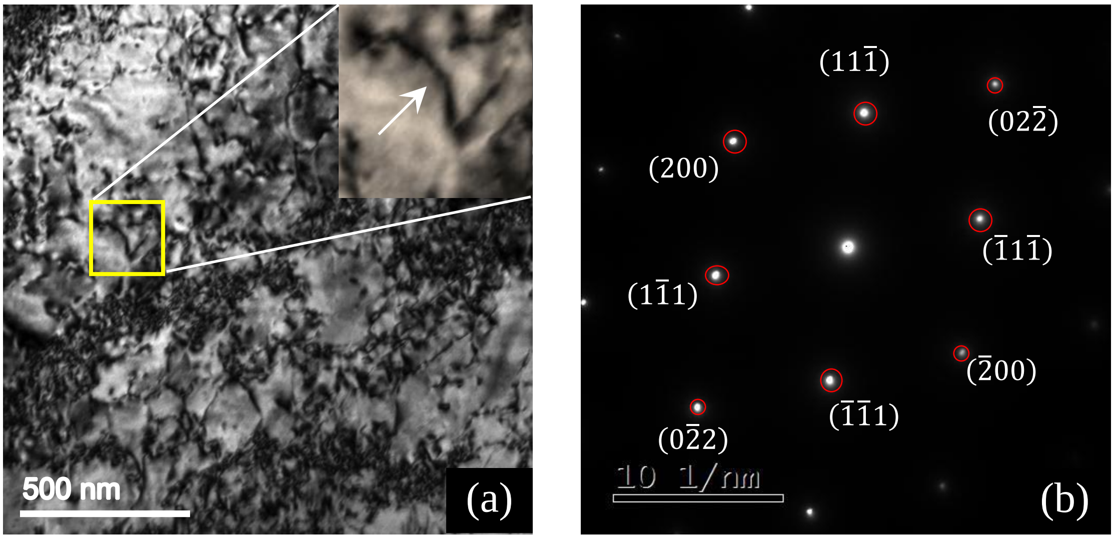

Fig. 6.7: Bright-field TEM micrographs at failure strain ($\sim$ 50%) of the specimen showing: (a) a loop string amongst dislocation debris under multi-beam conditions (b) diffraction condition of (a) in $B \approx [011]$

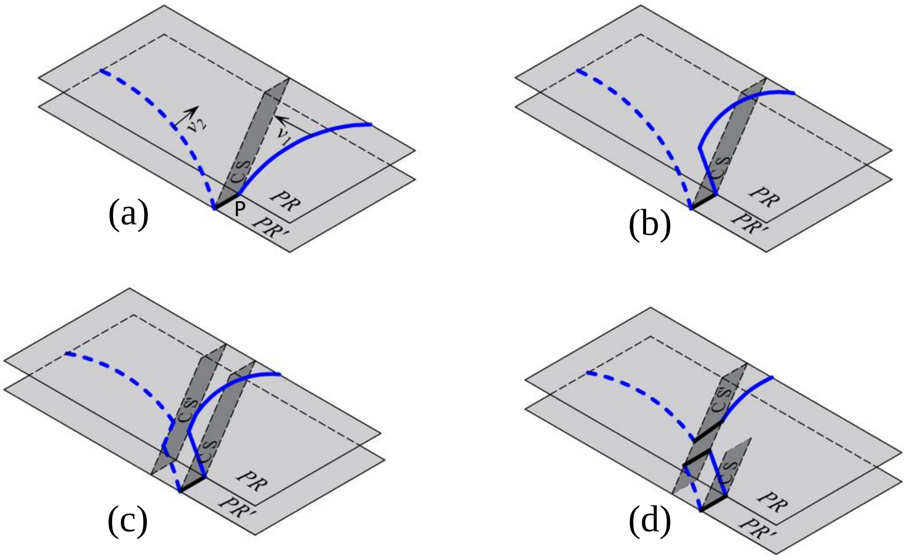

Fig. 6.8: The schematic of loop string formation in Fig. 6 2: (a) two impinging dislocations moving on parallel primary slip planes (PR and PR') with velocities v_1 and v_2 are jogged at $P, v_1 \gg v_2$. The jog (solid black segment) is free to move on the darkly shaded cross-slip plane (CS). (b) The dislocation segment in solid blue trails a hairpin like dipole configuration along the least mobile segment. (c) The two blue segments (solid and dashed) forming the dipole is aligned in the screw direction and cross-slips to the next parallel plane (CS'). (d) The glissile segments thus form the first loop through annihilation and this maneuver can repeat itself to produce several loops in succession.

strings by a closing jog and their subsequent relaxation towards edge orientation (Veyssiere & Gregori, 2002b). Such a configuration of the loop string was first observed in Fig. 6.1 for the studied steel at the onset of deformation, and thus the proposition of Veyssiére and Grègori (2002b) seems tenable in the present study. The whole mechanism of loop string formation in Fig. 6.1 is schematically presented in Fig. 6.8. Kubin and Devincre (1999) further suggested that the configurations of these loop strings remain stable under deformation, as also observed here in Fig. 6.7(a).

6.1.4 Deformation microstructure of a coarse-grained counterpart

The multi-beam TEM BF microstructure of the coarse-grained steel is now presented in Fig. 6.9 for a direct comparison of the microstructure evolving in two different grain-sized specimens. Fig. 6.9(a) shows an early intersecting planar dislocation structure, indicating the onset of Taylor lattice formation at 2% strain, similarly as was observed in the fine-grained specimen (Fig. 6.2(a)). An additional feature of the coarse-grained steel at this (2%) strain is in the presence of a wide SF presented as an inset in Fig. 6.9(a). Such SFs are known to play the role of twinning precursors in high-Mn steels (Idrissi *et al.*, 2010; Mahato *et al.*, 2015; De Cooman *et al.*, 2018). On the other hand, the BF microstructure of the coarse-grained specimen shown in Fig. 6.9(b) reveals profuse twinning at failure strain of ~ 50%, which is also

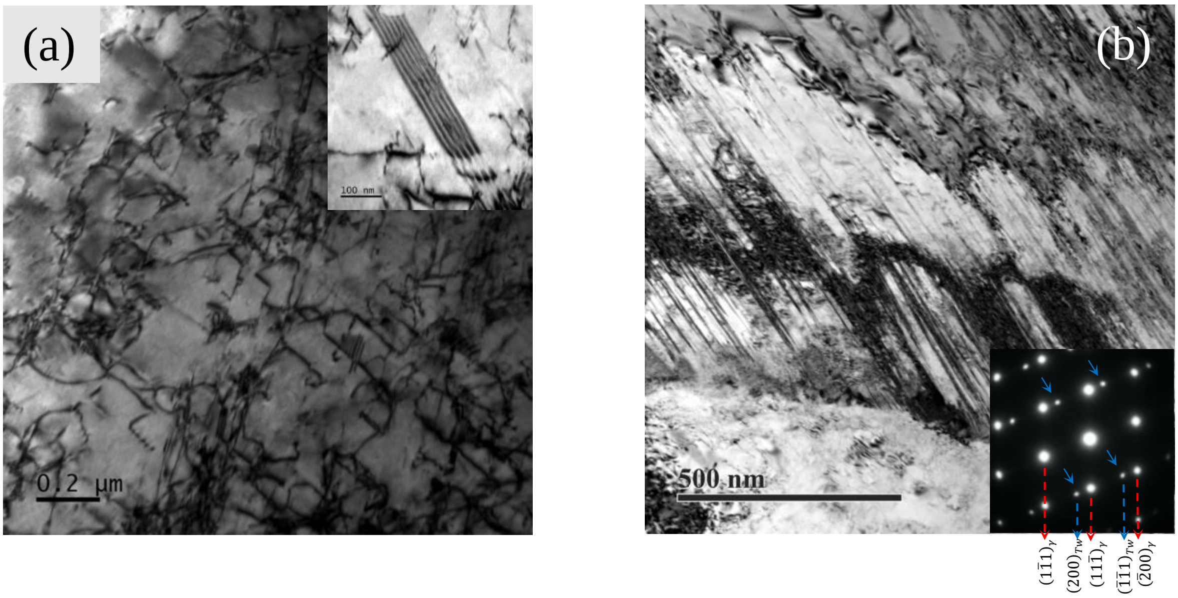

Fig. 6.9: Multi-beam TEM BF micrograph of the coarse grain steel in $B \approx [011]$ showing: (a) intersecting dislocations and the onset of Taylor lattice at 2% strain. The inset shows a long SF at this strain. (b) Fine twin bundles at failure strain ~ 50%. The inset reveals the corresponding SAD pattern with twinning side spots.

confirmed from the presence of twin side spots in the corresponding $B \approx [011]$ SAD pattern inserted in Fig. 6.9(b). Thus, the microstructural features of the coarse-grained steel counterpart are in good agreement with the conventional coarse-grained high-Mn steels revealing profuse twinning under plastic deformation (Idrissi *et al.*, 2010; De Cooman *et al.*, 2018). However, the microstructures in the fine- and coarse-grained steels used in the present study are in strong contrast to each other, while the former revealing near suppression of twinning and the latter revealing profuse twinning – and yet they reveal comparable strain hardening properties – as discussed under Fig. 3.1 of Chapter 3.2.

6.1.5 Effect of grain size on deformation twinning

It is known that deformation twins grow under locally defined stresses from defect-assisted atomic scale twin nuclei, which leads to different stress for twin nucleation and growth. The twinning tendency in fcc metals/alloys is interpreted using various empirical equations involving the critical twinning stress $(\tau_c)_{twin}$, which directly relate it to SFE of the concerned system. The literature reviewed in Chapter 1.4 indicated that grain refinement causes suppress the twinning tendency in high-Mn steels (Ueji *et al.*, 2008; De Cooman *et al.*, 2018). The suppression of twinning was interpreted based on the critical twinning stress, $(\tau_c)_{twin}$ – though such proposition remained ambiguous due to some conflicting reports. Phiu-on and Bleck (2008) indicated that the grain size does not affect the twinning stress, while Mohammed *et al.* (2007) reckons that it is increased by a reduction in the grain size. As also observed in the present type steel, twinning is generally enhanced in coarser austenite grains (De Cooman *et al.*, 2018).

The suppression of twinning in the steel used in the present dissertation could be qualitatively interpreted on the findings of Volosevich *et al.* (1976), Takaki *et al.* (1993) and Lee and Choi (2000) – discussing the influence of austenite grain size on SFE of Fe-Mn alloys. Volosevich *et al.* (1976) predict that when grain size is refined from 35 µm to 5 µm, an increase in SFE from 14 to 40 mJ/m^2 should occur in an Fe-17.8Mn-0.47C alloy, while Takaki *et al.* (1993) expects the increment to be from 20 to 25 mJ/m^2 in an Fe-26Mn alloy. In a recent study, Chen *et al.* (2021), estimated that their high-Mn steel reveals an SFE increase from 26 to 34 mJ/m^2, corresponding to a grain size refinement of 47 to 11 µm. However, their estimation does not consider the effect of deformation on SFE, while Mahato *et al.* (2015) estimated that SFE of high-Mn steel can increase from 18 to 40 mJ/m^2 with increasing deformation. This increment was attributed solely to dislocation-SF interaction, but not to any grain refinement (Mahato *et al.*, 2015).

Nevertheless, one obvious explanation based on the current theoretical and experimental understanding (Lee and Choi, 2000; Chen *et al.*, 2021) could be that the SFE in high-Mn steels is increased due to grain size refinement. Thus, when the grain size is refined, the higher back stresses on dislocations within the smaller grain size elevates apparent SFE of the steel and twinning is known to be suppressed under high SFE conditions. Therefore, the evaluation of $(\tau_c)_{twin}$ values should also involve an explicit grain size dependent parameter – at least for high Mn steels, while such expressions are still lacking in the literature.

6.1.6 The classical paradigm of twinning and the role of dislocation pile-up

In this section, we try to decipher the observed suppression of twinning from a classical paradigm. In this theory, the twinning tendency in fcc metals/alloys is interpreted using various empirical equations involving the critical twinning stress $(\tau_c)_{twin}$, although unambiguous experimental validation of critical twinning stress is difficult (De Cooman *et al.*, 2018). Nevertheless, De Cooman *et al.* (2018) discussed the implications of the various expressions for $(\tau_c)_{twin}$ and emphasized about three models that were also adopted in the present study, namely, the models proposed by Steinmetz *et al.* (2013) (Eq. 6.1), Suzuki and Barrett (1958) (Eq. 6.2), and Byun (2003) (Eq. 6.3):

$$(\tau_c)_{twin} = \frac{\gamma}{3b_p} + \frac{3Gb_p}{L_0} \tag{6.1}$$

$$(\tau_c)_{twin} = \frac{\gamma}{2b_p} + \frac{Gb_p}{L_0} \tag{6.2}$$

$$(\tau_c)_{twin} = \frac{2\gamma}{b_p} + \frac{(2-3\nu)}{4\pi(1-\nu)} \times \frac{Gb_p}{d} \tag{6.3}$$

The first two models closely relate to the experimentally determined values (De Cooman *et al.*, 2018), while the third model predicts the highest possible critical twinning stress. In Eqs. (6.1) – (6.3), b_p = 0.147 nm is the magnitude of the Burgers vector of Shockley twinning partials and γ is SFE ~ 60 mJ/m^2, calculated in Chapter 5.1.5. In Eqs. (6.1) – (6.3), it was assumed that L_0, the average length of the twinning source is ~ 200 nm (*i.e.*, ~ 1356 b_p) (Mahato *et al.*, 2015; Mahato *et al.*, 2017), the shear modulus of the steel G = 72 GPa, and Poisson's ratio ν = 0.24 (2014). It is worth mentioning that for twinning to occur according to

Byun's model (2003), the second term in Eq. (6.3) should vanish – only if the Shockley partials are 'infinitely' separated ($d \rightarrow \infty$), thereby simplifying Eq. (6.3) to $(\tau_c)_{twin} = \frac{2\gamma}{b_p}$. Repeating these calculations for the present steel, the $(\tau_c)_{twin}$ values turn out to be ~ 294 MPa, 257 MPa and 816 MPa (as $d \rightarrow \infty$), according to Eqs. (6.1) – (6.3), respectively. These assumed parameters are summarized in Table 6.1.

The outcomes of Eqs. (6.1) – (6.3) suggest that except for the value given by Byun's model (2003), the calculated $(\tau_c)_{twin}$ values are not high and could easily be overcome by the resolved shear stress even at small strains. Therefore, in spite of the high SFE of ~60 mJ/m^2 (Chapter 5.1.5), one might expect twinning to readily appear in the present fine-grained steel, similarly as observed in its coarse-grained counterpart Fig. 6.9(b), which was, however, not the case. In this context, it's noteworthy to mention that Gutierrez-Urrutia and Raabe (2012) also observed that a coarse-grained (~ 50 µm) Fe-30.5Mn-2.1Al-1.2C high-Mn steel with a SFE of ~ 63 mJ/m^2 can reveal a high density of deformation twins under tensile straining. Thus, it is quite reasonable to infer that the suppression of twinning in the present steel should not be attributed to its high SFE alone. It has been recently reported by some of the present authors that the classical twinning routes are suppressed when the SFE is moderately high, but not high enough to completely suppress the twinning (Shyamal *et al.*, 2021), and a non-classical hybrid twinning mechanism is activated. Although, no such hybrid twin mechanism could be observed here.

Table 6.1: Critical twinning stress values of the steel according to different models.

Shear modulus, G (GPa)	Burgers vector of Shockley partials, b_p(nm)	SFE, γ (mJ/m^2)	Critical twinning stress, $(\tau_c)_{twin}$ (MPa)	Twinning stress models
72	0.147	60	294	Steinmetz *et al.* (2013)
			257	Suzuki & Barrett (1958)
			816	Byun (2003)

Additionally, it should be mentioned that De Cooman *et al.* (2018) believe besides low SFE, a suitable dislocation pile-up in the matrix is also a prerequisite that provides the local stress concentration to observe twinning through sequential overlap of wide SFs on successive {111} planes. Interestingly, while pile-ups are known to be ubiquitous in such steels (Mahato *et al.*, 2015; De Cooman *et al.*, 2018), no such long pile-up of dislocations could be observed in the present steel in any of the TEM foils investigated. The only exception was a sporadic tiny incidence in Fig. 6.5(b), which was also accompanied by a twin nucleus in its vicinity. It was observed from TEM studies that the dominance of cross-slip mediated dislocation plasticity in this steel and the associated stress field of the dislocations effectively terminate the possibility of overlapping of the SFs to create a twin nucleus. Therefore, it is most likely that the suppression of twinning in this steel is related to prevalence of various dislocation substructures in the matrix, and this hypothesis is tested further in section 6.1.9

6.1.7 The role of cross-slip in delayed dynamic recovery

It is known that cross-slip and dynamic recovery are two strongly interrelated phenomenon and they both affect the strain hardening response of the concerned material. The dislocation substructure and dearth of twins and extended SFs in the deformed steel, as presented in the TEM micrographs described in previous sections is consistent with the high SFE of the steel, ~60 mJ/m^2 (Chapter 5.1.5). Such a situation is known to favor cross-slip that is usually activated at large strains. Formation of the di/multi-polar dislocation arrays and the wavy slip, however, indicate that cross-slip was activated quite early in the present steel (2–5% strains, see Fig. 6.2). In such conditions, cross-slip induced dynamic recovery is expected in strain hardening stage C and consequently, SHR should decrease in this stage (Humphreys & Hatherly, 2004). However, any pronounced softening did not occur even at 30% strain (Fig. 3.1(b) of Chapter 3.2), despite cross-slip being activated at the onset of deformation (Fig. 3.1(b) of Chapter 3.2).

In an attempt to explain this fallacy, it is perceived that any drop in SHR in stage C is essentially due to dynamic recovery, wherein, an important role is played by annihilation of dislocations with opposite Burgers vectors (Rollett & Kocks, 1993). The annihilation of dislocations does not seem very relevant in stage C for the present steel (Fig. 6.5(c)) and therefore a possible explanation in line with the finding of Jackson (1983) is that any cross-slip initiated at low strains has to be confined only over short-range distances until intermediate strains. The observation in Fig. 6.5(c) indeed lends support to this conjecture. Thus, such occurrences of cross-slip over short-range would delay dynamic recovery at intermediate strains and in synergy with the presence of LEDS delay associated softening in stage C. In such instances, cross-slip, instead of decreasing the SHR, upholds it at ~ $\frac{G}{35}$, *i.e.*, maintains a stable hardening of the steel until 30% strain. On the other hand, at even higher strains (> 30%), as and when the region of cross-slip extends within the grain interior, the probability of dynamic recovery increases due availability of more numbers of newly created dislocations. Such a situation would lead to observing recovered region(s) (Fig. 6.6) and associated drop of SHR in stage D (Fig. 3.1(b) of Chapter 3.2).

6.1.8 Effect of equilibrium stacking fault width

The presence of wide SFs within the deformation microstructures may also hinder the dislocation glide, and therefore the precise understanding of the active deformation mechanisms requires the determination of the width of SFs. It is well known that in absence of any external stress the width of a SF depends on the energy of the faulted region itself and the repelling forces of the two Shockley partials, which is same as the SFE of the material under consideration. However, the presence of any external stress strongly influences the formation a SF, and it should directly affect the width of the SF (Byun, 2003). Byun (2003) has suggested the dependence of the SF width (w_{sf}) on the external shear stress (τ), according to the following equation:

$$w_{sf} = \frac{Gb_p^2}{\pi(2\gamma - \tau b_p|sin\,\theta_2 - sin\,\theta_1|)}\left[cos\,\theta_1\,cos\,\theta_2 + \frac{sin\,\theta_1\,sin\,\theta_2}{(1-\nu)}\right] \qquad (6.4)$$

where, θ_1 and θ_2 indicates the angles made by the Burgers vectors of the leading and trailing partial dislocations with the unit vector of the perfect dislocation line, presumed as $-30°$ and $+30°$, respectively.

Therefore, Eq. (6.4) predicts that in the present steel only narrow SF ribbons will be formed, which might not provide any effective obstacle to the dislocation glide. A multi-beam BF TEM micrograph along $B \approx [011]$ at 5% strain is presented in Fig. 6.10(b), clearly shows that only fine sporadic SF ribbons surrounded by dislocations are evolved in the microstructure, although their widths are somewhat larger than the predicted one – attributable to the accuracy limits of several parameters used in Eq. (6.4), as well to any statistical variation of the width seen in TEM.

It is unanimously accepted that twinning in fcc crystals is observed, when the SFs overlap on successive {111} close packed planes. Interestingly, Talonen and Hänninen (2007) proposed the dependence of equilibrium twin width (w_{tw}) on the number of overlapping SFs

(N), which also involves the SFE of the austenite and is governed by the following equation:

$$w_{tw} = \frac{NGb_p^2}{4\pi\sigma^{\gamma/\varepsilon}}\left[\frac{3}{4} - \frac{1}{4(1-\nu)}\right] \tag{6.5}$$

where, $\sigma^{\gamma/\varepsilon}$ is the energy of the austenite/ε-martensite interface, which is a poorly defined parameter and is often approximated as $\gamma = 2\sigma^{\gamma/\varepsilon}$ with reported values for Fe-Mn alloys lying between 5–30 mJ/m^2 (Cotes *et al*., 2004). In the present study, the calculation of Talonen and Hänninen (2007) was repeated assuming the SFE of ~ 60 mJ/m^2 (Chapter 5.1.5). The results

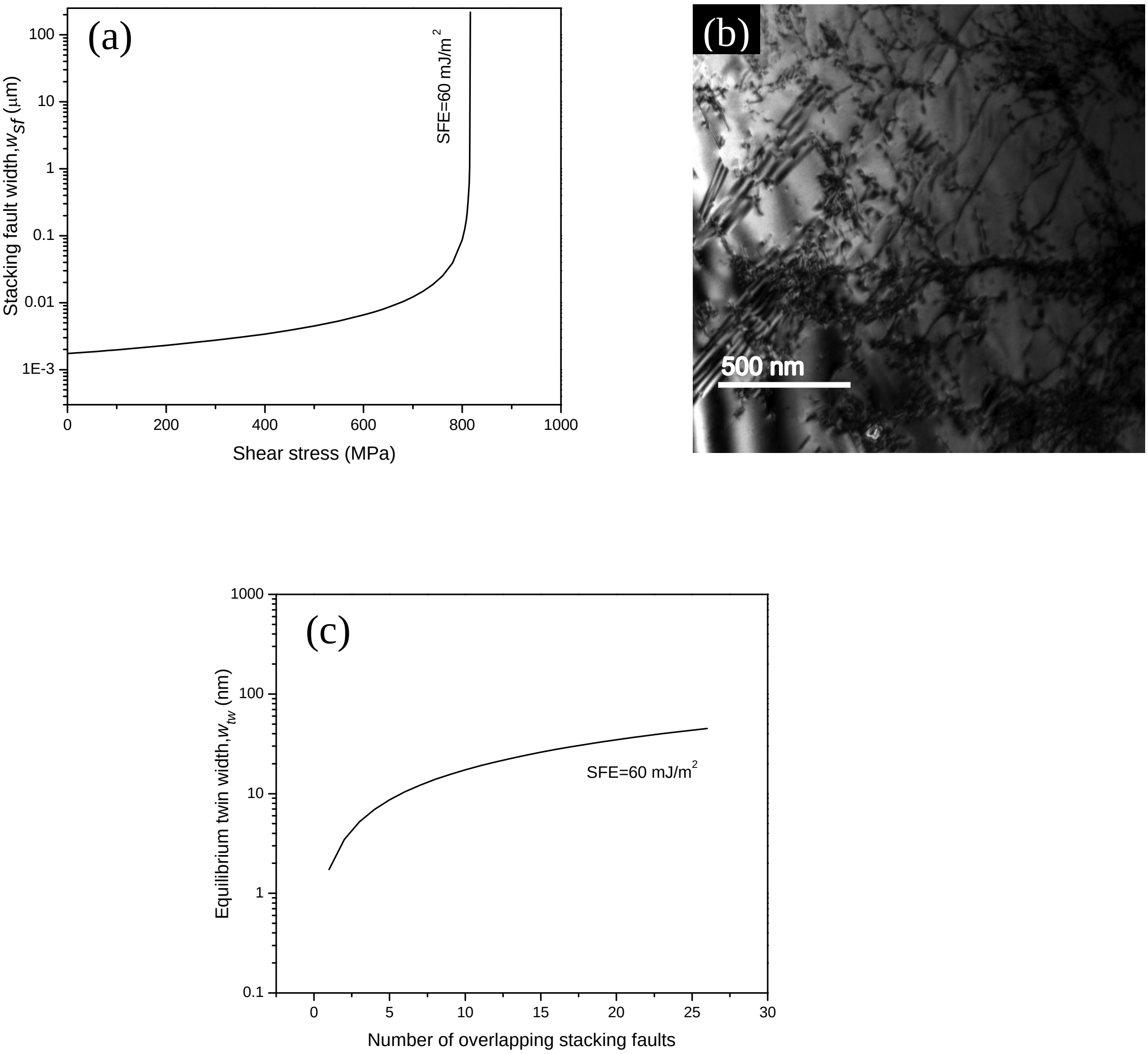

Fig. 6.10: (a) Variation of SF width with shear stress. (b) The multi-beam BF TEM micrographs along $B \approx [011]$ showing fine stacking fault ribbons at 5% strain. (c) Variation of overlapping SFs width with the number of overlapping SFs.

are plotted in Fig. 6.10(c). It can easily be inferred from the figure that the conditions in the present steel are too restrictive for deformation twinning, with w_{tw} not even reaching 100 nm even after overlapping of 25 SFs on successive twin planes. Interestingly, it is worth mentioning that it will be a deception to attribute this restriction to high SFE, since it was noted in the preceding discussion that even a high SFE ~ 60 mJ/m^2 could also lead to a low twinning stress, though no abundant twinning could be observed in reality. Thus, it is reasonable to conclude that since the SFE in the present steel cannot directly contribute towards the prevalence of twinning, the high SFE value of ~ 60 mJ/m^2 offers a favorable path to the occurrence of dislocation cross-slip at early strains (Section 6.1.1). Subsequently, dynamic recovery in the steel is delayed until stage C due to restriction of cross-slip to short-range distances, as already expressed in section 6.1.7.

6.1.9 Effect of local dislocation substructure

It is to be noted that the interplay between dislocation motion and twinning is still an open question, and the general consensus is that twinning occurs when the deformation conditions are such that it cannot completely accommodate the imposed plastic strain rate through dislocation slip and thereby calling for additional mechanisms. According to Mahajan (1969), Boucher and Christian (1972), the onset of twinning is a complex phenomenon that cannot simply be described by a critical global stress value, and that the dislocation density and structure play major roles in determining the twinning occurrences. They further hypothesized that the dislocation distribution was far more important to suppress twinning, and it could be suppressed due to presence of a homogenous dislocation distribution (Mahajan, 1969; Boucher and Christian, 1972). Combining their postulate with the complex dislocation substructure observed in the present study, it is likely that grain refinement terminates the twinning opportunity in this steel through hindering the overlap of SF pair, due to the presence of various dislocation substructure.

To strengthen this argument, the nucleation and growth of a twin lamella at 10% strain are distinctly observed in the two-beam BF micrograph of relatively low dislocation containing region displayed in Fig. 6.11(a), obtained with secondary g_{200} beam in $B \approx [011]$ primary beam direction. The characteristic periodic contrast of the $\frac{a}{6}\langle 121\rangle$ Shockley twinning partials in the nucleating stages, corresponding to $\vec{\mathrm{g}}.\vec{b} = \pm\frac{1}{3}$ is clearly identifiable in Fig. 6.11(a). The existence of extrinsic-intrinsic SF pair in the twin lamella of Fig. 6.11(a) was determined in

Fig. 6.11(b) on the basis of the contrast of SF outer fringe under axial DF conditions. A pair of extrinsic and intrinsic SFs, labelled respectively as ESF and ISF, is identified with g_{200} axial DF in Fig. 6.11(b). The g_{200} diffraction vector in Fig. 6.11(b) points away from the bright and dark outer fringes of the respective SFs, representing a set of ESF and ISF; indicated using a pair of yellow arrows. Thus, it is clearly evident that any probable occurrence of twinning in the studied steel is also realized through overlapping of extrinsic-intrinsic SF pairs, as happens in other high-Mn steels (Mahato *et al.*, 2015; Mahato *et al.*, 2015; Kim *et al.*, 2017) although such circumstances were rather infrequent in the present deformation condition. It is therefore imperative from the present TEM studies that seldom occurrence of twinning in the present steel, as observed in Fig. 6.5(b) is restricted to only regions devoid of homogenous dislocation substructure, where the growth of twin can sustain after any nucleation (Fig. 6.11). Thus, the overall twin deficiency is collectively attributed to absence of suitable dislocation pile-up that had to provide a local stress concentration, while at the same time, the cross-slip lead dislocation substructures produced in the matrix offers a preventive environment for twinning. In hindsight, dislocation mediated plasticity in a fine-grained high-Mn steel predominates under a twin destitute condition and the strain hardening response observed is quite comparable

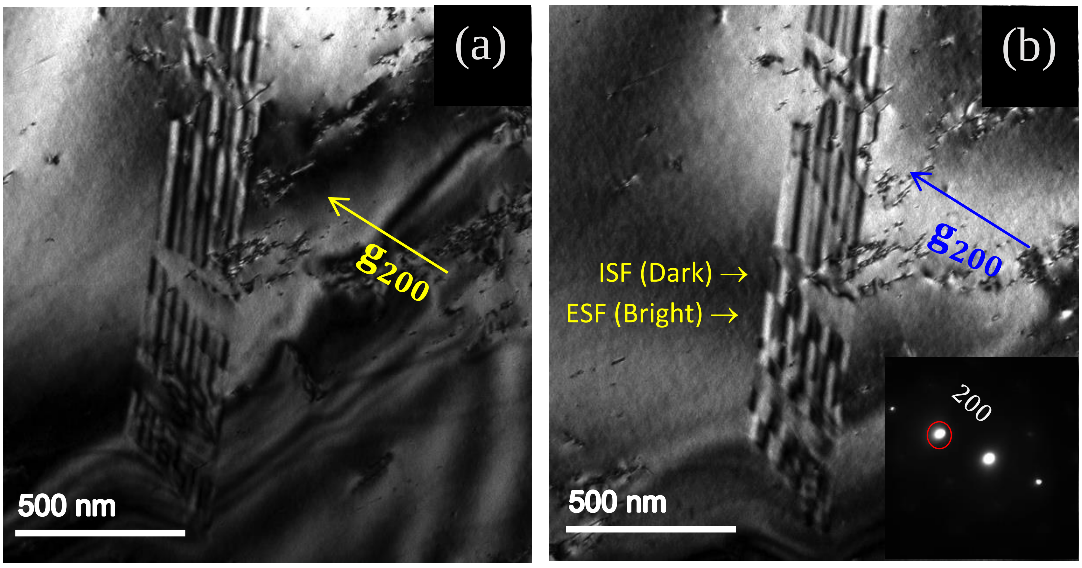

Fig. 6.11: TEM micrographs at 10% strain along $B \approx [011]$ showing: (a) two-beam BF micrograph showing the characteristic periodic contrast of the $\frac{a}{6}\langle 121\rangle$ Shockley twinning partials indicating nucleation and growth of a rare twin lamella in a region devoid of dislocation substructure. (b) Axial DF of (a) showing a pair of extrinsic and intrinsic SFs in the twin lamella.

to that manifested by a coarse-grained counterpart containing profuse deformation twinning (Fig. 3.1(a) of Chapter 3.2).

6.1.10 Correlations between X-ray line profile analysis and transmission electron microscopy investigations

The microstructural parameters estimated using XLPA in Table 5.1 and described through Chapter 5.1.1 – 5.1.5 are further introspected using TEM investigations of the differently deformed specimens and discussed. Fig.6.12 demonstrates a set of TEM BF micrographs acquired along $[110]$ zone axis, revealing various aspects of the deformed microstructures at each terminal strain. Fig. 6.12(a) obtained with g_{220} depicts the activation of multiple slip at 2%, occurring through mutually interacting gliding dislocations, while some of them are pinned and further that some of those dislocations are seen to trail a dipole loop, which on one hand, reaffirms the findings of XLPA in Table 5.1 that the dipole character/strength of dislocations are very prominent at early strains (2%). On the other hand, wavy glide could also be identified in Fig. 6.12(a), which is explained by the fact that glide mode of dislocations (whether planar or wavy) is determined by SFE of the concerned alloy system and that a high SFE usually promotes wavy glide and subsequent cross-slip of dislocations in fcc metals and/or alloys (Smallman & Ngan, 2007). At 5% strain, it is revealed from Fig. 6.12(b) that wavy glide becomes more prominent, and that cross-slip is a major deformation mode of the steel at this strain level.

As the strain is further increased to ~ 10%, regions of very high dislocation densities in the form of tangles and weak dislocation cells are observed in Fig. 6.12(c). The development of forest dislocations and dislocation cells at low strains is quite remarkable in Fe-Mn-Al-C alloys for that these alloys primarily deform by planar slip at low strains (De Cooman *et al.*, 2018). The appearance of dislocation cell at low strains (Fig. 6.12(c)) therefore is to be explained through the occurrence of multiple slip and wavy glide observed in Figs. 6.12(a) and (b), which in turn would facilitate cross-slip of dislocations at such strains. It is reported that dislocations before cross-slipping, should rearrange themselves into cell walls to reduce their stress fields (Smallman & Ngan, 2007). However, since cross-slip is related to internal stress of the material, it might also occur without any rearrangement of dislocations into cell walls. Nevertheless, cross-slip is likely to be responsible for the microstructure observed at 10% strain (Fig. 6.12(c)). This is also supported by the XLPA findings in Table 5.1 from the slowly increasing strain dependent R_e values that signify the phenomenon of stress relaxation of dislocations with increasing strain (Table 5.1 and Chapter 5.1.4).

Interconnected dislocation cells become a quite prominent feature at failure strain (~ 50%), and presented in Fig. 6.12(d). Alongside, dislocation free clear regions are also discernible in Fig. 6.12(d), which is essentially a consequence of dynamic recovery of dislocations occurring at high strains before fracture. In other words, Fig. 6.12(d) also reaffirms the apparent contrasting XLPA finding that M ~ 2.1 in Table 5.1 for the fractured specimen indeed represents weakening of dislocations' dipole strength at large strains, while a stronger

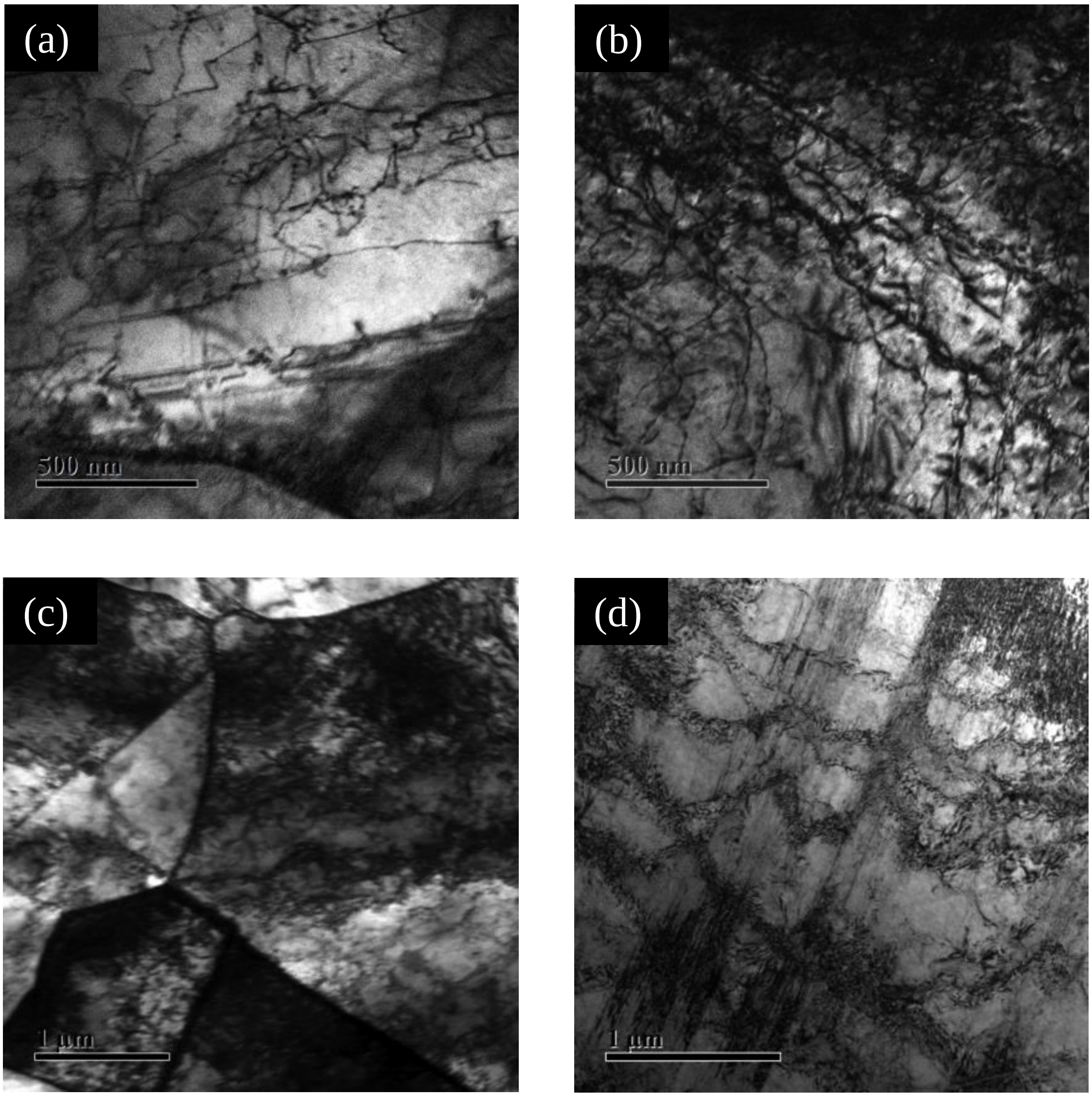

Fig. 6.12: Bright-field TEM micrographs along $B \approx [110]$ showing: (a) activation of multiple slip , pinning of dislocations and dipole loop formation at 2% strain (b) wavy glide of dislocation at 5% strain (c) forest dislocations and weak dislocation cell walls at 10% strain (d) interconnected dislocation cells and dislocations free recovered regions at failure strain (~ 50%).

character is otherwise expected at such strains for fcc metals/alloys (Ungar *et al.*, 2017). Besides, the presence of recovered region in Fig. 6.12(d) also justifies the marginal increase in R_e values observed at this strain (~ 50%) and discussed in Chapter 5.1.4, since it is well known that in presence of dynamic recovery, the deformed austenite undergoes significant stress relaxation (Pietrzyk *et al.*, 2015). In such instances, the correlation among the dislocations are expected to decrease and reflected through an increase in R_e values.

References

Bouaziz, O., Allain, S., Scott, C. P., Cugy, P. & Barbier, D. (2011) *Curr. Opinion Solid State Mater. Sci.* **15**, 141-168.

Boucher, N. A. & Christian, J. W. (1972) *Acta Metall.* **20**, 581-591.

Byun, T. S. (2003) *Acta Mater.* **51**, 3063-3071.

Caillard, D., Legros, M. & Couret, A. (2013) *Philos. Mag.* **93**, 203-221.

Chen, J., Dong, F., Liu, Z., & Wang, G. (2021) *J. Mater. Res. Technol.* **10**, 175-187.

Cockayne, D. J. H., Jenkins, M. L. & Ray, I. L. F. (1971) *Philos. Mag.* **24**, 1383-1392.

Cotes, S., Guillermet, A. F. & Sade, M. (2004) *Metall. Mater. Trans.* A. **35**, 83-91.

Farahani, M. G., Zarei-Hanzaki, A., Abedi, H. R., Kim, J. H., Jaskari, M., Sahu, P. & Karjalainen, L. P. (2020) *Scr. Mater.* **178**, 301-306.

Fujita, H. & Kimura, S. (1983) *J. Phys. Soc. of Japan*, **52**, 157-167.

Fultz, B. & Howe, J. (2007) Transmission Electron Microscopy and Diffractometry of Materials, 3rd Edition, , Springer, Berlin, Heidelberg, New York, ISBN 978-3- 540-73885-5.

Gerold, V. & Karnthaler, H. P. (1989) *Acta Metall.* **37**, 2177-2183.

Gutierrez-Urrutia, I. & Raabe, D. (2012) *Acta Mater.* **60**, 5791-5802.

Hong, S. I. & Laird, C. (1990) *Acta Mater.* **38**, 1581-1594.

Humphreys, F. J. & Hatherly, M. (2004.) in Recrystallization and Related Annealing Phenomena, Elsevier, Oxford.

Jackson, P. J. (1983) *Mater. Sci. Eng.* **57**, 39-47.

Kim, J.-K., Kwon, M.-H. & De Cooman, B. C. (2017) *Acta Mater.* **141**, 444-455.

Kim, S.-D., Park, J. Y., Park, S.-J., Hoon Jang, J., Moon, J., Ha, H.-Y., Lee, C.-H., Kang, J.-Y., Shin, J.- H. & Lee, T.-H. (2019) *Sci. Rep.* **9**, 15171 1-13.

Kubin, L. P. & Devincre, B. (1999) RisøNational Labora- tory, Roskilde, Denmark, 61-83.

Kubin, L. P. & Kratochvíl, J. (2000) *Philos. Mag.* A. **80**, 201-218 .

Kuhlmann-Wilsdorf, D. (1989) *Mater. Sci. & Eng.* A. **113**, 1-41.

Laplanche, G., Kostka, A., Reinhart, C., Hunfeld, J., Eggeler, G. & George, E.P. (2017) *Acta*

Mater **128**, 292303.

Lee, Y.-K. & Choi, C. (2000) *Metall. Mater. Trans*. A. **31**, 355-360.

Mahato, B., Sahu, T., Shee, S. K., Sahu, P., Sawaguchi, T., Kömi, J. & Karjalainen, L. P. (2017) *Acta Mater*. **132**, 264-275.

Mahato, B., Shee, S. K., Sahu, T., Ghosh Chowdhury, S., Sahu, P., Porter, D. A. & Karjalainen, L. P. (2015) *Acta Mater*. **86**, 69-79.

Martin, S., Wolf, S., Martin, U., Krüger, L. & Rafaja, D. (2016) *Metal. Mater. Trans*. A. **47**, 49-58.

Mohammed, A. A. S., El-Danaf, E. A., Radwan, A-K. A. (2007) *Mater. Sci. Eng*. A. **457**, 373-379.

Park, K.-T. (2013) *Scr. Mater.* **68**, 375-379.

Phiu-on, K. & Bleck, W. (2008) Lehrstuhl und Institut für Eisenhüttenkünde, Aachen.

Pierce, D. T. & Jiménez, J. A, Bentley, J., Raabe, D., Oskay, C. & Wittig, J. E. (2014) *Acta Mater*. **68**, 238-253.

Pietrzyk, M., Madej, L., Rauch, L. & Szeliga, D. (2015) Computational Materials Engineering (Chapter Four), 153-208.

Ray, I. L. F. & Cockayne, D. J. H. (1973) *J. Microsc*. **98**, 170-173.

Rollett, A. D. & Kocks, U. F. (1993) *Solid State Phenomena*. **35-36**, 1-18.

Saeed–Akbari, A., Imlau, J., Prahl, U. & Bleck, W. (2009) *Metall. Mater. Trans*. A. **40**, 3076-3090.

Shi, X., Saada, G. & Veyssière, P. (1995) *Philos. Mag. Lett*. **71**, 1-9.

Shyamal, S., Ghiasabadi Farahani, M., Allam, T., Hamada, A.S., Haase, C., Kömi, J. I., Chakraborti, P. C., Sahu, P. (2021) *Scr. Mater*. **192**, 83-88.

Smallman, R. E. & Ngan, A. H. W. (2007) Physical Metallurgy and Advanced Materials, Seventh edition, Elsevier Ltd.

Steeds, J. W. (1966) *Proc. R. Soc*. A. 292, 343-373.

Steinmetz, D. R., Jäpel, T., Wietbrock, B., Eisenlohr, P., Gutierrez-Urrutia, I., Saeed-Akbari, A., Hickel, T., Roters, F. & Raabe, D (2013). *Acta Mater*. **61**, 494-510.

Suzuki, H. & Barrett, C. (1958) *Acta Metall*. **6**, 156-165.

Takaki, S., Nakatsu, H. & Tokunaga, Y. (1993) *Mater. Trans. JIM*. **34**, 489-495.

Ueji, R., Tsuchida, N., Terada, D., Tsuji, N., Tanaka, Y., Takemura, A. & Kunishige, K. (2008) *Scr. Mater*. **59**, 963-966.

Ungar, T. & Ribarik, G. (2017) *IOP Conf. Ser. Mater. Sci. Eng*. **194**, 1-8.

Veyssière, P. & Grégori, F. (2002a) *Philos. Mag*. A. **82**, 579-590.

Veyssière, P. & Grégori, F. (2002b) *Philos. Mag.* A. **82**, 567-577.

Volosevich, P., Gridnev, V. & Petrov, Y. (1976) *Phys. Met. Metallogr.* **42**, 126-130.

Yvell, K. (2018) *KTH Royal Institute of Technology*. pp 63.

Chapter 7

A quantitative assessment of dislocation substructures' contribution to flow-stress

*This chapter is published in Materials Letters, 300 (2021) 130216 (No. 3 in the list of publications).

7.1 The dislocation substructures and their contribution to flow-stress

In absence of dynamic strain ageing (DSA) and planar faults, the total flow stress of the studied steel can be approximated as: $\sigma_{total} = \sigma_{YS}^{0} + \sigma_{loop} + \sigma_{forest}$ where, σ_{YS}^{0}, σ_{loop} and σ_{forest} are the contributions to flow stress due to lattice friction, prismatic dislocation loop and forest dislocations, respectively. The contributions to σ_{YS}^{0} are from the lattice friction stress (σ_0), approximated for fine-grained steel from the flow curve in Fig. 3.1(a) as: 375 MPa. The contribution of σ_{loop} be calculated using the relation involving dislocation core radius (r) i.e. the region within which the linear elastic solution diverges, prismatic loop diameter (w) and the average prismatic loop density (ρ_{loop}) (Fourie & Murphy, 1962):

$$\sigma_{loop} = \frac{Gb\sqrt{\rho_{loop} w \sin 45°}}{2\pi(1-\nu)} log\left(\frac{w}{r}\right) \tag{7.1}$$

where, $G \approx 72$ GPa is the shear modulus, ν = 0.24 is Poisson’s ratio and b = 0.2554 nm is magnitude of the Burgers vector. A reasonable value for r lies in the range: $b \leq r \leq 4b$, and often approximated as ~ 1 nm (Hull & Bacon, 2011). From Fig. 6.3.(c) (Chapter 6.1.1), w is estimated as ~ 40 nm, also matching well with the literature (Fourie & Murphy, 1962).

Table7.1: Dislocation parameters and their contribution to flow stress.

Strain (%)	Dislocation density, ρ($\times10^{14}$ m^{-2})	Dislocation interaction parameter, α_i	Observed flow-stress (MPa	Forest dislocation Contribution (MPa)
2%	1.18	0.429	392	
5%	1.44	0.423	457	49
10%	1.78	0.416	570	162
50%	24.86	0.335	1338	930

The challenge lies in experimental determination of ρ_{loop}, while Fourie and Murphy in their original work (Fourie & Murphy, 1962) assumed ~ 10^{19} loops/m^3, it was later shown by Zhou *et al*. (2017), that a constant loop density $\sim 10^{21}$ loops/m^3 best reproduces the stress-strain behavior of Al during laser shock peening. Therefore, $\rho_{loop} \sim 10^{21}$ loops/m^3 was assumed for estimating σ_{loop}. With these considerations, σ_{loop} was estimated as ~ 33 MPa from Eq. (7.1), which is indeed consistent with the report of Kuhlmann–Wilsdorf (1989) that the contribution of loops to strain hardening is minimal. On the other hand, the contribution of forest dislocation could be estimated using Taylor's equation (Taylor, 1934): $\sigma_{forest} = T\alpha_i Gb\sqrt{\rho}$ where, T is the Taylor factor, ρ is dislocation density and α_i is dislocation interaction strength parameter. It was further suggested that for microstructures containing LEDS, the parameter α_i should not be assumed constant, and its variation with strain is calculated as (Kuhlmann–Wilsdorf, 1989):

$$\alpha_i = \frac{1-\frac{\nu}{2}}{6\pi(1-\nu)} ln\left(\frac{3}{b\sqrt{\rho}}\right) \tag{7.2}$$

Thus, the estimation of α_i for each terminal strain from Eq. (7.2) is based on the ρ values obtained from the X-ray line profile analysis for each strain, also presented in Table 7.1. The variation of α_i with strain is shown in Fig. 7.1(a), which clearly indicates that interactions among dislocations decreases at large strains, presumably through dynamic recovery (DRV). In agreement to this, the TEM BF microstructure presented in Fig. 7.1(b) contains areas of very low density of dislocations, which are surrounded by regions of high-density dislocation walls, characteristic of a high SFE microstructure. It also indicate towards some decrease in the correlation among dislocations indeed occurs through DRV occurring before fracture (~50% strain) (Mahato *et al.*, 2015). DRV in high-Mn steels is generally observed during hot deformation, while the present steel was deformed at RT with a quasi-static strain rate, thus

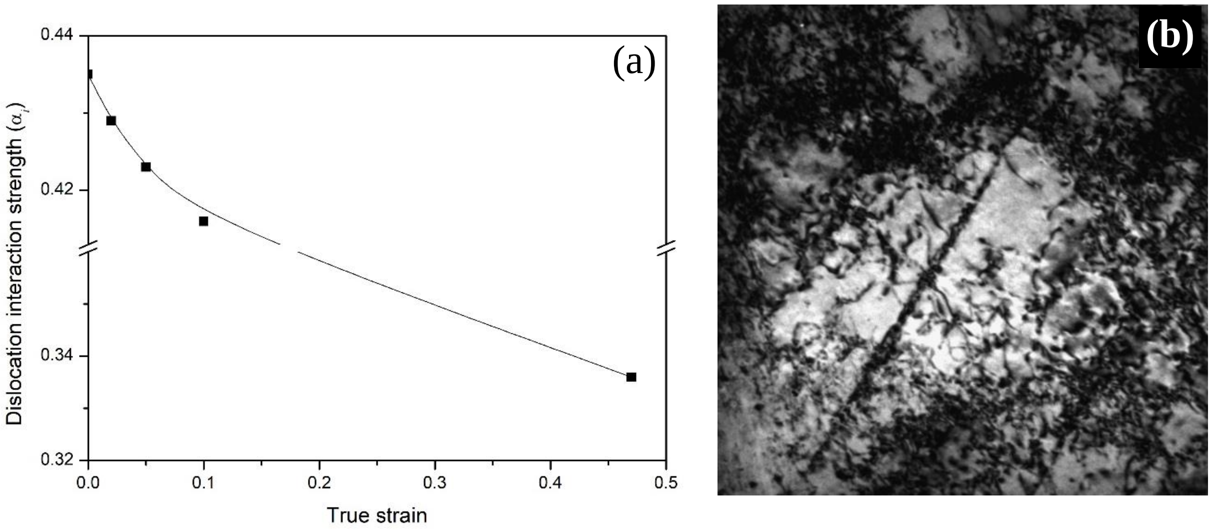

Fig. 7.1: (a) Variation of dislocation interaction strength parameter with strain. (b) Recovered region in austenite surrounded by forest dislocations in multi-beam condition at failure strain ~50%.

any adiabatic heating induced DRV is ruled out, but attributed to the presence of LEDS observed under TEM ((Fig. 6.2) (Chapter 6.1.1))((Kubin & Devincre, 1999).

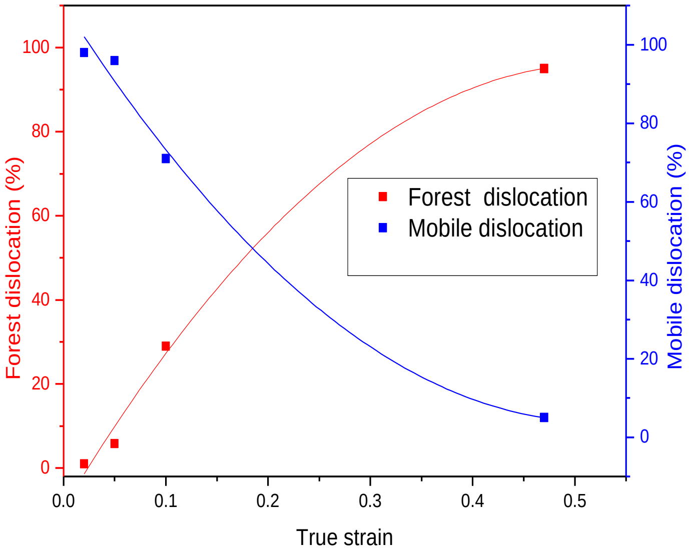

Fig. 7.2: Variation of mobile and forest dislocation fraction with strain.

Besides the contribution from σ_{YS}^{0}, the observed true flow stress includes contributions from primarily two types of dislocations, namely, the prismatic loops and the newly created forest dislocations. At 2% strain, by adding σ_{YS}^{0} ~ 375 MPa and σ_{loop}~ 33 MPa one obtains a flow stress of 408 MPa, which is comparable to the observed flow stress of 392 MPa in (Table 7.1), also indicating σ_{forest} is significant at 2% strain. In fact, no hardening was observed in the flow stress curve (Fig. 3.1(a) of Chapter 3.2) until this strain, while discontinuous yielding took place. Hardening in Fig. 3.1(a) of Chapter 3.2 indicates the predominance of σ_{forest} at higher strains. Using $\alpha_i$and ρ values from Table 7.1 for 5% strain and considering T =3.06, it is further obtained that σ_{forest} = 290 MPa. Therefore, adding up the previous contributions from σ_{YS}^{0} and σ_{loop} with σ_{forest}, the calculated flow stress is ~ 698 MPa, which is ~ 240 MPa higher than the observed flow stress value ~ 460 MPa at 5% strain (Table 7.1). This mismatch in the flow stress essentially arises due to the fact that entire dislocation density reported in Table 7.1 comprises of mobile and forest dislocations. Thus, only a fraction of this ρ value will contribute to the Taylor hardening. To our knowledge, no empirical equations or direct methods allow the estimation of such fraction of total dislocation densities, and therefore, an indirect and approximate approach is now presented below, based on the assumption that most of the loops are created at early strains (2%) and that their number remains nearly constant throughout the deformation range (Kubin & Devincre, 1999). It was further proposed that any stable work hardening at large strains is possible if the newly created mobile dislocations break away from the pre-existing configurations of forest dislocations.

A simple back-estimation in this study gives that the observed flow stress value at 5% will be matched only if 4% of the reported ρ value in Table 7.1 contribute through Taylor hardening, which in other words, is equivalent to presence of about only 4% forest dislocations at 5% strain contributing to ~49 MPa (Table 7.1) while the remaining 96% dislocations in the estimated density should come from mobile dislocations. In a similar fashion, the fraction of forest and mobile dislocation are obtained for the remaining terminal strain and plotted in Fig. 7.2 showing that the mobile dislocations' fraction decreasing to 70% and 10% for 10% and 50% strains, respectively. Expectedly, the forest dislocations at these strains increase to – 30% and 90%, which respectively contribute ~ 162 MPa and ~ 930 MPa to flow stress values (Table 7.1). This has an additional implication that newly created forest dislocations gradually outnumber the loops and the mobile dislocations at higher strains, resulting in gradual decrease in latter fractions in the dislocation population.

References

Fourie, J. T. & Murphy, R. (1962) *J. Philos. Mag.* **7** (82) 1617-1631.

Kubin, L.P. & Devincre, B. (1999) in: Bilde-Sørensen, et al. (Eds.), Deformation Induced Microstructures: Analysis and Relation to Properties. Risø National Laboratory, Roskilde, Denmark. 61-83.

Kuhlmann-Wilsdorf, D. (1989) *Mater. Sci. Eng.* A. **113**, 1-41.

Mahato, B., Shee, S. K., Sahu, T., Ghosh Chowdhury, S., Sahu, P., Porter, D. A. & Karjalainen, L. P. (2015) *Acta Mater.* **86**, 69-79.

Pierce, D. T. & Jiménez, J. A, Bentley, J., Raabe, D. & Wittig, J. E. (2015) *Acta Mater.* **100**, 178-190.

Taylor, G.I. (1934) *Proc. R. Soc.* **145**, 362-387.

Zhou, W., Ren, X., Ren, Y., Yuan, S., Ren, N., Yang, X., Adu-Gyamfi, S., Philos. Mag. (2017) **97,** 917-929.

Chapter 8

Summary and conclusions

8.1 General conclusion

In this thesis the deformation microstructure and plasticity mechanism of a high-Mn Fe 26Mn-1Al-0.14C steel was studied. The Fe-26Mn-1Al-0.14C steel was tensile tested at RT using quasi static strain rate of $10^{-4\ \mathrm{s}-1}$. XRD data acquisition of the differently strained specimens is carried out to know the structural and microstructural information. The EBSD and ECCI measurements were performed using a high-resolution field emission scanning electron microscope. TEM investigations were carried out to observe the deformation microstructure and deformation mechanism. Based on the results the following conclusions can be drawn:

1. A distinct four-stage strain hardening with a nearly constant strain hardening rate as high as 2 GPa (~ $\frac{G}{35}$) was observed until ~30% true strain, which at higher strains decreases slightly up to the fracture strain of ~50%. The deformation was dominated by various dislocation activity and delayed dynamic recovery, only causing a marginal drop in strain hardening rate at high strains.
2. High incidence of screw type dislocations' proliferation was revealed at the onset of deformation (2% strain) that gradually decreased with increasing imposed strain, while the densities of planar (stacking and twin) faults remained uncharacteristically small (~10^{-4}) until fracture occurring at ~50% strain.
3. Strong dipole character of dislocations was observed at the beginning of deformation, which facilitated cross-slip at early strain.
4. The early-stage deformation microstructure comprised of Taylor lattice and dislocation substructures, such as dislocation dipoles and multipoles, created by cross-slip. Wavy glide became even more pronounced at a higher strain of 10%, wherein the earlier dislocation structures transformed to weak tangles and cells.
5. Despite the dislocation densities increasing monotonously with increasing strain, and the highest value (~10^{15} m^{-2}) being observed at fracture strain (~50%), dynamic recovery was very significant at this strain (~50%), resulting in decreasing correlation among the dislocations, correlated through the gradually increasing $R_e$values from 34 nm at 2% strain to 43 nm at failure.
6. The microstructural aspects of the steel could be reasonably correlated with the relatively high SFE of the steel ~60 mJ/m^2, which was estimated according to the *modified* Schramm and Reed method based on the dislocation induced anisotropic strain broadening. The high SFE value was not favorable for any planar slip and consequent deformation twinning but

it promotes a wavy slip and cross-slip at the onset of deformation, while complex dislocation substructures, like tangles and cells were observed at large strains.

7. Wide SFs, as obstacles to dislocation glide, were rare in the microstructure due to the high SFE of the fine-grained steel, ~ 60 mJ/m^2, because of a very high critical stress value required to form. In this situation, dislocation glide dominated and deformation twinning was largely suppressed throughout the straining range.
8. The twin deficiency could not be explained on the basis of critical twinning stress. Rather, the deficiency of twinning is collectively attributed to absences of extended SFs and suitable dislocation pile-ups as well the presence of dislocation substructure.
9. Plasticity was governed by a cross-slip assisted dislocation truncation mechanism producing dislocation loop strings and Taylor lattices at early strain. Such a cross-slip based mechanism is expected to delay dynamic recovery in stage C to produce a good combination of high strength and ductility.
10. The dislocation substructure at 2% strain comprises of prismatic loops and mobile dislocations, wherein the contribution of loops to flow stress is minimal: 33 MPa and no hardening was observed until this strain. At 5% strain, the role of forest dislocations is activated and 4% of such dislocations were found contributing ~ 49 MPa, whose propensity increases rapidly with further increasing strain whose corresponding contribution was ~ 162 MPa and ~ 930 MPa, accompanied with a concomitant decrease in the population of mobile dislocations.

8.2 Scope for future work

In continuation of the studies on the Fe-26Mn-1Al-0.14C steel, it is imperative that the following aspects should be planned as future activity.

1 To investigate the role of short-range ordering on the flow stress behavior of Fe-Mn-Al-C steels from high resolution TEM investigation.

2 Unravel the role of Grain boundary dislocation interaction that lead to formation of dislocation substructures in Fe-Mn-Al-C steels.

Publications

Journal Publications

Materials Characterization 172 (2021) 110833

Contents lists available at ScienceDirect

Materials Characterization

journal homepage: www.elsevier.com/locate/matchar

X-ray line profile analysis of the deformation microstructure in a medium-grained Fe-Mn-Al-C austenitic steel

S.R. Das[a], S. Shyamal[a], S.K. Shee[b], J.I. Kömi[c], P. Sahu[a,*]

[a] *Department of Physics, Jadavpur University, Kolkata 700 032, India*
[b] *Department of Physics, Midnapore College, Midnapore 721 101, West Bengal, India*
[c] *Centre for Advanced Steels Research, University of Oulu, Box 4200, FIN 90014, Finland*

Materialia 15 (2021) 101042

Contents lists available at ScienceDirect

Materialia

journal homepage: www.elsevier.com/locate/mtla

Full Length Article

On the mechanism of cross-slip induced dislocation substructure formation in an high-Mn steel

S.R. Das[a], S. Shyamal[a], T. Sahu[b], J.I. Kömi[c], P.C. Chakraborti[d], D.A. Porter[c], L.P. Karjalainen[c], P. Sahu[a,*]

[a] *Department of Physics, Jadavpur University, Kolkata 700 032, India*
[b] *Department of Physics, S.A. Jaipuria College, Kolkata 700 005, India*
[c] *Centre for Advanced Steels Research, University of Oulu, Box 4200, FIN–90014, Finland*
[d] *Department of Metallurgical and Material Engineering, Jadavpur University, Kolkata 700 032, India*

Materials Letters 300 (2021) 130216

Contents lists available at ScienceDirect

Materials Letters

journal homepage: www.elsevier.com/locate/matlet

A quantitative assessment on the contribution of various dislocation substructures to flow stress in a fine-grain high-Mn steel

S.R. Das [a], T. Riaz [a], S. Shyamal [a], P.C. Chakraborti [b], P. Sahu [a,*]

[a] Department of Physics, Jadavpur University, Kolkata 700 032, India
[b] Department of Metallurgical and Material Engineering, Jadavpur University, Kolkata 700 032, India

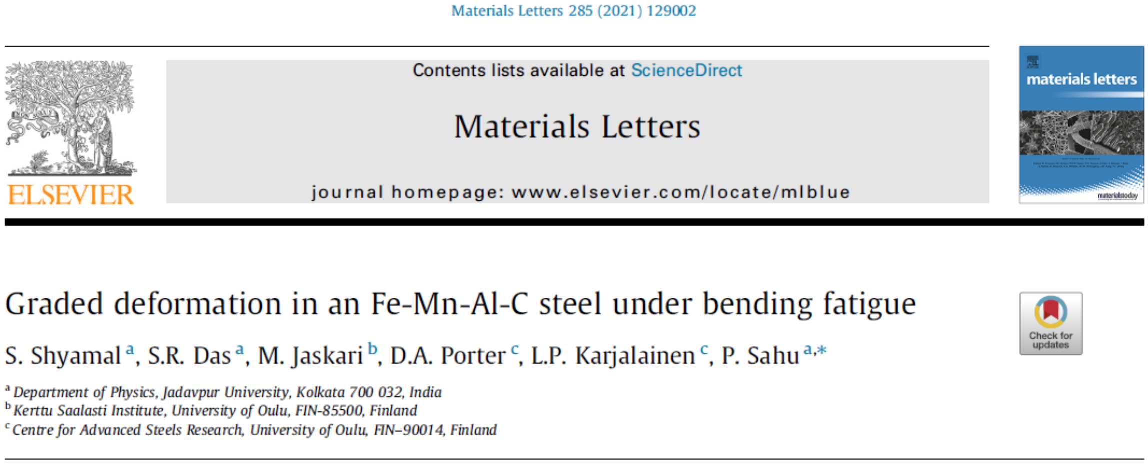

Materials Letters 285 (2021) 129002

Contents lists available at ScienceDirect

Materials Letters

journal homepage: www.elsevier.com/locate/mlblue

Graded deformation in an Fe-Mn-Al-C steel under bending fatigue

S. Shyamal [a], S.R. Das [a], M. Jaskari [b], D.A. Porter [c], L.P. Karjalainen [c], P. Sahu [a,*]

[a] Department of Physics, Jadavpur University, Kolkata 700 032, India
[b] Kerttu Saalasti Institute, University of Oulu, FIN-85500, Finland
[c] Centre for Advanced Steels Research, University of Oulu, FIN–90014, Finland

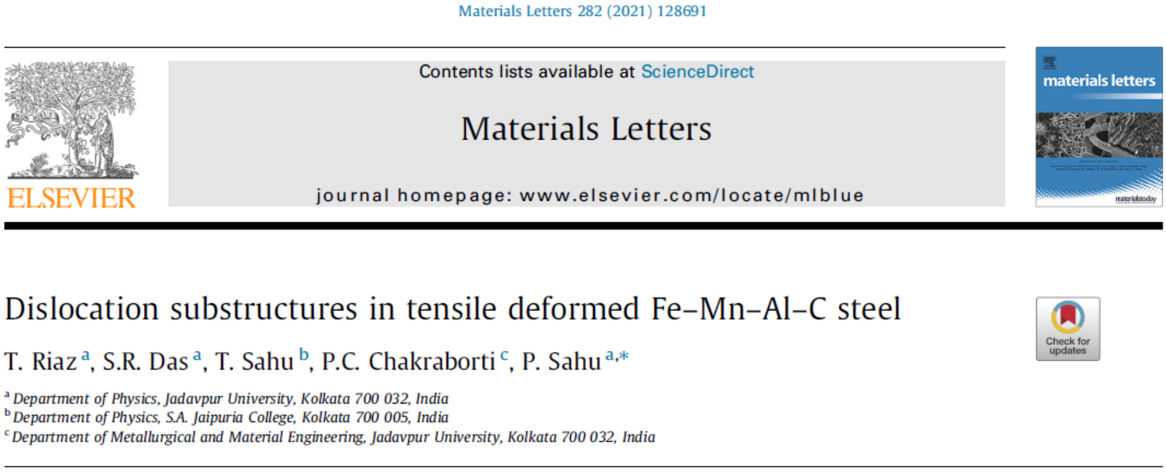

Materials Letters 282 (2021) 128691

Contents lists available at ScienceDirect

Materials Letters

journal homepage: www.elsevier.com/locate/mlblue

Dislocation substructures in tensile deformed Fe–Mn–Al–C steel

T. Riaz [a], S.R. Das [a], T. Sahu [b], P.C. Chakraborti [c], P. Sahu [a,*]

[a] Department of Physics, Jadavpur University, Kolkata 700 032, India
[b] Department of Physics, S.A. Jaipuria College, Kolkata 700 005, India
[c] Department of Metallurgical and Material Engineering, Jadavpur University, Kolkata 700 032, India